Title
High Resolution Numerical Studies of the Milky Way Halo

Author
Rashkov, Valery

Publication Date
2013

Peer reviewed|Thesis/dissertation

UNIVERSITY OF CALIFORNIA
SANTA CRUZ

HIGH RESOLUTION NUMERICAL STUDIES OF THE MILKY WAY HALO

A dissertation submitted in partial satisfaction of the
requirements for the degree of

DOCTOR OF PHILOSOPHY

in

ASTRONOMY AND ASTROPHYSICS
with an emphasis in STATISTICS

by

Valery Rashkov

June 2013

The Dissertation of Valery Rashkov
is approved:

Professor Piero Madau, Chair

Professor Constance Rockosi

Professor Puragra GuhaThakurta

Tyrus Miller
Vice Provost and Dean of Graduate Studies

Table of Contents

List of Figures **v**

List of Tables **vi**

Abstract **vii**

Dedication **ix**

Acknowledgments **x**

1 Introduction **1**
- 1.1 Some observations from the last decade . . . 1
- 1.2 Computer models and the problems they created . . . 2
- 1.3 Black holes in the MW halo - an exciting possibility . . . 5
- 1.4 The mass of the MW galaxy – a fundamental, yet elusive measure . . . 6
- 1.5 What next for the MW halo? . . . 7

2 On the Assembly of the Milky Way Dwarf Satellites and Their Common Mass Scale **8**
- 2.1 Introduction . . . 8
- 2.2 Simulation and particle tagging technique . . . 11
  - 2.2.1 Assembly history . . . 16
  - 2.2.2 Surviving satellites . . . 17
- 2.3 Kinematics of dwarf spheroidal satellites . . . 26
  - 2.3.1 The spherical Jeans equation . . . 26
  - 2.3.2 Applications to VLII dwarf satellites . . . 30
- 2.4 Summary . . . 37

3 A Population of Relic Intermediate-Mass Black Holes in the Halo of the Milky Way **40**
- 3.1 Introduction . . . 40
- 3.2 Black Hole Tagging Technique . . . 43
- 3.3 Demography of IMBHs . . . 45
  - 3.3.1 Population III Remnants . . . 45
  - 3.3.2 Direct Collapse Precursors . . . 46
- 3.4 Black Hole Recoils . . . 48

3.5 Spatial Distribution of IMBHs 50
3.6 Discussion 52

4 What is the mass of the Milky Way? 57
4.1 Introduction 57
4.2 Halo Tracer Population 59
4.3 The Eris Simulation 60
4.4 Tracer Mass Estimator 63
4.4.1 The Jeans equation - interface between kinematic tracers and galactic potentials 63
4.4.2 Applications of the Jeans equation to simulated galaxies 65
4.4.3 Parameter uncertainties - the velocity anisotropy 66
4.4.4 Parameter uncertainties - the stellar density profile 68
4.5 The Mass of the Milky Way's Halo 70
4.5.1 Direct comparison with observable data 70
4.5.2 Understanding the line-of-sight velocity dispersion profile 72
4.6 Summary 74

Bibliography 77

List of Figures

1.1 The Belokurov et al. (2006) Field of Streams 3

2.1 Distribution of the peak mass M_{h} at infall for VLII subhalos 12
2.2 Projected mass surface density of the VLII dark matter halo and its stellar halo . 18
2.3 Luminosity function and metallicity evolution of VLII dSph satellites 22
2.4 Positions, star formation efficiency evolution, and velocity structure evolution of VLII dSph satellites 23
2.5 Evolution of satellite V_{max} from infall to today 24
2.6 Luminosity and kinematics of the Carina and Sculptor simulated equivalents . . 27
2.7 Structural properties of the surviving VLII satellites 28
2.8 Kinematic analysis of VLII satellites with the Jeans equation 32
2.9 The VLII "common mass scale" and undetectable dSph satellites 35

3.1 Distributions of the stellar velocity dispersion and infall epochs of IMBH-hosting subhalos in VLII 44
3.2 Distribution of IMBHs in the VLII galactic halo today 47
3.3 Mass functions and location of IMBHs in the galactic halo 49
3.4 Number of subhalo mergers producing a recoiling IMBH, as a function of redshift 50
3.5 Spatial distribution of Galactic IMBHs vs Dark Matter 51
3.6 Distribution of V-band peak surface brightness of stellar cusps surrounding Galactic IMBHs 53
3.7 Angular size of stellar clusters around Galactic IMBHs 55

4.1 Density maps of the Eris and VLII stellar halos 62
4.2 Performance of a simple mass estimator when applied to Eris and VLII 66
4.3 Velocity anisotropy in Eris and VLII as a function of radius 67
4.4 Stellar density profiles in Eris and VLII 68
4.5 Eris and VLII stellar halo $v_r - R$ phase space density 69
4.6 Eris and VLII radial velocity dispersion profiles compared to observational data . 71
4.7 Radial velocity dispersion profiles from integration of the Jeans equation 72
4.8 Effect of the inner halo contraction due to stellar disk in the radial velocity dispersion profile 74

List of Tables

2.1 Build-up of the VLII stellar halo 12

3.1 Demography of Galactic IMBHs 49

4.1 Recent mass estimates of the Milky Way 58

Abstract

High Resolution Numerical Studies of the Milky Way Halo

by

Valery Rashkov

The halo of the Milky Way (MW) contains residual evidence of its hierarchical accretion history, such as stellar streams, dwarf satellite galaxies and possibly even intermediate-mass black holes the latter carried as they fell into the larger Galaxy. The discovery and study of these objects have the potential to answer elusive questions about our Galaxy, such as the accurate determination of its total mass, a fundamental quantity that determines the properties and fate of galaxies in the Universe.

I use a particle tagging technique to dynamically populate the N-body *Via Lactea II* high-resolution simulation with stars. The method is calibrated using the observed luminosity function of Milky Way satellites and the concentration of their stellar populations, and self-consistently follows the accretion and disruption of progenitor dwarfs and the build-up of the stellar halo in a cosmological "live host". Simple prescriptions for assigning stellar populations to collisionless particles are able to reproduce many properties of the observed Milky Way halo and its surviving dwarf satellites, like velocity dispersions, sizes, brightness profiles, metallicities, and spatial distribution. I apply a standard mass estimation algorithm based on Jeans modelling of the line-of-sight velocity dispersion profiles to the simulated dwarf spheroidals, and test the accuracy of this technique. The inner mass-luminosity relation for currently detectable satellites is nearly flat in this model, in qualitative agreement with the "common mass scale" found in Milky Way dwarfs.

I extend the tagging approach to the study of intermediate-mass black holes (IMBHs),

and assess the size, properties, and detectability of the leftover accreted halo population. The method assigns a black hole to the most tightly bound central particle of each subhalo at infall according to an extrapolation of the $M_{\rm BH}-\sigma_*$ relation, and self-consistently follows the accretion and disruption of Milky Way progenitor dwarfs and their holes in a cosmological "live" host from high redshift to today. I show that, depending on the minimum stellar velocity dispersion, below which central black holes are assumed to be increasingly rare, as many as two thousand or as few as seventy IMBHs may be left wandering in the halo of the Milky Way today. I identify two main Galactic subpopulations, "naked" IMBHs, whose host subhalos were totally destroyed after infall, and "clothed" IMBHs residing in dark matter satellites that survived tidal stripping. Naked IMBHs typically constitute about half of the total and are more centrally concentrated. Their detection may provide an observational tool to constrain the formation history of massive black holes in the early Universe.

I use the results from the stellar halo tagging in combination with the state-of-the-art hydrodynamical cosmological simulation *Eris* to address the question of the poorly known Milky Way halo mass. Taking advantage of the two simulated galaxies' very different masses, I explore the full range of estimates for the Galaxy from observational data. I establish that the simulated halos reproduce many of the properties of the MW stellar halo, including its density profile slope, velocity anisotropy and, in the case of the lighter galaxy, its radial velocity dispersion profile. There is a striking link between discontinuities in these quantities where significant pileup of stars in the orbital apocenters of their progenitors exists in phase space. I carry out controlled experiments using numerical integration of the Jeans equation to conclude that the lighter halo, *Eris*, indeed provides a much better fit to the data than the more massive halo of *Via Lactea II*.

To our ailing global ecosystem

Acknowledgments

This work would not have been possible without the incredible help and support of many individuals, some of who I would like to thank here:

Piero Madau, for being my scientific adviser, for supporting me for five years, and for enabling me to work with the finest galaxy simulations at the time of my graduate studies; Connie Rockosi and Raja Guha Thakurta, for the many fruitful discussions about the Milky Way and Andromeda galaxies, and for taking me out of the simulation box and into the observational world; Nathan Goldbaum, for teaching me about Romberg integration and thus enabling me to integrate the Jeans equation; Mike Kuhlen and Juerg Diemand, for teaching me how to work with dark matter simulations and overseeing my first project at UCSC; Kevin Schlaufman, for showing me the importance of proper statistics in data analysis, for inspiring me to think outside the academic box, and for the many hours we spent together in sailing class; Michele Fumagalli, for being a great friend, for showing me that things aren't usually as hard as they seem to be at first, and for the affogato with Jack; Robert da Silva and Jacob Arnold, for being there and not allowing "my face to explode" when I was looking for a job, and for introducing me to the finest of American humor; Fernanda Duran, for her seemingly endless energy and optimism; Hannah Marcus and Morgan MacLeod, for all the fun times at 1120 Bay; Annalisa Pillepich, for her cheer, excitement and selflessness in our discussions about galaxy formation and life in general; my dear friends Zoë Buck and Chris Bracey, for the love, support and all the wonderful times together. Special thanks also go to Javiera Guedes, Anne Medling, Neil Miller, James Guillochon, Alis Deason, Tomer Tal, Adriane Steinacker, Greg Laughlin, Maria Sliwinski, the city of San Francisco and all my friends there, the teams behind Google Maps and Wikipedia, as well as the National Park Service.

Above all, I thank my parents and my brother for all the support and love they have given me not just during these five years, but throughout. I would have never completed a PhD without you.

The text of this dissertation includes reprints of the following previously published material: “On the Assembly of the Milky Way Dwarf Satellites and Their Common Mass Scale”, (2012, ApJ, 745, 142) and “A Population of Relic Intermediate-Mass Black Holes in the Halo of the Milky Way” (2013, submitted to ApJ, arXiv: 1303.3929R). The co-author listed in this publication directed and supervised the research which forms the basis for the dissertation.

Chapter 1

Introduction

1.1 Some observations from the last decade

It has been an exciting decade to study the Galactic halo. With the dawn of deep, wide, multi-color photometric and spectroscopic surveys like the Sloan Digital Sky Survey (SDSS; Gunn et al. 1998, York et al. 2000), our knowledge of the outskirts of our Galaxy has dramatically increased.

Among the first hints that the MW's halo was not smooth and originated in a hierarchical accretion fashion was the discovery of the heavily perturbed Sagittarius dwarf galaxy Ibata et al. (1994). Rich substructure, including ultra-faint dwarf spheroidal galaxies (Willman et al. 2005, Belokurov et al. 2007; 2010), stellar streams (Belokurov et al. 2006) and other overdensities, arguably shells (Jurić et al. 2008), have been identified in star count maps since then. Recently, Bell et al. (2008) quantified the amount of substructure as a function of radius, confirming expectations that the stellar halo gets more "lumpy" with distance, consistent with it having an accreted origin, as the much longer mixing timescale in its lower-density outskirts ensures the survival of these substructures.

Beyond the spatial domain, substructure in the MW halo has been identified in the velocity and metallicity spaces as well. Using data from the Sloan Extension for Galactic Understanding and Exploration (SEGUE; Yanny et al. 2009), Schlaufman et al. (2009) identified numerous elements of cold halo substructure within 20kpc of the MW center with statistically distinct radial velocity structure relative to a smooth underlying halo. Additionally, the same authors observed significant angular autocorrelation in the positions of stars with similar metallicity even in regions with no significant overdensity in position or velocity space (Schlaufman et al. 2012).

Further from home, similar studies are starting to uncover the wealth of structure in the halos of external galaxies. Ibata et al. (2001a) discovered a "Giant Stream" around the Andromeda galaxy, and McConnachie et al. (2009) later reported significant debris consistent with leftovers of disrupted dwarf galaxies in its halo. Since then, the Spectroscopic Portrait of Andromeda's Stellar Halo (SPLASH; Kalirai et al. 2006, Gilbert et al. 2006) has provided a wealth of information on the chemistry and kinematics of the building blocks of Andromeda's halo. Beyond the Local Group, Martínez-Delgado et al. (2010) have presented the first halo substructures in nearby spiral galaxies. While intrinsically harder due to the larger distances, these studies complement the study of the MW halo by giving us an external view of halo substructure that is easier to interpret.

In Figure 1.1, we show one of the most iconic images of recent MW stellar halo studies - the "Field of Streams" of Belokurov et al. (2006).

1.2 Computer models and the problems they created

At the same time as these observational advances, computer models have become powerful enough to provide a point of comparison with observations. Following predictions

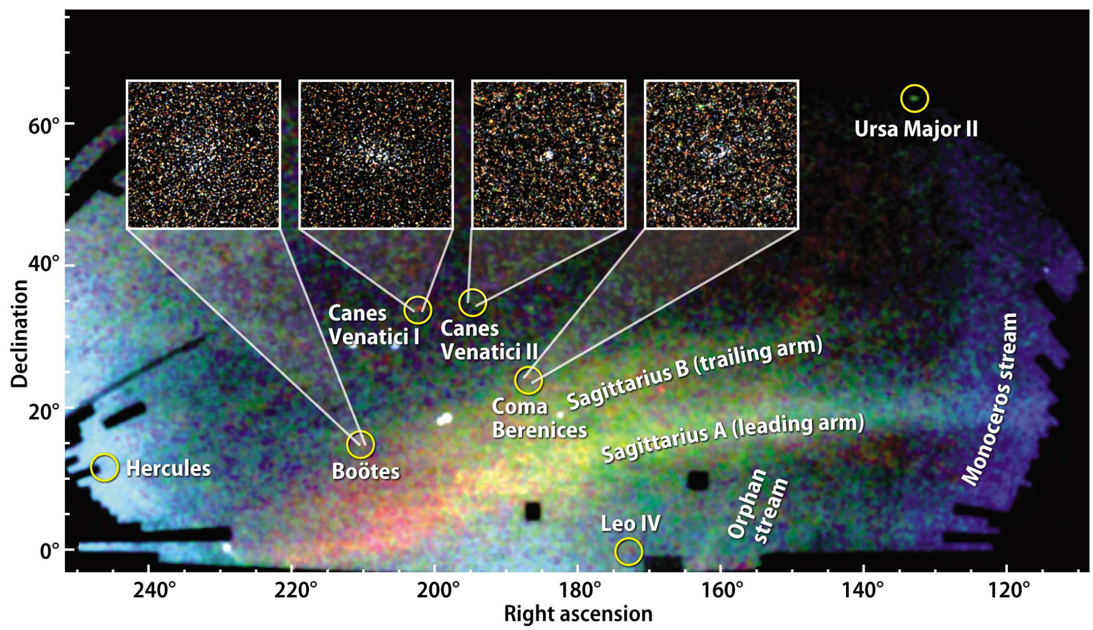

Figure 1.1: One of the most iconic images from the past decade of MW stellar halo studies – the Belokurov et al. (2006) "Field of Streams". This structure becomes apparent in the density distribution of SDSS stellar data after the application of a simple color cut that roughly selects upper main sequence and turnoff stars. Stars are color coded by distance, with blue for the nearest and red for the furthest stars. Shown are the location of various known MW substructures, including ultra-faint dwarf galaxies. Stellar overdensity maps, in which the latter were first spotted, are shown as a tribute to the difficulty involved in their discovery.

from the hierarchical ΛCDM galaxy formation scenario (White & Rees 1978, Blumenthal et al. 1984), high-resollution zoom-in fully cosmological simulations that produce galactic halos from the continuous accretion of smaller building blocks (subhalos populated with dwarf galaxies) have been successfully completed recently (Bullock & Johnston 2005, Diemand et al. 2005, Springel et al. 2008, Cooper et al. 2010). Existing in the full cosmological context, yet with full resolution capabilities to resolve the scales of ultra-faint dSph galaxies, simulations have opened as many questions as they have answered.

The first significant discrepancy between the data and models became known as the "missing satellites problem" (Klypin et al. 1999, Moore et al. 1999) and refers to the fact that numerical simulations based on the CDM paradigm overpredict the number of surviving bound satellites by a large factor. While SDSS doubled the number of known MW satellites and suffers from the drawbacks of incomplete sky coverage and a distance-dependent magnitude limit (Tollerud et al. 2008), correcting the expected number of currently unobserved satellites for these limitations of the survey does not provide a satisfactory solution to the problem. Recently, the problem has been revisited in the context of baryonic physics and star formation within small substructures, which, owing to their extremely shallow potential wells, are unable to cool gas and form stars efficiently (Kuhlen et al. 2012).

A related, but distinct problem was pointed out by Strigari et al. (2008), who suggested that the inner regions of the dSph galaxies inhabiting the MW halo have a similar mass of $10^7 M_\odot$ within an aperture radius of 300pc, despite spanning four orders of magnitude in luminosity. This "common mass scale" of the MW dwarf satellites sparked another flurry of research activity, pointing to observational biases (Bullock et al. 2010), a fundamental scale in galaxy formation (Muñoz et al. 2009) or just a natural manifestation of the central density of subhalos in ΛCDM (Macciò et al. 2009). Cooper et al. (2010) approach the problem in a semi-analytical way, painting the properties of stellar populations onto the gravitational carriers - DM particles of the Aquarius simulations (Springel et al. 2008) according to the GALFORM model of galaxy formation (Bower et al. 2006). They demonstrate that simply applying a standard galaxy formation model on the scales of accreted by the MW subhalos can reproduce the large scale properties of the stellar halo and its dSph population.

In recent years, the “common mass scale” has been recast under a different name, the “too big to fail” problem (Boylan-Kolchin et al. 2011), referring to very centrally concentrated, massive subhalos within the MW halo that remain dark, failing to form stars. Predicted in high-resolution cosmological simulations, like VLII (Diemand et al. 2005) and the Aquarius suite (Springel et al. 2008), these subhalos’ rotation curves are too steep to accommodate the observed velocities measured at the MW dSph half-light radii. Further studies of this problem point to a baryonic solution. Pontzen & Governato (2012) suggest that repeated supernova explosions modify the central density cusp, leaving subhalos less resilient to accretion into the main galactic host halo.

1.3 Black holes in the MW halo - an exciting possibility

Getting a hold of the physics behind galaxy formation on the smallest known scales opened up the possibility to investigate a related and equally elusive question - the formation of galactic black holes in a hierarchical Universe. As most massive galaxies have locally been observed to host black holes in their centers, with the black hole mass correlating with the galaxy velocity dispersion (Häring & Rix 2004), one might ask about the implications of smaller black holes forming in dwarf galaxies for the MW halo. Recent observations have suggested that the $m-\sigma$ relation consistently extrapolates to the upper end of the dwarf galaxy velocity distribution - 30km/s (Barth et al. 2005, Xiao et al. 2011). Extrapolating a little further would reach the regime of intermediate-mass black holes, candidates for which have finally been identified in the cores of globular clusters (Gebhardt et al. 2005, Noyola et al. 2010, Lützgendorf et al. 2012).

The physics that could form IMBH in dwarf galaxies points to two different formation channels, implying different threshold halo masses necessary and hence different demographics of the accreted Galactic halo IMBH population. IMBHs could have formed early from the seed Population III stellar remnants (Madau & Rees 2001, Volonteri et al. 2003), forming in more ubiquitous, less massive building blocks of the MW halo, or later from the direct collapse of low-angular momentum gas in more massive, rarer hosts (Loeb & Rasio 1994, Koushiappas et al. 2004). Previous calculations of the number of black holes present in the Galactic bulge and halo today rely on techniques as diverse as analytical integration of the Press & Schechter (1974) formalism (Madau & Rees 2001), Monte Carlo realizations of a hypothetical MW accretion history (O'Leary & Loeb 2009, van Wassenhove et al. 2010), and collisionless simulations of galaxy formation (Micic et al. 2006; 2011).

1.4 The mass of the MW galaxy – a fundamental, yet elusive measure

Apart from the leftovers from its past accretion events, the overall structure of the MW halo itself is of great interest, especially its mass. A galaxy's mass determines its fate, from the environment it lives in to the size and morphology of its baryonic component. Knowing the MW mass accurately would give us a much better understanding of the amount of substructure we should expect to see in its halo. Wang & White (2012) used SDSS data to study the distribution of satellite galaxies around isolated bright hosts and concluded that their number increases strongly with the stellar mass of the primary, in proportion with the expected halo mass. This result suggests that a "lighter" MW might not have as big of a problem with its "missing satellites", however, it would exacerbate the odds of having two Magellanic clouds.

Galaxies the mass of the MW already have very small odds of having two satellites the mass of the Magellanic clouds, about 10% (Busha et al. 2011). Reducing the mass of the Galaxy beyond current estimates would then imply that the MW is somehow special.

Despite recent efforts to measure it, the MW mass remains largely uncertain, with estimates varying between $2 \times 10^{12} M_{\odot}$ (Wilkinson & Evans 1999) and $7 \times 10^{11} M_{\odot}$ (Deason et al. 2012b). Once again, these different measurements originate from the use of different relevant data sets - the rotation curve halo gas (Rohlfs & Kreitschmann 1988), the orbits of the Magellanic clouds (Besla et al. 2007), the dynamics of halo stars (Xue et al. 2008, Deason et al. 2012b). One of the biggest sources of uncertainty in the MW mass measurements is the fact that in all but a few cases, only the line-of-sight component of the velocity is available. Only recently has the well-known density-anisotropy degeneracy resulting from this limitation of our data been broken for the first time - Deason et al. (2012a) report an anisotropy parameter in the MW of 0.5, corresponding to a radial velocity dispersion twice that in the tangential direction.

1.5 What next for the MW halo?

Looking into the future, computer simulations run with full treatment of the relevant hydrodynamic physics, of which *Eris* (Guedes et al. 2011) was a pioneer will be more and more ubiquitous. They will provide an invaluable opportunity to study the diversity of cosmological galactic halos beyond the boundaries of a single galaxy with a single, unique accretion history. At the same time, the European Space Agency mission *Gaia* (Perryman et al. 2001) will observe one billion stars in the MW Galaxy, providing not only extremely precise astrometric positions, but also their transverse velocities, which will open new frontiers in research of the build-up and structure of the MW halo. With this wealth of data dawning upon us, high resolution studies of the MW halo are only about to begin.

Chapter 2

On the Assembly of the Milky Way Dwarf Satellites and Their Common Mass Scale

2.1 Introduction

Galaxy halos are one of the crucial testing grounds for ΛCDM structure formation scenarios, as they contain the imprints of their assembly via the hierarchical merging and accretion of many smaller progenitors (White & Rees 1978, Blumenthal et al. 1984). Subunits are predicted to collapse at high redshift and have high density concentrations, and when they merge into more massive hosts they are able to resist tidal disruptions and survive in large numbers as bound substructures (e.g. Diemand et al. 2008). The dwarf spheroidal (dSph) satellites present today in the halos of massive galaxies like our own Milky Way (MW) are thought to represent a fossil record of such early merging activity. The old tally of MW "classical" dwarfs with $M_V \lesssim -10$ (e.g. Mateo 1998) has been recently revised by the discovery of a new, large population of ultra-faint dwarfs in the *Sloan Digital Sky Survey* (SDSS) (Willman et al. 2005, Belokurov et al. 2007). Follow-up spectroscopic observations have shown that these extreme objects are the most dark matter-dominated galaxies as well as some of the most metal-poor stellar systems known in the universe (Simon & Geha 2007, Kirby et al. 2008, Geha et al. 2009). While most of the observed dSphs seem to be in pressure-supported equilibrium, others (like the Sagittarius dwarf, see Ibata et al. 2001b, Majewski et al. 2003) are being ripped by tidal forces into long streams of stars that will eventually dissolve into the Galactic stellar halo. Large coherent stellar streams have been observed in Andromeda's halo (McConnachie et al. 2009) and in the outskirts of other nearby galaxies (Martínez-Delgado et al. 2010, Mouhcine et al. 2010).

The predicted counts of bound substructures vastly exceed the number of known satellites of the MW, a "missing satellite problem" that has been the subject of many numerical studies over the last decade (e.g. Klypin et al. 1999, Moore et al. 1999, Madau et al. 2008a). While this discrepancy is partially alleviated by correcting the data to account for the incomplete sky coverage and distance-magnitude or surface brightness limits of current surveys (Koposov et al. 2008, Tollerud et al. 2008, Bullock et al. 2010), it is generally agreed that a complete solution to the apparent conflict between the Galaxy's relatively few observed stellar clumps and the abundance of halo substructure in cold dark matter simulations requires either a modification of the nature of the dark matter particle that would act to suppress small-scale power (e.g. Colín et al. 2000) or an extremely low star formation efficiency in small dark matter subunits (e.g. Kauffmann et al. 1993, Benson et al. 2002, Bullock et al. 2000, Somerville 2002, Kravtsov et al. 2004, Madau et al. 2008b, Kuhlen et al. 2012).

Measurements of the line-of-sight velocity dispersion as a function of radius in dwarf satellites, combined with a spherical Jeans analysis, may have provided another "small-scale puzzle". Despite spanning about 5 decades in luminosity, MW dSphs appear to contain a similar amount of dark mass, $M_{300} \sim 10^7$ $M_\odot$, within a fixed aperture radius of 300 pc from their centers (Strigari et al. 2008, Walker et al. 2009). It is unclear at this stage whether the flat inner mass-luminosity relation inferred, $M_{300} \propto L^{0.03\pm0.03}$, is an accident of small number statistics, an artifact of the spherical Jeans analysis technique, arises from an observational selection bias (Bullock et al. 2010), is evidence for a new fundamental scale in galaxy formation (Muñoz et al. 2009), or arises naturally in the ΛCDM paradigm (e.g. Macciò et al. 2009, Stringer et al. 2010).

Numerical simulations of the assembly of the halo of Milky Way-sized galaxies have the potential to shed light on the nature of dSph galaxies and test the ΛCDM hierarchical clustering paradigm. Owing to their computational expense, state-of-the-art cosmological hydrodynamic simulations that include gas cooling, star formation, and supernova feedback, and can self-consistently follow the formation and evolution of MW substructure down to the present epoch, are limited to dark particle masses $m_p \gtrsim 10^5$ $M_\odot$ (Guedes et al. 2011), and can well resolve only the most massive subhalos. To be able to reach the necessary resolution, we use in this chapter a particle tagging technique to dynamically populate the N-body *Via Lactea II* (hereafter VLII) high-resolution simulation with stars, and self-consistently follow the accretion and disruption of progenitor dwarfs and the build-up of the stellar halo in a cosmological "live host". We show how simple prescriptions for assigning stellar populations to collisionless particles are able to reproduce many properties of the observed MW halo and its surviving dwarf satellites, like velocity dispersions, sizes, brightness profiles, metallicities, and spatial distribution. More importantly, with over 1.6 million stellar particles tagged in post-processing, we can then mimic the observations of the line-of-sight velocity dispersion profiles of the simulated dSphs, apply a standard mass estimation algorithm based on spherical Jeans modelling, test the accuracy of this technique, and confirm or dispel the existence of a common mass scale for satellite galaxies.

A number of previous implementations of the particle-tagging approach exists in the literature (e.g. White & Springel 2000, Diemand et al. 2005, Bullock & Johnston 2005, Moore et al. 2006, Cooper et al. 2010, Tumlinson 2010). The approximation breaks down when baryons become dynamically important, i.e. in the inner regions of the MW and in the galactic disk. The orbits of some subhalos will pass through these regions, and one has to keep in mind and eventually correct for the fact that some substructure will actually feel the potential of baryonic configurations. Dwarf spheroidal satellites on the other hand seem to be dark matter-dominated on all scales, and our simulated subhalo potentials can be directly compared to the observed stellar kinematics. VLII's high mass resolution allows the survival of small dark matter subhalos long after they are accreted by the main host. Resolved at the present epoch with anywhere between 1,000 and 100,000 particles, these systems, in combination with an appropriate technique to designate stellar particles, serve as a testbed for the techniques commonly used to estimate the masses of dSph galaxies from real data.

This chapter has been published in the Astrophysical Journal as Rashkov et al. (2012) and is organized as follows. In § 2.2 we describe the VLII simulation and particle tagging technique, together with the resulting stellar halo and the population of dwarf satellites surviving today. In § 2.3 we describe the Jeans analysis used to estimate masses in pressure-supported collisionless systems, and assess its performance in correctly estimating the underlying mass distributions of the simulated dSph galaxies. We summarize our findings in § 2.4.

2.2 Simulation and particle tagging technique

The VLII simulation, one of the highest-precision calculations of the assembly of a Galactic halo to date (Diemand et al. 2008, Zemp et al. 2009), was performed with the PKDGRAV tree-code (Stadel 2001). Initial conditions were based on the WMAP 3-year data release cosmology (Spergel et al. 2007) and were generated with a modified, parallel version of the GRAFIC2 package (Bertschinger 2001). VLII employs just over one billion $4,100\ \mathrm{M}_\odot$ particles to model the formation of a $M_{200} = 1.9 \times 10^{12}\ \mathrm{M}_\odot$ Milky-Way size halo and its substruc-

Table 2.1: Build-up of the VLII stellar halo

Snapshot	Redshift	$N_{\rm halos}$	$M_*[{\rm M}_\odot]$	Snapshot	Redshift	$N_{\rm halos}$	$M_*[{\rm M}_\odot]$
0	27.54	0	-	13	1.37	61	3.63×10^3
1	23.13	0	-	14	1.16	45	6.86×10^5
2	17.88	0	-	15	0.98	22	4.45×10^5
3	14.78	0	-	16	0.83	17	1.50×10^7
4	12.71	3	4.48×10^0	17	0.70	12	9.84×10^4
5	11.20	24	9.83×10^3	18	0.58	15	2.01×10^4
6	9.14	190	1.89×10^5	19	0.48	14	6.07×10^3
7	7.77	530	4.25×10^8	20	0.39	6	1.18×10^1
8	4.56	1109	9.61×10^7	21	0.31	3	9.20×10^1
9	3.24	609	1.26×10^8	22	0.24	5	3.68×10^2
10	2.50	303	7.12×10^7	23	0.17	1	4.81×10^2
11	2.00	166	8.86×10^8	24	0.11	1	3.66×10^0
12	1.65	67	4.50×10^7	25	0.05	1	1.04×10^1
				26	0.00	0	-

Note. — Columns 1 and 2 give the VLII snapshot number and its corresponding redshift. Columns 3 and 4 list the number of subhalos that reached their maximum dark matter mass $M_{\rm h}$ in that snapshot, together with the total stellar mass they contribute to the VLII main host at $z = 0$.

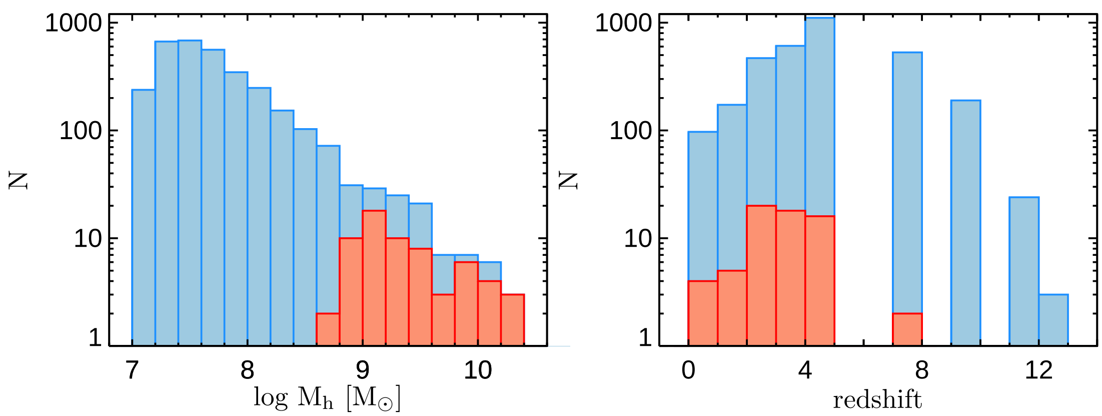

Figure 2.1: Distributions of the peak mass $M_{\rm h}$ at infall for 3,204 VLII subhalos (in blue) above $M_{\rm h} = 10^7$ M$_\odot$ (*left panel*) and of their infall redshift (*right panel*). Tagged subsets of dark matter particles in these systems are followed in post-processing from infall to the present. Subhalos that at $z = 0$ host a SDSS-detectable dSph populate the higher-mass and lower-redshift ends of these distrubutions (in red). The gaps in the redshift distribution correspond to $\Delta z = 1$ intervals where VLII snapshots were not analyzed in detail (see Table 2.1).

ture. About 40,000 subhalos of masses as low as 10^6 $M_\odot$ are resolved today within the host's $r_{200} = 402$ kpc (the radius enclosing an average density 200 times the mean matter value).

The particle tagging technique makes full use of 27 snapshots (out of 400 total) of the simulation, spanning the assembly history of the host between $z = 27.54$ and the present. Numbered from 0 to 26, the snapshots are listed in Table 2.1 together with the corresponding redshift. In each snapshot, all (sub)halos were identified with the 6DFOF group finder (Diemand et al. 2006), and linked from snapshot to snapshot to their most massive progenitor: the halo 'tracks' built in this way contain all the time-dependent structural information necessary for our study. We use them to identify the simulation snapshot in which each subhalo reaches its maximum mass $M_{\rm h}$ before being accreted by the main host and stripped. By neglecting all subhalos with $M_{\rm h} < 10^7$ $M_\odot$, we restrict our analysis to 3,204 such tracks that contribute mass to the main host halo at $z = 0$. The mass distribution of the selected subhalos at infall and the distribution of infall redshifts are shown in Figure 2.1. The gaps in the redshift histogram correspond to epochs in which no VLII snapshots were studied in detail (see Table 2.1). Due to the great computational effort necessary in the analysis of a single VLII snapshot, 6DFOF was applied only to the 27 ones listed here, and expanding this analysis to more snapshots is beyond the scope of our work. Halos that are accreted by the main host in these intervals are tagged at the next available snapshot. As the halos we consider are composed of a large number of particles, they are well resolved even ∼0.5-0.8 Gyr (typical snapshot separation) after accretion, making it unlikely that this time discretization affects significantly our results.

A subset of dark matter particles in each subhalo is then "tagged" as stars at infall, and no subsequent star formation is assumed to take place - hydrodynamical simulations suggest that ram pressure stripping would deplete the subhalo gas reservoir and shut star formation off shortly thereafter (e.g. Mayer et al. 2006). It is therefore at infall that tagged particles acquire a stellar mass $m_{\rm sp}$, an age $t_{\rm sp}$, and a metallicity $[{\rm Fe/H}]_{\rm sp}$: any subsequent evolution of the tagged stellar populations is purely photometric and kinematical in character, as systems age and are accreted and disrupted in a cosmological "live host".

The following three prescriptions determine $m_{\rm sp}$, $t_{\rm sp}$, and $[{\rm Fe/H}]_{\rm sp}$, and were tuned to match certain structural and statistical properties of the surviving dSph population at $z = 0$: the star formation efficiency $M_*/M_{\rm h}$ is fit to reproduce the satellite luminosity function, the selection of particles painted in halos is made to fit the current extent of their luminous component, and the assigned metallicities are designed to place satellites on the observed metallicity–luminosity relation today. The first two prescriptions thus determine the value $m_{\rm sp}$ for each tagged particle, while the third determines its $[{\rm Fe/H}]_{\rm sp}$. The age $t_{\rm sp}$ of the stellar population consistently follows from the star formation efficiency prescription and the history of dark matter build-up of the subhalo it was tagged in.

In the spirit of Koposov et al. (2009) and Kravtsov (2010), the total stellar mass tagged at infall is assumed to scale as a power-law of the host subhalo mass,

$$\frac{M_*}{M_{\rm h}} = 1.6 \times 10^{-5} \left(\frac{M_{\rm h}}{10^9\ {\rm M}_\odot}\right)^{1.8}. \tag{2.1}$$

Kravtsov (2010) used a slope of 1.5 but argued that the results would not change drastically if a somewhat steeper (2.0-2.5) slope was assumed. Koposov et al. (2009) similarly adopted a slope of 2.0. Our relation has a somewhat higher normalization than both. The difference likely arises from the conversion of the assigned stellar mass to a V-band luminosity. Koposov et al. (2009) assume a mass-to-light ratio $M/L = 1$ to be typical for old stellar populations, while we find that $M/L \sim 3 - 4$ better fits the range of ages and metallicities we assign to the infalling satellites (see below). A similar argument holds for the Kravtsov (2010) relation, which directly assigns a V-band luminosity to a halo of a given mass, instead of a stellar mass. Additionally, some of the halos in VLII lose a fraction of their stellar mass after accretion from tidal stripping, an effect that may not have been treated in the other two studies.

Our stellar mass-subhalo mass relation at infall has a scaling similar to the low-mass end ($M_h \sim 10^{11.5}$ M$_\odot$) galaxy stellar mass–halo virial mass relation, $M_*/M_h \propto M_h^{1.9}$, derived at $z = 1$ by Behroozi et al. (2010) using an abundance matching technique. It implies a star formation efficiency (the fraction of baryons turned into stars), $f_* \equiv (\Omega_M/\Omega_b)(M_*/M_\mathrm{h})$, that is close to 1% in $M_\mathrm{h} = 10^{10}$ M$_\odot$ subhalos, and becomes negligibly small in systems below $M_\mathrm{h} = 10^8$ M$_\odot$. The detailed physical explanation of this behavior is still an area of active research. Here we stress that it is the simple prescription in equation (2.1) that largely determines the luminosity function of surviving dwarf satellites today and empirically bypasses the missing satellite problem by strongly suppressing star formation in low-mass systems.

The total stellar mass within an infalling subhalo is equally distributed to its 1% most tightly bound dark matter particles. This number determines the concentration of the stellar system at the time of infall, and therefore governs the amount of stellar material stripped at later times as well as the present-day structural properties of surviving satellites, like their half-light radii and central surface brightnesses. Cooper et al. (2010) have shown that tagging the 1% highest total binding energy particles with stellar populations provides a good fit to the distribution of half-light radii in MW dSphs. Our analysis below confirms this result.

The metallicity assigned to each particle at infall is also a function of M_h,

$$[\mathrm{Fe/H}]_\mathrm{sp} = -7.87 + 0.9 \times \log\left(\frac{M_\mathrm{h}}{10^3\ \mathrm{M}_\odot}\right), \tag{2.2}$$

i.e. more massive subhalos are assumed to retain more of their enriched material and have a higher [Fe/H] than smaller systems. All particles initially tagged in the same subhalo are assigned the same metallicity. This prescription does not account for the timescale of enrichment of the stellar systems with iron or alpha-elements. In the present work metallicity only enters in the calculation of the luminosity of a given stellar system, and does not affect our kinematic studies. Two processes turn the above scaling into the observed present-day luminosity-metallicity relation of Kirby et al. (2008): (i) stellar mass loss from tidal stripping and (ii) dimming of the stellar populations with age (see the right panel of Fig. 2.3). When comparing the above relation to the one derived for SDSS galaxies, we note that it lies below the extrapolation of the Tremonti et al. (2004) relation. This suggests that processes governing metal formation and retention in dSphs may be significantly different from those in more massive galaxies.

Finally, while all particles in a given subhalo are tagged at a single epoch (infall), they have a distribution of stellar ages resulting from applying equation (2.1) to the history of dark matter build-up of each halo prior to its infall and assigning the respective age $t_{\rm sp}$ to the corresponding fraction of tagged stellar mass. This process mimics the extended star formation histories of dwarf satellites in the MW halo (see Orban et al. 2008).

After all stellar particles are tagged with the above properties, they are traced down to the $z = 0$ snapshot in the simulation. Some are still part of surviving dSph satellites; many form coherent stellar streams and contribute to the smooth stellar halo component. Their final V-band luminosities are self-consistently determined for their age, stellar mass, and metallicity from the stellar population synthesis models of Bruzual & Charlot (2003) (assuming a Chabrier initial mass function, Chabrier 2003).

2.2.1 Assembly history

A total of 1.6 million tagged particles end up in the main host at redshift $z = 0$ (0.35% of all particles within r_{200}): most are tidally stripped from their subhalos after infall, and only 52% of them remain bound to the 1,925 self-gravitating clumps that partially survive the accretion event. The total mass of the stellar halo today is $\mathcal{M}_* = 1.6 \times 10^9$ $\mathrm{M}_\odot$ within 402 kpc (of which 2.3×10^8 $\mathrm{M}_\odot$ is in bound substructures), and Table 2.1 lists the contribution to

$\mathcal{M}_*$ from each snapshot: the peak contribution comes from redshift 2. The mass in the stripped component between 1 kpc and 40 kpc is 5×10^8 M$_\odot$, comparable to recent estimates for the MW halo mass within the same range (Bell et al. 2008).

In terms of its mass assembly history, the stellar component of the VLII halo is already in place by redshift $z = 1.5$, while the dark component continues to grow from mergers with smaller subunits down to the present epoch. The faster assembly of the stellar component follows from the very steep mass-star formation efficiency relation adopted in our model. A similar behavior was seen in the assembly history of the six Aquarius stellar halos by Cooper et al. (2010). About 50% of today's stellar halo can be traced back to a subhalo of $M_* = 8.8 \times 10^8$ M$_\odot$ that fell in at $z = 2$. The three next most massive contributors, with $M_*/\,\mathrm{M}_\odot = (4.2 \times 10^8, 1.2 \times 10^8, 4.5 \times 10^7)$, were accreted at redshifts z =7.8, 3.2, and 1.6, respectively. Combined, these four progenitor systems account for about 88% of the total stellar halo.

Figure 2.2 shows an image of the projected VLII dark matter and stellar halo mass density at 3 different redshifts. The disruption of the stellar component of an individual satellite is depicted in the right panels, where particles initially tagged in one subhalo at infall (the system reaches its M_h at $z = 2$) are violently stripped by tides and form shell- and stream-like structures. The bottom left and middle panels make it clear how the adopted steep stellar mass-halo mass relation offers an empirical solution to the "missing satellite problem". While the dark halo exhibits a vast amount of surviving self-bound substructure, only the most massive subhalos form enough stellar mass at infall to still be visible in the stellar halo today.

2.2.2 Surviving satellites

Surviving satellites in the $z = 0$ VLII snapshot were identified by considering all particles that fall within the tidal radius of a bound subclump (identified in the dark matter density field by the 6DFOF group finder, see Diemand et al. 2006). We then performed a

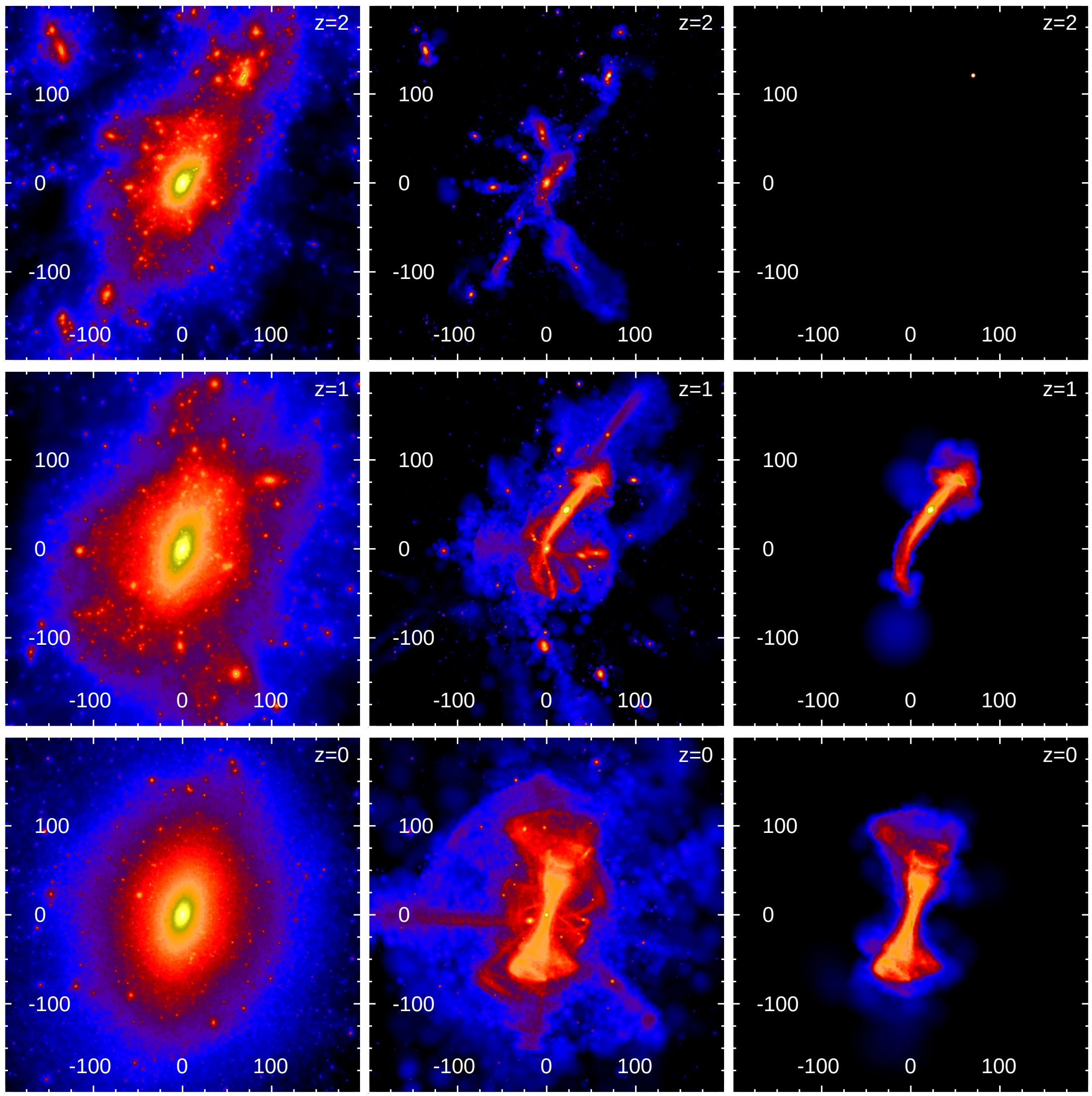

Figure 2.2: Projected mass surface density of the VLII dark matter halo (*left panels*) and its stellar halo (*central panels*), at redshift 2 (*top*), 1 (*middle*) and today (*bottom*). The image size is 400 physical kpc in all panels. For comparison, the r_{200} radius of the VLII dark matter halo is 94 kpc, 180 kpc, and 400 kpc at these 3 epochs, respectively. The color scale (from dark to bright) ranges from 2×10^5 $M_\odot\,\mathrm{kpc}^{-2}$ to 10^9 $M_\odot\,\mathrm{kpc}^{-2}$ for the dark matter, and from 10^{-2} $M_\odot\,\mathrm{kpc}^{-2}$ to 2×10^8 $M_\odot\,\mathrm{kpc}^{-2}$ for the stars. *Right panels:* the disruption of the stellar component of an individual satellite tagged at infall ($z = 2$).

peculiar velocity cut of $V_p \leq 2V_{\rm max}$ in order to remove particles belonging to the main halo that just happen to be flying through the given satellite at that time. The total luminosity of each satellite was computed by summing up the contributions of all stellar particles linked to it, and its metallicity determined from their mass-weighted average. Satellites of absolute magnitude M_V located closer than the SDSS completeness limit $r_{\rm max}$ (Tollerud et al. 2008) from the main halo center,

$$r_{\rm max} = \left(\frac{3}{4\pi f_{\rm DR5}}\right)^{1/3} \times 10^{(-0.6M_V-5.23)/3}\ \mathrm{Mpc}, \tag{2.3}$$

were flagged as observable in current surveys ($f_{\rm DR5} = 0.194$ here is the sky covering fraction of the SDSS DR5). Only 65 of the 1,925 surviving satellites present today in the VLII stellar halo are bright enough to be detected by an all-sky SDSS-like survey, out to a galactocentric distance of 280 kpc, corresponding to the Milky Way virial radius (Xue et al. 2008). Note that, as the SDSS detection efficiency is nearly independent of central surface brightness for $\mu_{0,V} \lesssim 30$ mag arcsec^{-2} (Koposov et al. 2008), no surface brightness threshold has been applied to our sample. We have checked that all but 13 of the observable VLII satellites have a central surface brightness of at least 30 mag arcsec^{-2}. The 13 low surface brightness systems are all faint ($M_V \gtrsim -5$) and have half-light radii $r_{\rm eff}$ close to the gravitational softening scale of the simulation, i.e. they have been artificially puffed up. We have estimated that, without such a numerical effect, these subhalos would actually lie above the SDSS surface brightness limit. Our prescriptions do not therefore produce a large population of low surface brightness "stealth" satellites awaiting discovery in the MW halo, as suggested by Bullock et al. (2010).

The stellar masses today of the observable VLII satellites range from $2,000\ \mathrm{M}_\odot$ to $10^8\ \mathrm{M}_\odot$, and their dark masses from $4\times10^6\ \mathrm{M}_\odot$ to $3\times10^9\ \mathrm{M}_\odot$. They have mass-to-light ratios that range from about 20 to 10^5, and infall redshifts mostly between 1.5 and 8 (with a few falling in later, between redshifts 0.6 and 1.1). Their mass-to-light ratios have decreased by a factor ranging between a few and 20, as their extended dark matter halos have been tidally stripped more than their compact luminous components. The ten most luminous satellites ($L > 10^6$ L$_\odot$) in the simulation are hosted by subhalos with peak circular velocities today in the range $V_{\rm max} = 10 - 40$ km s^{-1} that have shed between 80% and 99% of their dark mass after being accreted at redshifts $1.7 < z < 4.6$. Their $V_{\rm max}$ values have decreased by a factor of 2.5 on the average (and up to 6 in individual cases) after accretion, so their present-day $V_{\rm max}$ is not a good indicator of the subhalo maximum mass.

The differential satellite luminosity function is shown in the left panel of Figure 2.3, plotted against the luminosity function of observed MW dwarfs (see also works by Koposov et al. 2009, Macciò et al. 2010). As in Koposov et al. (2009), we use different scales for the number of satellites brighter and fainter than $M_{\rm V} = -11$, introduced to produce a continuous luminosity function despite the limited SDSS DR5 sky coverage of $f_{\rm DR5} = 0.194$. The shaded region to the left of $\rm M_V = -11$ spans the 1σ extent in the number of faint, but detectable satellites that fall within the SDSS DR5 footprint in each of 2,000 randomly oriented sky projections of the VLII stellar halo. In the case that the satellites are isotropically distributed, our exercise should produce a result equivalent to a scaling of the number counts of observed faint satellites by the sky coverage fraction of the SDSS survey. Satellites to the right of the dashed line, corresponding to $M_{\rm V} = -11$ are always detectable. The shaded region to the right of $\rm M_V = -11$ covers the 1σ Poisson errors in each bin there. The lack of Magellanic Cloud equivalents in VLII is responsible for the discrepant bright end of the luminosity function, as the simulation does not contain satellites more luminous than $M_V \lesssim -14$. Studies suggest that satellites this bright are rare around Milky Way-like galaxies (Boylan-Kolchin et al. 2010, Liu et al. 2011). In the right panel of the same figure, we plot the luminosity–metallicity relation of surviving satellites compared to data for MW dSphs (Kirby et al. 2008; and references therein) and their best-fit model to the data. The relation assumed at infall (eq. 2.2) has been modified by tidal mass losses and by the aging of stellar populations.

In Figure 2.4, the cumulative galactocentric distance distribution of VLII luminous subhalos is compared to that of MW satellites fainter than $M_V \geq -12$. Even though the final spatial distribution of dwarfs depends on their accretion and orbital history, the two distributions track each other reasonably well, though VLII shows an excess of close-in satellites compared to the observations. The figure also shows (right top panel) the present-day stellar mass–subhalo mass relation. Much like the metallicity–luminosity relation in Figure 2.3, it has been modified from its infall value by tidal mass losses. As accreted systems lose a disproportionate amount of their dark mass, the apparent (inferred today) star formation efficiency of dSphs may exceed the true one by as much as a factor of 100. We also explore (bottom left panel of Fig. 2.4) how the average 1-D line-of-sight velocity dispersion $\sigma_{\rm los}$ of dSphs (an observable quantity) compares to the peak (3-D) circular velocity $V_{\rm max}$ of the system's host halo (a quantity of theoretical interest). Early attempts at this conversion assumed a proportionality factor of $\sqrt{3}$ motivated by the isotropy of these systems (Moore et al. 1999). Our model suggests that the baryonic tracers are deeply embedded in their dark matter potentials today, resulting in higher values of $V_{\rm max}$, proportional to $2.2\sigma_{\rm los}$.[1] The difference is even more pronounced when comparing to the highest $V_{\rm max}$ values these systems ever achieved. Shown in the Figure as downward pointing triangles, these values indicate the amount of tidal mass loss that the subhalos hosting dSphs have undergone between infall and today. In Figure 2.5, we re-iterate this point by plotting the time evolution of $V_{\rm max}$ as a function of satellites' present-day luminosities.

Finally, we show how VLII dSphs compare to the Tully-Fisher relation (data from Pizagno et al. 2007) for disk galaxies (Fig. 2.4, bottom right panel). Just like the MW dSph population, our star formation prescription fails to produce dwarfs that lie on the extrapolated Tully-Fisher relation. The flattening of the distribution of spheroidal galaxies to a constant

[1]This ∼30% difference in $V_{\rm max}$ corresponds to a factor of 2 increase in total mass, $M \propto V_{\rm max}^3$.

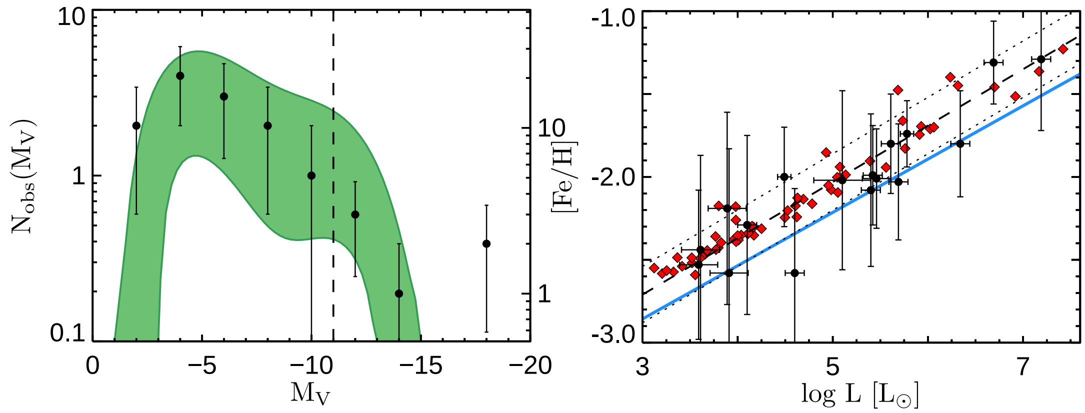

Figure 2.3: *Left panel:* Luminosity function of surviving satellites out to 280 kpc from the host halo center (*shaded in green*). Only galaxies that satisfy the magnitude-distance visibility SDSS criterion (see main text) are included. The shaded region for satellites fainter than $M_V = -11$ spans the difference in number of dSphs falling within the SDSS DR5 footprint from 2,000 randomly oriented sky projections of the VLII halo *Black dots:* differential luminosity function of known MW satellites (see Koposov et al. 2009). Error bars are indicative of Poisson number statistics in each magnitude bin. The lack of Magellanic Cloud equivalents in the VLII halo is apparent in the bright-end discrepancy between model and data. Note the different scales for the number of satellites fainter (left y-axis) and brighter (right y-axis) than $M_V = -11$, introduced to produce a continuous luminosity function despite the SDSS sky coverage of $f_{DR5} = 0.194$. *Right panel:* Evolution of the adopted metallicity–luminosity relation after tidal stripping and dimming of the stellar populations with time. The original prescription (eq. 2.2) assuming a mass-to-light ratio of unity is shown by a simple power-law (*solid blue line*). The stripping of stars from infalling satellites and the aging of stellar populations shifts luminosity to the left at a fixed value of [Fe/H]. *Red diamonds:* VLII satellites. The dashed and dotted lines show the observed metallicity–luminosity relation and 1σ spread from Kirby et al. (2008). *Black circles*: Milky Way dSphs; data from Kirby et al. (2008) and references therein.

velocity value in comparison to field spiral galaxies is reminiscent of the "common mass scale" seen in the M_{300} mass function (see Fig. 2.9), in which all currently detectable dSphs cluster around the value $M_{300} \sim 10^7$ $M_\odot$. As we shall see below, in our model the "common mass scale" is the result of a luminosity bias, and future detection of fainter dSph satellites would break it and reveal lighter dark matter subhalos hosting stellar systems.

We now turn to the structural properties of the surviving VLII dwarfs. For all satellites observable in an all-sky SDSS-like survey, we calculate the circularly-averaged surface brightness

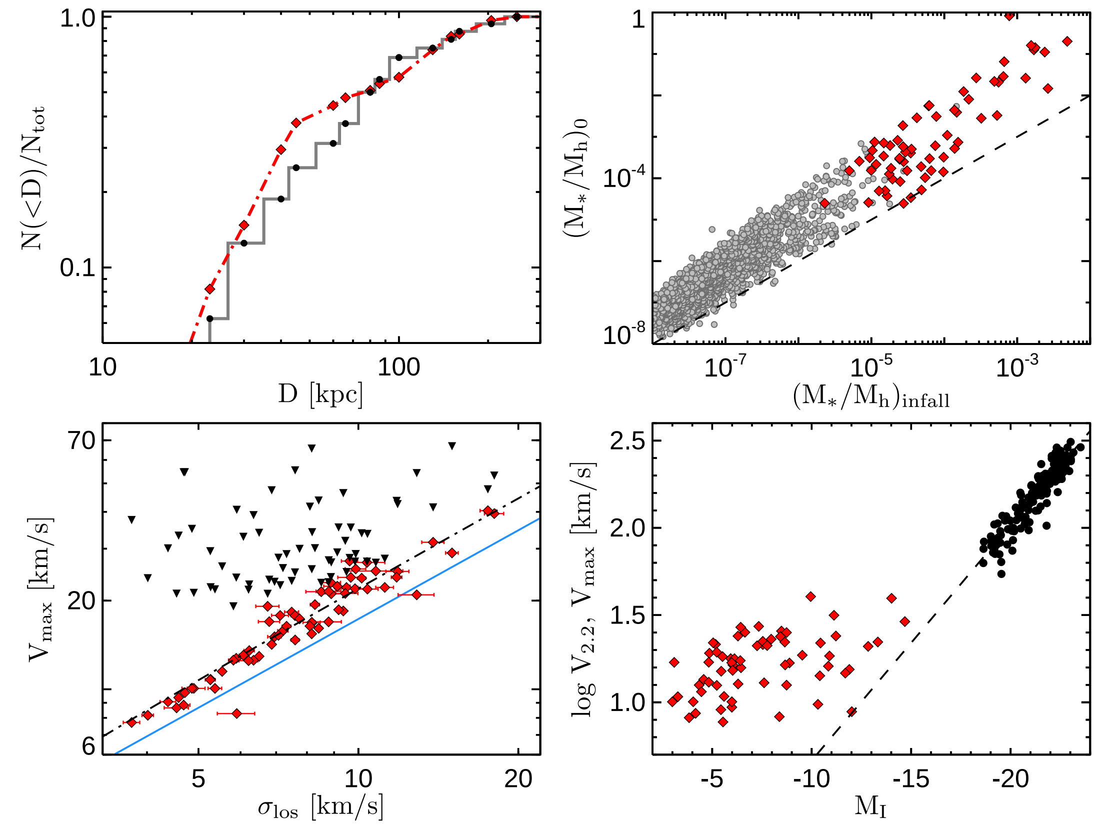

Figure 2.4: *Left top panel:* Cumulative distribution of galactocentric distance of VLII satellites fainter than $M_V \geq -12$, corresponding to the dSph satellites discovered by the SDSS. *Black circles:* Milky Way dSphs. *Red diamonds:* VLII satellites. *Right top panel:* Evolution of the stellar mass-halo mass relation from the infall epoch to the present in VLII surviving subhalos. *Red diamonds:* satellites detectable in an all-sky SDSS-like survey. *Grey dots:* all remaining (currently undetectable) satellites. The apparent increase in the star formation efficiency is caused by the preferential tidal stripping of the more diffuse dark matter component relative to the inner, more tightly bound stellar particles. *Left bottom panel:* Correspondence between 1-D line-of-sight velocity dispersion $\sigma_{\rm los}$ and 3-D maximum circular velocity $V_{\rm max}$ for observable VLII dSphs. *Solid blue line:* $V_{\rm max} \propto \sqrt{3}\sigma_{\rm los}$. *Red diamonds:* VLII detectable satellites. Error bars indicate 1σ variation over the 11 measurements of each profile used in our kinematic study. *Dashed line:* $V_{\rm max} \propto 2.2\sigma_{\rm los}$. *Black triangles:* Highest value of $V_{\rm max}$ ever achieved by each satellite. *Right bottom panel:* The $V_{\rm max}$−I band magnitude relation for surviving satellites (*red diamonds*) compared to to the Tully-Fisher relation of a broadly selected galaxy sample (*black dots*) from the SDSS (Pizagno et al. 2007). The dashed line gives the extrapolation of the best fit to the galaxy data. VLII dSphs clearly do not follow the relation.

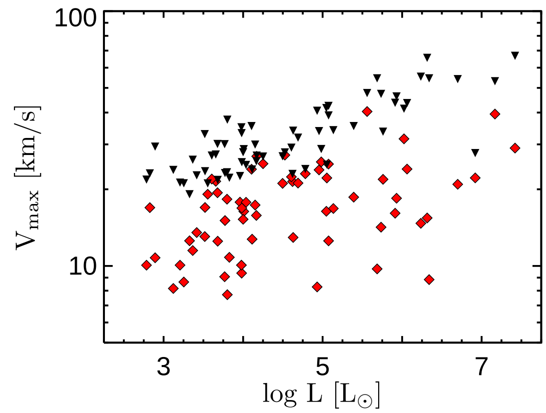

Figure 2.5: Comparison between the values of the 3-D maximum circular velocity $V_{\rm max}$ at infall and today as a function of the satellite's present-day luminosity, for observable VLII dSphs. *Red diamonds:* values of $V_{\rm max}$ today. *Black triangles:* the highest values of $V_{\rm max}$ ever achieved by each satellite. For the 10 most luminous satellites today, the $V_{\rm max}$ values have decreased by a factor of 2.5 on average (and up to 6 in individual cases) since accretion.

seen by a galactocentric observer and fit it with a 2-D projected King profile (King 1962),

$$I_*(R) = k \left[\left(1 + \frac{R^2}{r_k^2}\right)^{-1/2} - \left(1 + \frac{r_t^2}{r_k^2}\right)^{-1/2} \right]^2, \tag{2.4}$$

where $I_*(R)$ is the surface brightness at radius R from the satellite center, k is the profile normalization, r_k is the core radius of the satellite, and r_t is its tidal (cutoff) radius. This formula provides a good fit to the surface brightness profiles of MW dSphs (Mateo 1998), and has the advantage of having an analytical de-projected 3-D form in spherical geometry. Our use of the King profile as a fit to the projected surface brightness of VLII satellites instead of, say an exponential profile, is motivated by its standard use in published studies of dSph mass estimation. We find that the luminous component of the observable simulated dSph is well fit by a King profile across the full range of observable luminosities. Note that, while the tidal radii in the luminous component do not correspond to the physical truncation scale in the satellites' dark matter extent, the two scales are indeed comparable. On average, the ratio between the tidal radius in the luminous component and the tidal radius in the dark matter extent varies between 0.5 and 1 for satellites more luminous than $10^6 L_\odot$, while it is between 0.3 and 0.8 for fainter systems.

A comparison between the surface brightness and line-of-sight velocity dispersion profiles of two dSph satellites (Sculptor and Carina) and individual VLII counterparts is shown in Figure 2.6. Both surface brightness and kinematics should be compared only at radii larger than twice the VLII softening length of 40 pc, as the artificial "heating" of particles inside this region from numerical resolution effects would give a poor match to the data. In the surface brightness plot, we show the diverse light profiles of all VLII dwarfs that have a luminosity within $\pm 80\%$ of the corresponding MW satellite. Equally diverse is the span of velocity dispersion profiles these dwarfs have, with values ranging between $4\,\mathrm{km\,s^{-1}}$ and $15\,\mathrm{km\,s^{-1}}$, pointing to the differences between the potential wells in which these systems reside. The insets in the figure show the evolution of the luminous systems' parameters (King profile core and tidal radii and half-light radii) from 'tagging' (infall) until today. The behavior seen here is representative of the other SDSS detectable dwarfs in VLII - the core radii increase with time (though they remain close to the simulation softening length), while the half-light and tidal radii decrease as the satellites lose stars from their outskirts to the main halo. In the velocity dispersion plots, we try to reproduce the 'noisy' observed profile by sparsely sampling the simulation data. Using the same number of stellar particles in each corresponding bin as the one in the observed profile (M. Walker, private communication), we note that the scatter in the simulated profile increases significantly.

In a systematic analysis, Strigari et al. (2010) have shown that at least one simultaneously structural and kinematic counterpart to each of the five classical dSph with good kinematic and photometric data can be found in the Aquarius simulations. Our ability to obtain simultaneous brightness and kinematic fits for dSphs like Sculptor and Carina can be seen as a confirmation of their results and a success of our model, and is a prerequisite for testing the "common mass scale" of MW satellites. Structural parameters of the VLII satellite population (half-light radii and velocity dispersions measured directly from the particle data, and central surface brightnesses from the King model fits as a function of absolute magnitude) are compared to the observed properties of MW dSphs in Figure 2.7. The agreement is reasonably good. Reproducing the properties of the luminous component of dSph galaxies is a necessary condition for generating realistic "mock" data to test the mass measurement technique.

2.3 Kinematics of dwarf spheroidal satellites

2.3.1 The spherical Jeans equation

The Jeans equation is the first moment over velocity of the collisionless Boltzmann equation. It provides a link between the underlying potential of a pressure-supported system and the distribution function of a tracer population in equilibrium with it. In spherical geometry its radial component is:

$$r\frac{d\left(\nu_*\sigma_r^2\right)}{dr} = -\nu_* V_c^2 - 2\beta\nu_*\sigma_r^2, \tag{2.5}$$

where $\nu_*(r)$ is the luminosity density profile of the tracer stars, σ_r is their radial velocity dispersion, and $\beta = 1 - \sigma_t^2/\sigma_r^2$ is the velocity anisotropy, i.e. the difference between the radial, σ_r, and the tangential, $\sigma_t^2 = (\sigma_\theta^2 + \sigma_\phi^2)/2$, components of the velocity dispersion. Here, $V_c(r)$ is the circular velocity profile of the system, a measure of the underlying gravitational potential Φ,

$$V_c(r)^2 = G\frac{M(< r)}{r} = -r\frac{d\Phi}{dr}. \tag{2.6}$$

Since 3-D kinematic data for MW dSph stars are not available, one has to use a 1-D projection of the spherical Jeans equation along the line-of-sight between the observer and the studied system. This introduces an additional geometric effect involving the velocity anisotropy

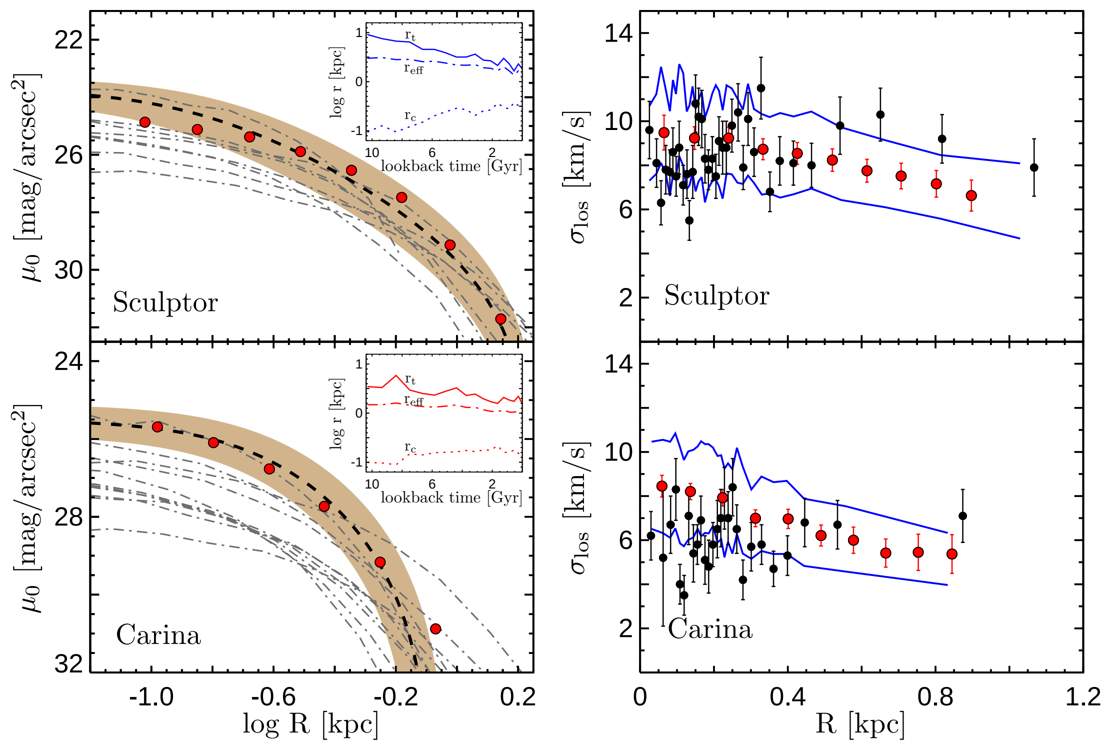

Figure 2.6: Surface brightness and velocity dispersion profiles of two VLII satellites (*red dots*) closely resembling the Milky Way dSph Sculptor and Carina. Error bars are indicative of 1σ Bootstrap re-sampling errors in each bin. Simulated surface brightness and kinematics should be compared only for $R > 80$ pc, corresponding to twice the VLII softening length. The observed surface brightness profiles are plotted with dashed lines and the uncertainty is shown by the shaded region. Brightness fits for Sculptor and Carina are taken from Mateo (1998), while the kinematic data (*black dots with error bars*) are from Walker et al. (2009). Also shown is the diversity in brightness profiles among VLII satellites with luminosities within $\pm 80\%$ of Sculptor's and Carina's (*grey dot-dashed lines*). The insets follow the evolution of the King profile structural parameters for the fiducial satellites from the time of 'tagging' (infall) until today. *Solid blue lines:* the 95% confidence region in the kinematic profiles where the data are sparsely sampled as the observations.

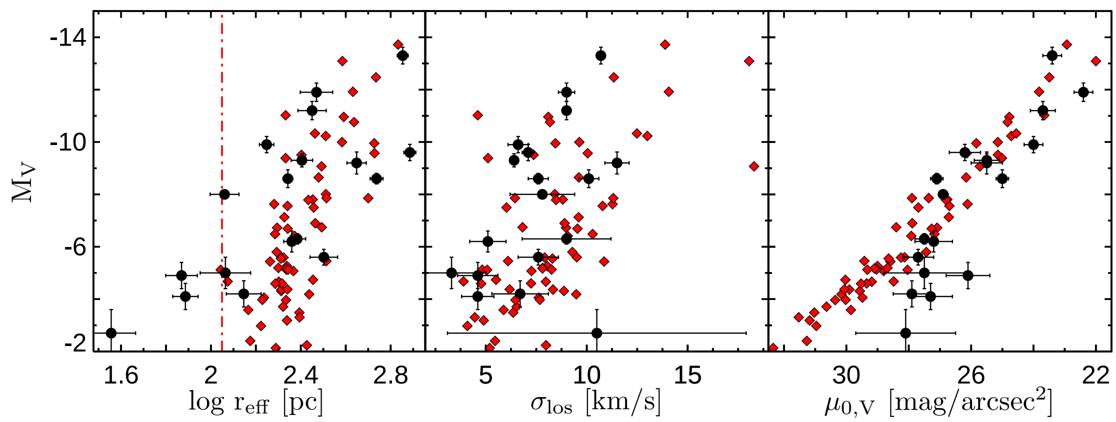

Figure 2.7: Structural properties of surviving VLII satellites. Plotted against V-band absolute magnitude are their half-light radii (*left panel*), line-of-sight velocity dispersions (*middle panel*), and central surface brightnesses (*right panel*). *Red diamonds:* observable VLII dwarfs. *Black circles with error bars:* Milky Way dSph. Data compiled as follows: M_V: *classical dwarfs:* (Mateo 1998), except for *Leo II* (Coleman et al. 2007), *ultra-faint dwarfs:* (Martin et al. 2008), except for *Hercules* (Sand et al. 2009) and *Leo T* (de Jong et al. 2008); $r_{\rm eff}$ and $\sigma_{\rm los}$: Wolf et al. (2010); $\mu_{0,\rm V}$: *classical dwarfs;* (Mateo 1998), except for *Draco* (Martin et al. 2008), *ultra-faint dwarfs:* (Martin et al. 2008), except for *Leo T* (Irwin et al. 2007). The dash-dot red vertical line in the left panel marks 2.8× the VLII softening length of 40 pc (see Cooper et al. 2010).

(Binney & Tremaine 2008):

$$\sigma^2_{\rm los}(R) = \frac{2}{I_*(R)} \int_R^\infty \left(1 - \beta \frac{R^2}{r^2}\right) \frac{\nu_* \sigma_r^2 r}{\sqrt{r^2 - R^2}} dr, \tag{2.7}$$

where $I_*(R)$ is the projected surface brightness profile of the tracer population. Of all quantities involved in the projected Jeans equation, $\sigma_{\rm los}$ and $I_*(R)$ are readily determined observationally, and $\nu_*(r)$ can be obtained through a de-projection of the surface brightness profile, assuming it follows some analytical form - either a spherical King (1962) or a Plummer (1911) profile. Both of these profiles adequately fit the light distribution of MW satellites and the choice of one or the other does not affect the results of our kinematic study (Strigari et al. 2008). The remaining parameters, namely $\beta(r)$ and $V_c(r)$, are not constrained observationally and have to be modeled appropriately.

We adopt a generalized NFW profile (Navarro et al. 1996) for the mass distribution of subhalos:

$$\rho(r) = \frac{\rho_s}{(r/r_s)^{\gamma}(1 + r/r_s)^{\delta}}, \tag{2.8}$$

where ρ_s gives the density normalization, r_s is the scale radius, and γ and δ define the inner and outer slopes of the density fall-off. The fiducial NFW form has $\gamma = 1$ and $\delta = 2$. To allow for a range of inner density cusps as well as outer tidally-modified profiles, we allow these two parameters to vary in the intervals $0.7 \lesssim \gamma \lesssim 1.2$ and $2 \lesssim \delta \lesssim 3$ (Strigari et al. 2007). We have verified that the upper limit on the outer slope δ is high enough to accommodate the profiles of even the most massive VLII subhalos, whose density profiles fall off faster than those of field halos in the tidally-stripped outer regions (Diemand et al. 2008).

The velocity anisotropy parameter β is largely unconstrained by current observations. According to its definition, β can vary between $-\infty$ and 1, with $\beta = -\infty$ when $\sigma_{\rm tot} = \sigma_t$ and $\beta = 1$ when $\sigma_{\rm tot} = \sigma_r$. Available data are often in the form of 1-D line-of-sight velocity dispersion, insufficient to constrain σ_r and σ_t individually. These two quantities are well determined only at the very center and very edge of a system, since $\sigma_{\rm los}(0) = \sigma_r$ and $\sigma_{\rm los}(r_t) = \sigma_t$. In between these two extremes, the mass of a dSph enclosed within a radius close to the system's half-light radius can be calculated such that the uncertainty from the velocity anisotropy term is minimized (Wolf et al. 2010). At any other intermediate radius, the β parameter will more strongly affect the mass measurement and must be estimated using a theoretical model. In principle, β can be a function of radius within a particular system (Strigari et al. 2007). Previous studies have shown that marginalizing over a set of parameters that define a general anisotropy profile does not constrain the mass distribution better than assuming β to be constant with radius (Walker et al. 2009). The latter case, however, greatly simplifies the solution to the spherical Jeans equation (Mamon & Łokas 2005):

$$\nu_* \sigma_r^2(R) = G R^{-2\beta} \int_R^\infty r^{2\beta-2} \nu_*(r) M(r) dr. \tag{2.9}$$

The standard procedure in mass modeling of pressure-supported systems is to generate a theoretical velocity dispersion profile that fits the observed one, and to marginalize the solution over all free parameters but the density profile normalization. While most model parameters are largely unconstrained by this fitting procedure, the density profile normalization (defined as the total amount of mass enclosed in a fixed aperture radius, typically 300 pc or 600 pc) is very well determined by the data (Strigari et al. 2008, Walker et al. 2009). It is this analysis that yields the so-called "common mass scale" of MW dSph satellites.

2.3.2 Applications to VLII dwarf satellites

We apply the mass measurement technique above to the simulated data using the following procedure:

1. Obtain $\sigma_{\rm los}(R)$ and $I_*(R)$ for a satellite of interest;
2. Choose the density profile and anisotropy parameters ρ_s, r_s, γ, δ, and β;
3. Integrate the Jeans equation (2.5) to solve for $\sigma_r(r)$;
4. Project $\sigma_r(r)$ along the line of sight (eq. 2.7);
5. Compare the solution to the measured $\sigma_{\rm los}(R)$;
6. Iterate (2 - 5) to find the model that best matches the kinematic data.

Once the best fit mass density profile is determined, we integrate it to a given aperture radius, either 300 pc or 600 pc from the satellite center to obtain the total enclosed mass, M_{300}

or M_{600}, and compare it directly to the "true" value in the simulation. To obtain the "mock" observations of VLII dSphs in step 1, we place "hypothetical observers" in the simulation volume, and reduce computational time by "observing" each of the 65 detectable satellites only 11 times. One of the "observers" is always in the center of the VLII main host, while the other 10 are randomly distributed at the same distance from the satellite as the galactocentric "observer". In this way we attempt to capture the anisotropy of subhalos' physical shapes and velocity ellipsoids.

Since integrating the Jeans equation requires a boundary condition on $\sigma_r(r_t)$, which is not known a priori from the data, the line-of-sight projected solution cannot be trusted across the full extent of the surface brightness fit. The observed line-of-sight velocity dispersion profile is therefore calculated in 10 linear distance bins out to 60% of each satellite's tidal radius r_t. The simulated data used to determine each subhalo's kinematic profile do not have an associated observational uncertainty. To make a fair comparison with the derived mass estimates, "observational" errors should be consistent with the ones in the current literature (Walker et al. 2009). This is done by randomly assigning error values σ_i ranging between 1 and 2 $\mathrm{km\,s^{-1}}$ to the velocity dispersion data when evaluating the goodness of fit in equation (2.10) below.

Sample line-of-sight velocity dispersion profiles for two VLII simulated satellites and their assigned "observational" errors are shown in the top left panel of Figure 2.8. The two satellites have masses of $M_{300} = 7.22 \times 10^6$ $\mathrm{M}_\odot$ and $M_{300} = 2.65 \times 10^7$ $\mathrm{M}_\odot$, respectively. For each satellite, we plot all 11 best fit $\sigma_{\mathrm{los}}(R)$ profiles. The two sets of data points (in black and grey) correspond to the kinematic profile fits highlighted in darker colors, which were chosen to the span the range of M_{300} for which the fit's likelihood falls to 10% of its peak value (see the right top panel of Fig. 2.8). The average M_{300} values inferred from these 11 fits are 6.65×10^6 $\mathrm{M}_\odot$ and 2.44×10^7 $\mathrm{M}_\odot$ respectively, within 8% of the true values.

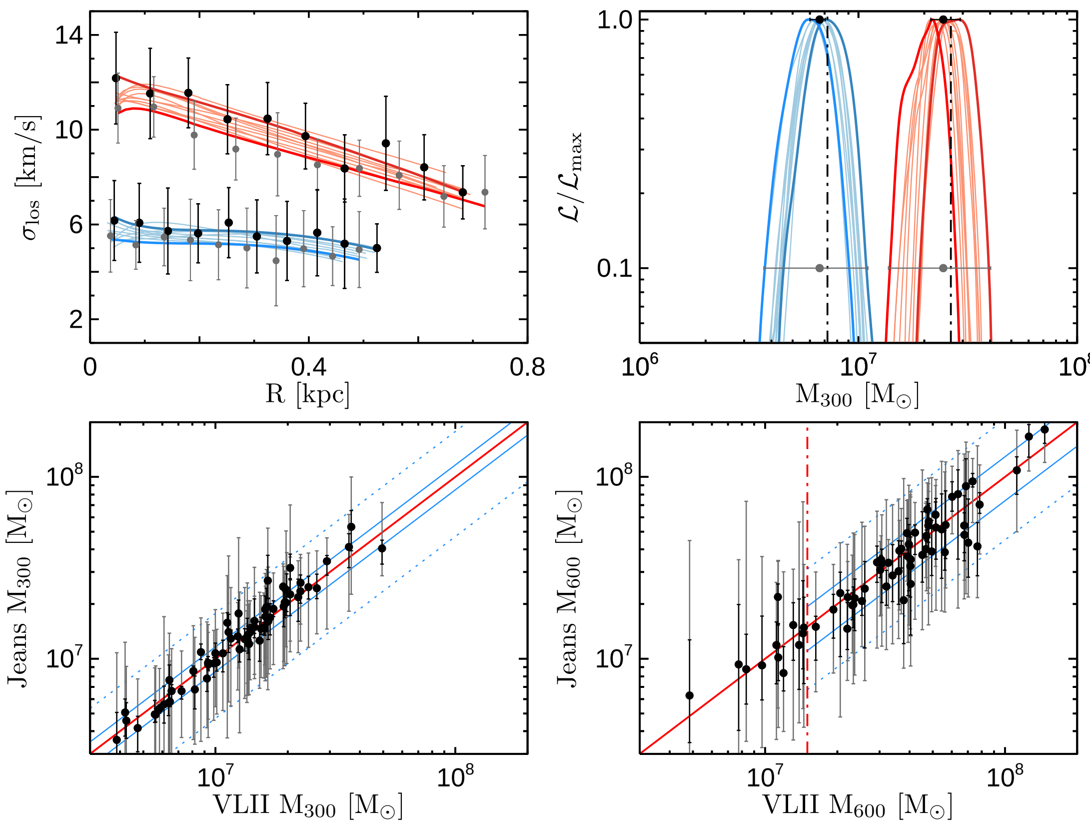

Figure 2.8: *Left top panel:* Sample line-of-sight velocity dispersion profiles for two VLII dSph, of masses $M_{300} = 7.22 \times 10^6$ $\mathrm{M}_\odot$ and $M_{300} = 2.65 \times 10^7$ $\mathrm{M}_\odot$. Best fit Jeans solutions for $\sigma_{\rm los}(R)$ plotted in red and blue. Fits highlighted in darker colors correspond to the points with error bars and the envelope 10% likelihood functions shown in the right top panel. The average best fit estimates of M_{300} in this case are 6.65×10^6 $\mathrm{M}_\odot$ and 2.44×10^7 $\mathrm{M}_\odot$ respectively. *Right top panel:* Likelihood functions of M_{300} for the two satellites in the left panel. The 11 realizations span a range in the best fit values around their mean (black dots with error bars) as well as a range in uncertainty where the likelihood has fallen to 10% of the best fit value (grey error bars). The vertical dot-dash lines indicate the true VLII values of M_{300}. *Left bottom panel:* Total mass within the inner 300 pc, M_{300} as determined through the Jeans equation in comparison with its true value from VLII. Mean values of 11 individual measurements are plotted with black points. Black error bars span the range between best fit values, while the grey error bars span the full range of values where the likelihood of the fit has fallen to 10% of its peak value. *Solid red line:* Unity correspondence. *Solid blue lines:* Average over the full M_{300} mass range of the spread among the best-fit measurements. *Dotted blue lines:* Average over the full M_{300} mass range of the spread among measurements where the likelihood is 10% of its peak. *Right bottom panel:* Total mass within the inner 600 pc, M_{600} as determined through the Jeans equation in comparison with its true value from VLII. Labels as in the M_{300} panel on the left. Systems with $M_{600} \lesssim 1.5 \times 10^7$ $\mathrm{M}_\odot$ (left of the red dash-dot line) do not have kinematic data out to $r = 600$ pc, which results in a larger scatter in their estimated M_{600} values.

To get the above estimates, we fit a model to each "observed" kinematic profile using a Monte Carlo Markov Chain (MCMC). A theoretical velocity dispersion profile $\sigma_{\rm los,th}(R)$ is computed for each parameter set in step 2. and the likelihood of the fit is evaluated as:

$$\mathcal{L} = \prod_i \frac{1}{\sqrt{2\pi\sigma_i^2}} \exp\left[-\frac{1}{2}\frac{(\sigma_{\rm los}(R_i) - \sigma_{\rm los,th}(R_i))^2}{\sigma_i^2}\right] \tag{2.10}$$

where $\sigma_{\rm los}(R_i)$ is the line-of-sight velocity dispersion measured at radius R_i and σ_i is its associated error. Each MCMC chain is initialized to maximize the likelihood $\mathcal{L}$ on a coarse model grid that spans the full parameter space. It is then left to explore the parameter space following the Metropolis-Hastings algorithm. Two concurrent chains are run on each data set and the MCMC is stopped after 10,000 attempts of each chain. This number is large enough to provide satisfactory fits to the kinematic data (Walker et al. 2009). The 11 resulting likelihood functions for M_{300} of the two satellites above are shown in the right top panel in Figure 2.8.

Once the best-fit model for each data set has been found, it provides the full mass density profile that can be integrated to any distance from the dSph center, with 300 pc or 600 pc being of particular interest. There are 11 likelihood distributions for the estimates of M_{300} and M_{600} of each VLII satellite, and these can be compared to the true values. The results are shown in the bottom panels of Figure 2.8, in which we plot the average of the 11 best mass estimates as a function of the true dark matter mass. The nature of the MCMC data allows us to make two estimates for the error in each case. The smaller error bars (in black) in Figure 2.8 reflect the span of the 11 best fit values for each satellite. The larger errors (in grey) span the full range in values where the likelihood of the fit has fallen to 10% of its maximum value. For the particular two satellites in the top panels of Figure 2.8, we thus have the following mass estimates: $M_{300} = 6.65^{+0.41+4.40}_{-0.64-2.95} \times 10^6 M_\odot$ for the lower-mass satellite and $M_{300} = 2.44^{+0.48+1.48}_{-0.30-1.07} \times 10^7 M_\odot$ for the higher-mass one, where the first set of errors corresponds to the best fit value range and the second set of errors corresponds to the 10% likelihood value range.

We infer that the spherical Jeans analysis is a robust method to estimate the central masses of dSph satellite galaxies. The mean best fit M_{300} values determined through the Jeans analysis are on average within 12% of the true VLII values. The normalized scatter among the 11 best fits about the mean value is $^{+0.16}_{-0.15}$ on average and is shown as solid lines in the bottom panels of Figure 2.8. The normalized full range scatter about the mean where the likelihood of the fit is greater than 10% of its peak value is $^{+0.78}_{-0.53}$ on average (dashed lines). No significant difference to these results arises when just the galactocentric observer's estimates are considered: the best fit galactocentric estimate of M_{300} across the full mass range is on average within 16% of the true VLII value.

When evaluating M_{600}, we exclude systems that have $M_{600} \lesssim 1.5 \times 10^7$ M$_\odot$. It is apparent in the bottom right panel of Figure 2.8 that these exhibit a larger scatter than the systems with $M_{600} \geq 1.5 \times 10^7$ M$_\odot$. The smallest dSphs host stellar systems smaller than 0.6 kpc in radial extent. The estimate of M_{600} for them is therefore an extrapolation to a region in parameter space where tracers are simply not present. Among the dSphs with kinematic data available all the way to $r = 0.6$ kpc, the mean best fit M_{600} value determined with the Jeans analysis is on average within 17% of the true VLII value. The normalized scatter among the 11 best fits about the mean value is $^{+0.29}_{-0.26}$ on average. The normalized full range scatter about the mean where the likelihood of the fit is greater than 10% of its peak value is $^{+1.08}_{-0.55}$ on average. The VLII galactocentric observer would report a M_{600} value within 23% of the true VLII value.

The range in $\sigma_{\rm los}(R)$ and $I_*(R)$ when measured from different viewpoints is due to the anisotropic velocity tensor of the dSph and any deviation from perfect sphericity of its shape. The mass estimate uncertainties among the best-fit values presented here should therefore be regarded as intrinsic, cosmologically-induced ones that will eventually be minimized when 3-D

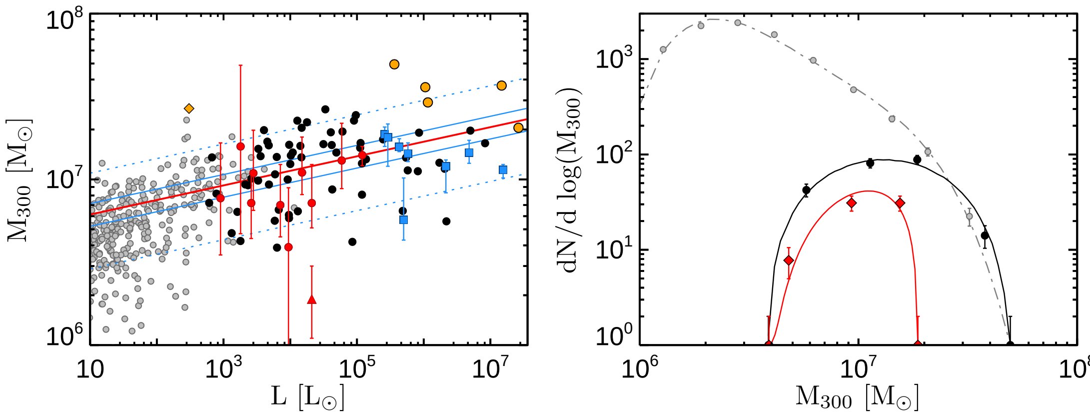

Figure 2.9: *Left panel:* Total mass within the central 300 pc, M_{300} as a function of total luminosity for dwarf satellites in VLII visible by an all-sky SDSS-like survey (black dots). Currently undetectable VLII dwarfs are shown in grey. A linear best fit to the data with slope 0.088 is shown with a red solid line. Data points with error bars are from Strigari et al. (2008), indicating a "common mass scale". These error bars correspond to the points where the likelihood is 60.6% of its peak value on either side of the best estimate. For comparison, we plot our average error estimates in M_{300} from Figure 2.8 about the best fit (*solid red line*): *solid blue lines:* full spread in best-fit estimates; *dotted blue lines:* full spread in values where the likelihood is 10% of its peak. The "classical" dSphs ($L \geq 2 \times 10^5$ $L_\odot$) are shown as blue squares and the "ultra-faint" dSphs as red circles. The improved mass for the Hercules dwarf from Adén et al. (2009) is shown as a red upward pointing triangle. The six VLII subhalos identified by Boylan-Kolchin et al. (2011) as too dense to host any of the known MW dSphs are plotted in orange as five circles (if detectable) and a single diamond (currently undetectable). *Right panel:* M_{300} mass function for VLII dSph satellites. *Red diamonds:* MW dSphs with masses taken from (Strigari et al. 2008). *Black dots:* VLII satellites detectable in SDSS. *Grey dots:* all VLII surviving subhalos that were tagged with stars, including those currently undetectable. The "common mass scale" is apparent in the currently detectable population.

kinematic data is collected and better models of the nature of dSph satellites in high-resolution, fully cosmological hydrodynamical simulations are carried out.

In the left panel of Figure 2.9, we plot the mass enclosed in the inner 300 pc versus total luminosity for all satellites that would be visible according to the SDSS detection limit. Overplotted are data from Strigari et al. (2008), suggesting a "common mass scale". Observable VLII dSphs exhibit a behavior similar to the MW dSph population, though a linear fit suggests a shallow but significant correlation between M_{300} and the total luminosity: $M_{300} \propto L^{0.088\pm0.024}$, where the error on the slope reflects the 1σ deviation from bootstrap re-sampling of the sample. This is steeper than the $L^{0.03\pm0.03}$ relation derived from observational data (Strigari et al. 2008). Lowering the derived M_{300} values of some of the ultra-faint dSphs, as suggested by Adén et al. (2009) for the case of the Hercules dwarf, might be sufficient to reconcile the observations with the slope predicted from our model.

In our model, the nearly constant M_{300} is explained by the combination of the steep adopted stellar mass-halo mass relation (eq. 2.1) and the SDSS detectability magnitude limit. The remaining $\sim 2,000$ VLII surviving subhalos to which we assigned stars (about 200 of which are more luminous than $M_{\rm V} = 0$) are just too faint to be detected by a SDSS-like survey. Some of them have M_{300} significantly lower than 10^7 $M_\odot$ (see the right panel of Figure 2.9).

Boylan-Kolchin et al. (2011) has recently pointed out that state-of-the-art collisionless simulations of Galactic structure, both VLII and Aquarius, predict a population of massive subhalos that appear to be too dense (i.e. have too high a $V_{\rm max}$ for a given $r_{\rm vmax}$) to host any of the known MW dSph. While a failure of the CDM model is one interpretation of this result, another possibility is that star formation becomes stochastic below some mass, in which case the MW halo would harbor several massive but dark satellites. It is also quite plausible that baryonic feedback processes in the more massive subhalos redistribute some of their dark matter, thereby lowering their central density (see e.g. Governato et al. 2010). For reference we have marked the six VLII subhalos that are too dense according to the Boylan-Kolchin et al. (2011) analysis in the left panel of Figure 2.9. Of these six, five have a luminosity greater than $M_V = -11$ and would have been detected as luminous dSph satellites. In our model, it is thus not possible for these overdense subhalos to have evaded detection because of an effectively low star formation efficiency resulting, for example, from their accretion or orbital history. As expected, these six halos have the highest values of M_{300} for their luminosity among all VLII satellites. A reduction in M_{300} by about a factor of two would bring them into agreement with the classical MW dSph sample. Our study of the standard Jeans analysis demonstrates that the 'observed' M_{300} values cannot be changed by that amount, i.e. that errors in the mass estimates are not responsible for the discrepancy between the models and the observations. Future, high-resolution hydrodynamical simulations of MW analogs that include an accurate treatment of baryonic processes and their effects on the central densities of luminous satellites will be crucial to the settling of this outstanding issue.

2.4 Summary

We have used a particle tagging technique to dynamically populate the N-body *Via Lactea II* high-resolution simulation with stars. The method is calibrated using the observed luminosity function of MW satellites, the concentration of their stellar populations, and the metallicity–luminosity correlation they exhibit, and self-consistently follows the accretion and disruption of progenitor dwarfs and the build-up of the stellar halo. The particle tagging technique makes full use of 27 simulation snapshots spanning the assembly history of the VLII main host between $z = 27.54$ and $z = 0$. A subset of the most bound dark matter particles in each of about 3,200 progenitor subhalos is tagged as stars at infall, when star particles acquire a stellar mass, an age, and a metallicity. Their subsequent evolution is purely photometric and kinematical in character, as the collisionless stellar populations age following population synthesis models, and are accreted and disrupted in a comological "live host". Luminous particles linked to self-bound substructures in the $z = 0$ snapshot constitute a surviving population of dSph satellites. Like the previous studies of Bullock & Johnston (2005) and Cooper et al. (2010), we have shown that simple prescriptions for assigning stellar populations to collisionless particles are able to reproduce many properties of the MW dwarf satellite population, like velocity dispersions, sizes, brightness profiles, metallicities, and spatial distribution. In agreement with previous results (e.g. Kravtsov 2010, Koposov et al. 2009, Madau et al. 2008b), a steep stellar mass-subhalo mass relation is required to fit the observed luminosity function of MW dSphs and offer an empirical solution to the missing satellite problem. This model predicts the existence of approximately 1,850 subhalos harboring "extremely faint" satellites (with mass-to-light ratios $> 5 \times 10^3$) lying beyond the SDSS detection threshold. Of these, about 20 are "first galaxies", i.e. they formed a stellar mass above 10 $M_\odot$ before redshift 9. The ten most luminous satellites ($L > 10^6$ $L_\odot$) in the simulation are hosted by subhalos with peak circular velocities today in the range $V_{\rm max} = 10 - 40$ $\rm km\,s^{-1}$ that have shed between 80% and 99% of their dark mass after being accreted at redshifts $1.7 < z < 4.6$. The satellite maximum circular velocity $V_{\rm max}$ and stellar line-of-sight velocity dispersion $\sigma_{\rm los}$ today follow the relation $V_{\rm max} = 2.2\sigma_{\rm los}$, i.e. stellar particles in satellites have smaller velocity dispersions than the dark matter. The ability to obtain simultaneous brightness and kinematic fits for dSphs like Sculptor and Carina is a confirmation of earlier searches for MW satellite counterparts in simulated halos such as the one by Strigari et al. (2010) and a success of our model. It is a prerequisite for studying another small-scale puzzle of galaxy formation in ΛCDM, namely the observed "common mass scale" of MW satellites, i.e. the fact that, despite spanning about 5 decades in luminosity, MW dSphs appear to contain a similar amount of dark mass, $M_{300} \sim 10^7$ $M_\odot$, within a fixed aperture radius of 300 pc from their centers (Strigari et al. 2008, Walker et al. 2009). We have applied a standard mass estimation algorithm based on Jeans modelling of the line-of-sight velocity dispersion profiles to the simulated VLII dwarf spheroidals, and tested the accuracy of this technique. We have shown that the mass enclosed within the inner 300 pc can be estimated accurately to within 20% of the true value. The predicted M_{300}-luminosity relation for currently detectable simulated satellites is nearly flat. We do, however, predict a weak, but significant positive correlation for these objects: $M_{300} \propto L^{0.088 \pm 0.024}$. Our results are consistent with previous studies in which satellites observable by presently available wide-field surveys naturally tend to reside in subhalos that contain about 10^7 $M_\odot$ within their inner 300 pc. Future, even deeper surveys with the *Large Synoptic Survey Telescope* may be able to determine if an extension of this satellite galaxy population, at an even fainter magnitudes, indeed exists in the halo of the Milky Way. These experiments will cast light on the processes that govern galaxy formation on even smaller scales predicted in ΛCDM cosmology. Ultimately, the prescriptions used in this work must be tested with hydrodynamical simulations that include baryonic physics. Simulations of the formation of late-type spiral galaxies in a cold dark matter (ΛCDM) universe have traditionally failed to yield realistic candidates. Our group has recently reported a new cosmological hydrodynamic simulation of extreme dynamic range, "Eris", in which a close analog of a Milky Way disk galaxy arises naturally at the present epoch (Guedes et al. 2011). With a mass resolution that is ~ 20 times lower than VLII, Eris includes radiative cooling, heating from a cosmic UV field and supernova explosions (blastwave feedback), a star formation recipe based on a high gas density threshold, and neglects any feedback from an active galactic nucleus.

Chapter 3

A Population of Relic Intermediate-Mass Black Holes in the Halo of the Milky Way

3.1 Introduction

Direct dynamical measurements show that most local massive galaxies host a quiescent massive black hole (MBH) in their nuclei. Their masses have been found to correlate tightly with the mass (Häring & Rix 2004) and the stellar velocity dispersion of the host stellar bulge, as manifested in the $M_{\rm BH} - \sigma_*$ relation of spheroids (Ferrarese & Merritt 2000, Gebhardt et al. 2000). It is not yet understood whether such scaling relations were set in primordial structures and maintained throughout cosmic time with a small dispersion, or indeed which physical processes established such correlations in the first place. It is also unclear whether there exists a minimum host galaxy mass or velocity dispersion below which MBHs are unable to form or grow. The subset of the MBHs that populates the centers of dwarf galaxies and very late spirals and is undergoing accretion can be detected as active galactic nuclei (AGNs). Observations of AGNs with estimated black hole masses in the range 10^5-10^6 $M_\odot$ appear to be consistent with an extrapolation of the local $M_{\rm BH} - \sigma_*$ relation for inactive galaxies down to stellar velocity dispersions of 30 $\rm km\,s^{-1}$ (Barth et al. 2005, Xiao et al. 2011). The existence of "intermediate-mass" black holes (IMBHs) with 20 $M_\odot < M_{\rm BH} < 10^5$ $M_\odot$ remains in dispute. Dynamical mass measurements have shown the presence of IMBH candidates in the cores of the globular clusters G1 ($M_{\rm BH} = 1.8 \pm 0.5 \times 10^4$ $M_\odot$, Gebhardt et al. 2005), ω Centauri ($M_{\rm BH} = 4.7 \pm 1.0 \times 10^4$ $M_\odot$, Noyola et al. 2010), NGC 1904 and 6266 ($M_{\rm BH} = 3 \pm 1 \times 10^3$ $M_\odot$ and $M_{\rm BH} = 2 \pm 1 \times 10^3$ $M_\odot$, Lützgendorf et al. 2012). The X-ray spectra and bolometric luminosities of the ultraluminous off-nuclear X-ray sources detected in nearby galaxies may imply the presence of IMBHs with $M_{\rm BH} \gtrsim 500$ $M_\odot$ (Farrell et al. 2009, Kaaret et al. 2001).

While the "seeds" of the MBHs powering the $z \gtrsim 6$ *Sloan Digital Sky Survey* (SDSS) very luminous, rare quasars (Fan 2006) must have appeared at very high redshifts and grown rapidly to more than 10^9 $M_\odot$ in less than a Gyr, the problem of their origin and occupation fraction in early galaxies remains unsolved. MBHs may have grown from the remnants of Population III (Pop III) star formation in sub-dwarf galaxies at $z \gtrsim 15$ (e.g. Madau & Rees 2001, Volonteri et al. 2003, Tanaka & Haiman 2009), or from more massive precursors formed by the "direct collapse" of large amounts of gas in dwarf galaxy systems at later times (Loeb & Rasio 1994, Koushiappas et al. 2004, Begelman et al. 2006, Lodato & Natarajan 2006, Mayer et al. 2010). Massive seeds have larger masses than Pop III remnants, but form in rarer hosts. Questions remain in the Pop III remnant model about the ability of $\sim$ 100 $M_\odot$ seed holes to grow at the Eddington rate for tens of e-folding times unimpeded by feedback, and in the direct collapse model about the needed large supply of low angular momentum gas that must accumulate in the center of young galaxies before fragmentation and star formation sets in (see, e.g., Haiman 2012 and references therein).

In this chapter we assess the size, properties, and detectability of the leftover population of IMBHs[1] that is predicted to survive today in the halo of the Milky Way (MW) galaxy by two fiducial seeding scenarios. It was first pointed out by Madau & Rees (2001) that, if seed holes were indeed common in the subgalactic building blocks that merged to form the present-day massive galaxies, then a numerous population of relic IMBHs should be present in the Galactic bulge and halo (see also Volonteri et al. 2003, Islam et al. 2003, Volonteri & Perna 2005). Micic et al. (2006; 2011) used collisionless simulations to study the effect of gravitational recoil kicks on the IMBH distribution in present-day galaxies and test merger-driven recipes for black hole growth. van Wassenhove et al. (2010) ran Monte Carlo realizations of the merger history of massive galaxy halos to study IMBHs in MW satellites at $z = 0$. A similar approach was employed by O'Leary & Loeb (2009) to estimate the expected number of recoiled IMBH remnants present today in the MW halo. Cosmological hydrodynamic simulations of the growth of MBHs are either limited by resolution to galaxy hosts with $M_{\rm halo} \gtrsim 10^{10}$ M$_\odot$ (e.g. Di Matteo et al. 2008) or stop at high redshift (e.g. Bellovary et al. 2011). In all approaches seed holes are planted by hand. To improve on and complement the above calculations, we use here a *particle tagging technique* to dynamically populate the N-body *Via Lactea II* (VLII) extreme-resolution simulation with IMBHs. As we shall discuss, this method allows us to self-consistently follow the accretion and disruption of MW progenitor dwarfs and the kinematics of their holes in a cosmological "live" host, and the build-up of a large population of Galactic "naked" wandering IMBHs. This chapter has been submitted to the Astrophysical Journal for publication as Rashkov & Madau (2013).

[1]In the following, we will use the term IMBH to refer to any hole with 20 M$_\odot$ $< M_{\rm BH} < 10^5$ M$_\odot$, i.e. more massive than the stellar-mass black holes found in X-ray emitting binary systems (Orosz et al. 2007) and 40 times less massive than Sgr A*.

3.2 Black Hole Tagging Technique

The cosmological ΛCDM VLII simulation, one of the highest-precision N-body calculations of the assembly of the Galactic halo to date (Diemand et al. 2008), was performed with the PKDGRAV tree-code (Stadel 2001). It employs just over one billion $4,100\ \mathrm{M_\odot}$ particles to model the formation of a $M_{200} = 1.93 \times 10^{12}\ \mathrm{M_\odot}$ Milky Way-sized halo and its substructure. About 20,000 surviving subhalos of masses above $10^6\ \mathrm{M_\odot}$ are resolved today within the main host's $r_{200} = 402$ kpc (the radius enclosing an average density 200 times the mean matter value). Central black holes are added to subhalos following the particle tagging technique detailed in Rashkov et al. (2012) and quickly summarized here. In each of 27 (out of the 400 available) snapshots of the simulation, chosen to span the assembly history of the host between redshift $z = 27.54$ and the present, all subhalos are identified and linked from snapshot to snapshot to their most massive progenitor: the subhalo tracks built in this way contain all the time-dependent structural information necessary for our study. We then: 1) identify the simulation snapshot in which each subhalo reaches its maximum mass, $M_{\rm halo}$, before being accreted by the main host and tidally stripped; 2) measure the subhalo maximum circular velocity $V_{\rm max}$; 3) link it to the stellar line-of-sight velocity dispersion, σ_*, using the relation $V_{\rm max} = 2.2\sigma_*$ derived by Rashkov et al. (2012); and 4) tag *the most tightly bound central particle* as a black hole of mass $M_{\rm BH}$ according to an extrapolation of the $M_{\rm BH} - \sigma_*$ relation of Tremaine et al. (2002),

$$\frac{M_{\rm BH}}{\mathrm{M_\odot}} = \begin{cases} 10^{6.91} \left(\frac{\sigma_*}{100\ \mathrm{km\,s^{-1}}}\right)^4 & (\sigma_* \geq 6\ \mathrm{km\,s^{-1}}) \\ 100 & (\sigma_* < 6\ \mathrm{km\,s^{-1}}). \end{cases} \tag{3.1}$$

Note that significantly steeper $M_{\rm BH} - \sigma_*$ relations have been derived recently by, e.g. Graham et al. (2011) and McConnell & Ma (2013). We will discuss the impact of a steeper power-law on our results in the journal article.

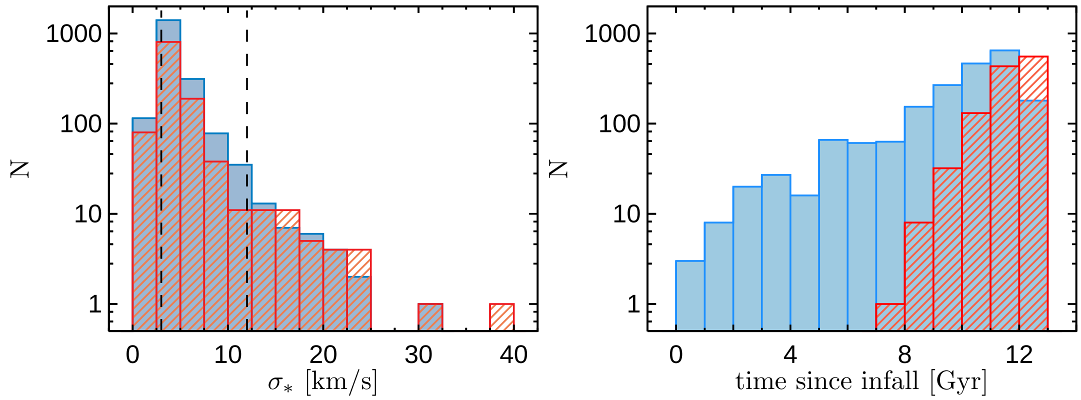

Figure 3.1: Histograms of the stellar velocity dispersion at infall (*left panel*) and infall lookback time (*right panel*) for all subhalos with $M_{\rm halo} > 10^7$ M$_\odot$ in the VLII simulation. The color coding separates self-gravitating subhalos that survive their accretion event and become MW satellites (*blue*) from those that are totally disrupted (*red*). The vertical lines in the left panel mark the minimum velocity dispersion below which central black holes are assumed to be increasingly rare in the two seeding scenarios discussed in the text.

By neglecting all subhalos with $M_{\rm halo} < 10^7$ M$_\odot$, we restrict our analysis to 3,204 such tracks. Any evolution of the tagged holes after infall is purely kinematical in character, as their satellite hosts are accreted and disrupted in an evolving Milky Way-sized halo. After tagging, the black hole particles are tracked down to the $z = 0$ snapshot. The main host is assigned a central black hole at $z = 0$ of mass equal to that of Sgr A*, $M_{\rm BH} = 4 \times 10^6$ M$_\odot$ (Ghez et al. 2008). While we tag at most one hole per subhalo, we allow multiple systems to form when subhalos merge after infall (see below).

Figure 3.1 shows the distributions of stellar velocity dispersion at infall (left panel) and time since infall (right panel) for the VLII subhalo population. The color coding separates self-gravitating subhalos that survive their accretion event and become MW satellites from those that are totally disrupted. The latter are found to fall in preferentially at earlier times, and have a median infall redshift of 4.5.

3.3 Demography of IMBHs

Below we discuss two simple models of seed hole formation that may be illustrative of more realistic growth scenarios, and differ only in the black hole occupation fraction as a function of the host's stellar velocity dispersion.

3.3.1 Population III Remnants

Let us first consider a scenario where the black hole occupation fraction is of order unity at infall in all subhalos with stellar velocity dispersions $\geq \sigma_m = 3\ \mathrm{km\,s^{-1}}$ and drops to zero below σ_m. This value is comparable to the stellar velocity dispersion measured today in the ultra-faint MW satellite Segue 1 (Simon et al. 2011), i.e. this model places seed holes in small-mass subhalos that are known to have been rather inefficient at forming stars (e.g. Rashkov et al. 2012, Cooper et al. 2010, Koposov et al. 2009). The mass distribution of subhalos with $\sigma_* > 3\ \mathrm{km\,s^{-1}}$ at infall has a median of $5 \times 10^7\ \mathrm{M_\odot}$. We assign black holes masses following the relation (3.1). As most of the subhalos in Fig. 3.1 host then a 100 $\mathrm{M_\odot}$ black hole, we refer to this model as "Pop III remnants".

Two large subpopulations of Galactic black holes can then be readily identified today within r_{200}, 798 "naked" IMBHs, whose host subhalos have been totally disrupted after infall, and 1,234 "clothed" IMBHs residing in satellites that survived tidal stripping. Within the latter category, 1,096 are single black hole systems, i.e. are located in subhalos that host only one hole at the present epoch. The others are multiple systems: we find 42 dwarf subhalos with 2 holes, 7 with 3, 5 with 4, and 1 with each of 6 and 7 holes. These multiple systems are produced when their host subhalos merge together after infall, as they fall into the main halo in groups. We assume that by that time, ram pressure stripping has removed any leftover gas from the system, making it difficult for IMBHs to sink to the center of the potential well and merge.

Substructures that host 5 or more IMBHs are found to be more than 250 kpc from the Galactic center and have masses in the range $2 \times 10^9 - 3 \times 10^9$ $M_\odot$ today. Figure 3.2 (left panels) shows an image of the projected spatial distribution of IMBHs in today's inner and outer Galactic halo according to this model, while Figure 3.3 depicts their mass function and radial distribution. Naked holes are more concentrated towards the inner halo regions as a consequence of the tidal disruption of infalling satellites. Indeed, within 10 kpc of the center, most IMBHs are naked. The second most massive hole (after "Sgr A*") has $M_{\rm BH} = 8.6 \times 10^4$ $M_\odot$ (i.e. was tagged at infall in a large satellite with $\sigma_* = 32$ km s^{-1}), is naked, and is located at a distance of 55 kpc from the center. There are 48 IMBHs above $M_{\rm BH} = 10^3$ $M_\odot$, of which 29 are naked. Most holes are assigned the seed mass of 100 $M_\odot$, i.e. they are not allowed to grow in this model: we count a total of 1,801 such "light" IMBHs, of which 695 are naked.

3.3.2 Direct Collapse Precursors

Consider by contrast a scenario where more massive seeds form in rarer hosts. Models in which seed black holes become very rare for halos with $M_{\rm halo} \lesssim 10^9$ $M_\odot$ have been recently discussed by, e.g., Bellovary et al. (2011) and Devecchi et al. (2012). Here, we take the hole occupation fraction to be of order unity in all subhalos with stellar velocity dispersions $\geq \sigma_m = 12$ km s^{-1}, and to drop to zero below σ_m. Black hole masses are again assigned following equation (3.1) down to σ_m. The mass distribution of subahalos hosting central black holes at infall now has a median of 3×10^9 $M_\odot$, and the minimum hole mass is $M_{\rm BH} \simeq 1,700$ $M_\odot$.

This tagging prescription gives origin to 39 naked and 33 clothed IMBHs (of which 27 are single systems). Figure 3.2 (right panels) shows an image of the projected spatial distribution of IMBHs in today's inner and outer Galactic halo according to this model, while Figure 3.3 (left panel) depicts their mass function. There are 20 IMBHs above $M_{\rm BH} = 10^4$ $M_\odot$, of which 13 are naked.

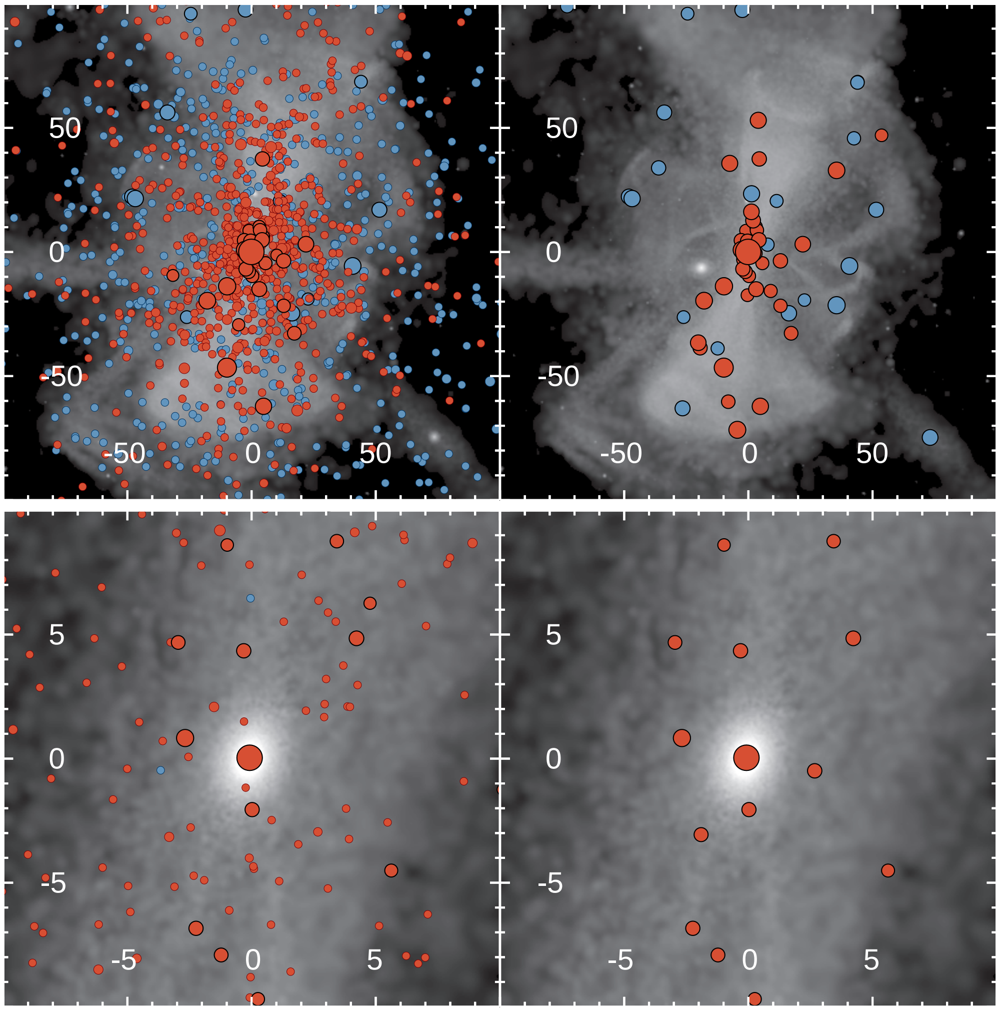

Figure 3.2: Projected distribution of IMBHs in the Galactic halo today. *Left panels:* Pop III remnant model. *Right panels:* Direct collapse progenitor model. The color coding is as in Fig. 3.1, while the size of the points is proportional to $\log_{10} M_{\rm BH}$. The stellar halo from Rashkov et al. (2012) is plotted in the background. *Top row:* 200 kpc box. *Bottom row:* Zoom-in of the inner 20 kpc region.

3.4 Black Hole Recoils

The asymmetric emission of gravitational waves produced during the coalescence of a binary black hole system imparts a velocity kick to the system that can displace the hole from the center of its host. The magnitude of the recoil will depend on the binary mass ratio and the direction and magnitude of their spins (Baker et al. 2008), but not on the total mass of the binary. When the kick velocity is larger than the escape speed of the host halo, a hole may be ejected into intergalactic space before becoming a Galactic IMBH. The demography of IMBHs discussed in the previous section accounts for recoiling holes as follows.

Following the results of high-resolution self-consistent gasdynamical simulations of binary mergers of disk galaxies by Kazantzidis et al. (2005), we assume that unequal-mass galaxy mergers with mass ratios larger than 4:1 will not lead to the formation of a close black hole pair at the center of the remnant, and hence of a recoiling hole. All major mergers (mass ratios smaller than 4:1) produce instead recoiling holes with a kick velocity that is equal to the most likely value of the probability distribution function for randomly oriented spins (see Fig. 3 of Guedes et al. 2011). In practice, this means that all recoiling holes will have speeds in excess of 100 $\mathrm{km\,s^{-1}}$ and will be ejected from the system. This is a conservative assumption in the sense that it tends to minimize the actual number of relic IMBHs in the Galactic halo. We trace all $<$4:1 halo mergers following the VLII merger tree back to redshift 10. This was built by identifying all subhalos in each snapshot with the 6DFOF halo finder (Diemand et al. 2006), and linking them from one snapshot to the next by the id numbers of the shared particles. We identify all halos that would have been assigned a hole at infall, but had in their past a $<$4:1 major merger with another black hole-hosting system. As the kick velocity is always larger than the escape speed from the host, the hole is removed from the final catalog of Galactic IMBHs.

The size of the recoiling population is clearly very sensitive to the hole occupation

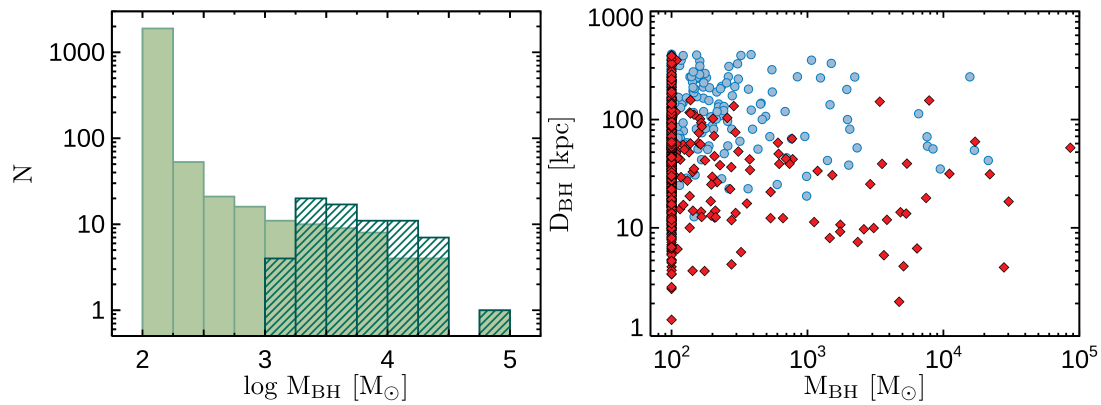

Figure 3.3: *Left panel:* Mass function of relic IMBHs within r_{200} in the two scenarios discussed in the text. *Solid histogram:* Pop III remnants. *Hatched histogram:* Direct collapse precursors. *Right panel:* Location of "naked" (*red diamonds*) and "clothed" (*blue circles*) IMBHs in the $M_{\rm BH}$-Galactocentric distance plane for the Pop III model. Naked IMBHs are more concentrated towards the inner halo regions, a trend that is also observed in the direct collapse, massive seed scenario.

Table 3.1: Demography of Galactic IMBHs

Model	Population III	Direct Collapse
σ_m [km s^{-1}]	3.0	12.0
med($M_{\rm halo}$) [$M_\odot$]	5×10^7	3×10^9
$N_{\rm naked}$	798	39
$N_{\rm clothed}$	1234	33
$N_{\rm massive}(M_{\rm BH} > 5,000$ M$_\odot$)	21	37
min($M_{\rm BH}$) [$M_\odot$]	1.0×10^2	1.7×10^3
max($M_{\rm BH}$) [$M_\odot$]	1.9×10^5	1.9×10^5
$N_{\rm recoil}$	577	5

Note. — Row 1 indicates the seeding scenario, rows 2, 3, 4, 5, 6, 7, 8, and 9 give the minimum subhalo line-of-sight stellar velocity dispersion required for hosting a central black hole, the median halo mass at infall, the number of "naked" and "clothed" Galactic IMBHs, the number of Galactic IMBHs more massive than 5000 M$_\odot$, the mass of the lightest and heaviest Galactic IMBHs, and the number of recoiled IMBHs, respectively.

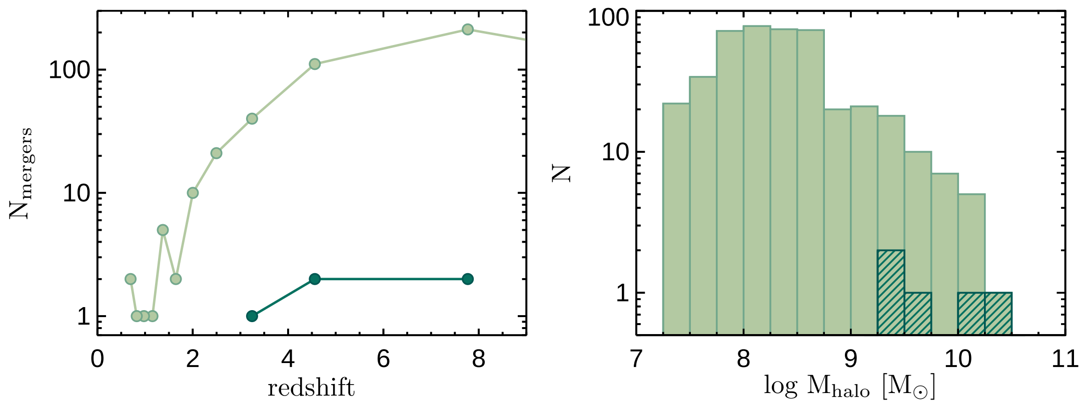

Figure 3.4: *Left panel:* Number of subhalo major mergers that produce a recoiling IMBH, as a function of redshift. *Light green curve:* Pop III remnants model. *Dark green curve:* Direct collapse precursors. *Right panel:* Mass distribution (at infall) of all the subhalos whose central black holes were ejected following a major merger. The color scheme is the same as in the top panel.

fraction. Figure 3.4 shows the total number of halo major mergers that produce recoiling IMBHs in the "Pop III" and "direct collapse" seed scenarios. The former produces 577 recoiling holes (22% of the total black hole population), mostly belonging to $\sim 10^8$ $M_\odot$ subhalos at infall. The latter produces only 5 recoiling holes (6% of the total) all from rather massive hosts. Note that it is because of recoils that the number of Galactic IMBHs heavier than a few thousand solar masses is actually larger in the direct collapse model (see Fig. 3.3). The demography of Galactic IMBHs in our two scenarios is summarized in Table 3.1.

3.5 Spatial Distribution of IMBHs

The spatial distribution of Galactic IMBHs today is shown in Figure 3.5. Naked holes dominate in the inner ~ 50 kpc from the halo center. Their number density, however, plummets at larger distances, where most IMBHs are still hosted in surviving substructures. This is a manifestation of the fact that subhalos orbiting closer to the dense central regions of the main host are more likely to be tidally disrupted, and leave their IMBHs exposed. In the outer halo

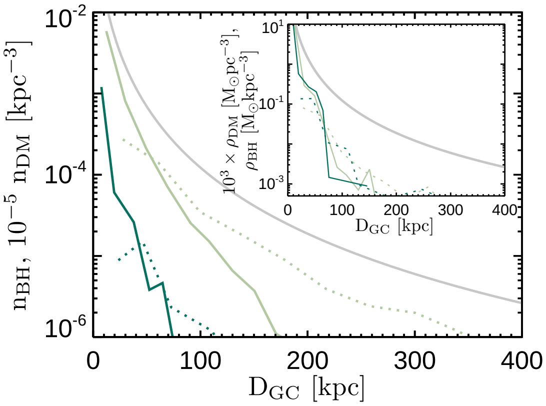

Figure 3.5: Spatial distribution of Galactic IMBHs versus the dark matter density profile in VLII. *Main panel:* IMBH number density *Inset:* IMBH mass density. The mass density of the dark matter has been multiplied by a factor of 1,000 for comparison. *Light green:* Pop III remnants scenario, naked (*solid curves*) and clothed (*dotted curves*) IMBHs. *Dark green:* direct collapse progenitors scenario, naked (*solid curves*) and clothed (*dotted curves*) IMBHs. *Gray:* VLII dark matter density profile. The total number density of IMBHs follows the dark matter density profile, while their mass density does not.

regions, the lower background density makes substructures more resilient to tidal forces, allowing them to survive and retain their holes. A comparison of the IMBH number density to the density profile of the dark matter shows that the cumulative distribution of Galactic IMBHs (naked plus clothed) follows the dark matter profile rather well, but that each individual subpopulation does not. The inset in Figure 3.5 shows that the IMBH mass density profile does not follow the density profile of the dark matter, as most of the mass in black holes is concentrated in the inner regions.

Since naked IMBHs more massive than dark matter particles do not experience proper dynamical friction in our simulation, we have estimated a posteriori the effect of black hole orbital decay in two different ways – using the slowly-decaying circular orbit approximation, as well as computing the instantaneous deceleration from dynamical friction (Binney & Tremaine 2008) in each available VLII snapshot. We find that, even for the heaviest IMBHs in the highest density regions of our simulation, dynamical friction timescales exceed the Hubble time at all points along the orbit. A similar conclusion was reached by O'Leary & Loeb (2009) in their study. Of course, our N-body simulation does not account for possible hydrodynamical effects and interactions with the galaxy stellar disk in the very center of the VLII halo.

3.6 Discussion

We have used a particle tagging technique to populate the subgalactic building blocks of a present-day MW-sized galaxy with black holes, and assess the size, properties, and detectability of the leftover population. Our approach combines a computationally expensive, extreme-resolution, N-body simulation like VLII, in which structures grow ab initio in a fully cosmological framework, with simple prescriptions for seeding, in post-processing, progenitor subhalos with IMBHs. Insofar baryonic material does not appreciably perturb the collisionless dynamics of the N-body component, the dynamical association of black holes with individual particles in the N-body component should correctly reproduce the spatial and kinematic properties of IMBHs in galaxy halos, in particular of the naked subpopulation whose host satellite galaxies have been totally destroyed after infall. This level of detail is unavailable to a standard merger-tree approach.

We have discussed two simple models of seed hole formation that may be illustrative of more realistic growth scenarios, a "Pop III remnant" model in which small-mass black holes populate subhalos with stellar velocity dispersion as low as 3 $\mathrm{km\,s^{-1}}$, and a "direct collapse precursor" model in which holes become very rare in systems with stellar velocity dispersion below 12 $\mathrm{km\,s^{-1}}$, and are more massive. It is important to keep in mind that the Pop III route does not necessarily require the formation of extremely massive stars from gas of primordial composition. Already at metallicities $Z \lesssim 0.01\,Z_{\odot}$, the mass loss rates of massive stars through radiatively driven stellar winds are predicted to be rather small (with rates decreasing with

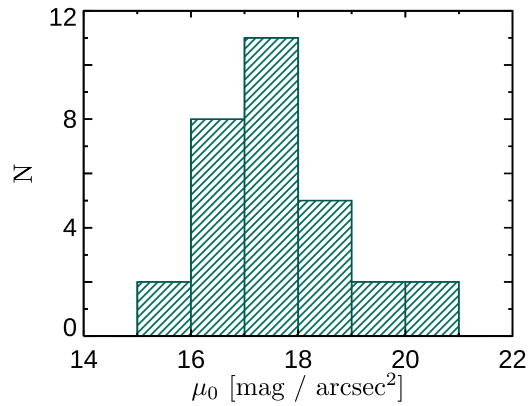

Figure 3.6: Distribution of V-band peak surface brightness (within the central 1 arcsec) of stellar cusps around naked IMBHs in the "direct collapse" model. Only 20% of the initial stellar mass (equal to $2 \times M_{\rm BH}$) is assumed to be retained today. To account for the partial SDSS sky coverage, the expected numbers should be scaled down by a factor of $\sim$5.

metallicity as $\dot{M} \propto Z^{0.69}$, see Vink et al. 2001). If low-metallicity stars above 50 $M_\odot$ collapse to black holes after losing only a small fraction of their initial mass, then IMBHs with masses above the $5 - 20$ $M_\odot$ range of known "stellar-mass" holes may be the inevitable end product of early star formation. A standard Salpeter initial mass function (IMF), $dN/dm_* \propto m_*^{-2.35}$ in the range $1 - 100$ $M_\odot$, would produce an IMBH every 1000 $M_\odot$ of stars formed. A top-heavy IMF like that found in recent simulations of primordial star formation by Stacy & Bromm (2012), $dN/dm_* \propto m_*^{-0.17}$, over the same $1 - 100$ $M_\odot$ mass range, would generate an IMBH every 100 $M_\odot$ of stars formed. Note that 1000 $M_\odot$ of stars in a 5×10^7 $M_\odot$ subhalo imply a star formation efficiency that is much too high to match the observed dearth of faint Milky Way satellites (e.g. Rashkov et al. 2012), *and a top-heavy IMF must then be invoked for consistency.*

Galactic IMBHs may light up if they pass through dense regions of the galaxy and accrete from the interstellar medium (Volonteri & Perna 2005). IMBHs present in the lensing galaxy of multiply-imaged background QSOs will produce monopole- or dipole-like distortions in the surface brightness of the QSO images and may be detectable by next generation submillimeter telescopes with high angular resolution (Inoue et al. 2013). It is interesting at this stage to discuss the observability of the stellar cusps that may accompany naked IMBHs wandering in the Milky Way halo. After the complete disruption of their host subhalo, naked IMBHs are still expected to carry with them a Bahcall-Wolf stellar cusp (Merritt et al. 2009) which, upon formation and in the absence of a kick from gravitational recoil, has a mass of order the mass of the hole and an extent of order the hole's radius of influence,

$$r_\bullet = GM_{\rm BH}/\sigma_*^2. \tag{3.2}$$

Throughout their dynamical evolution, these stellar clusters will lose mass by relaxation and expansion, as well as tidal disruptions by the black hole (Komossa & Merritt 2008, O'Leary & Loeb 2012). The relaxation timescale,

$$t_{\rm r} \approx 10^9 \left(\frac{M_\bullet}{10^5 M_\odot}\right)^{5/4} {\rm yr}, \tag{3.3}$$

ranges from several Myr for the smallest IMBHs to a Gyr for the largest. As IMBHs get accreted by the Milky Way early in the history of the Universe, the above processes can cause a 60-80% fractional loss of stellar mass by the present day (O'Leary & Loeb 2012). At the same time, the physical extent of the clusters is expected to grow like $t^{1/3}$ after the first relaxation timescale (O'Leary & Loeb 2012), resulting in a total expansion by a factor of 16 (for $\mathrm{M}_\bullet \sim 10^3 M_\odot$) to 3 (for $\mathrm{M}_\bullet \sim 5 \times 10^4 M_\odot$) over a Hubble time. Assuming that the initial extent of the clusters is dictated by the IMBH's sphere of influence at infall, their physical extent today would range between 0.5pc and 1.0pc. Despite their expansion, stellar clusters surrounding IMBHs would still be very compact today and may appear point-like or extended depending on their distance. Photometrically, they would have colors similar to those of old stars, while spectroscopically they would be distinguishable by the high velocity dispersions.

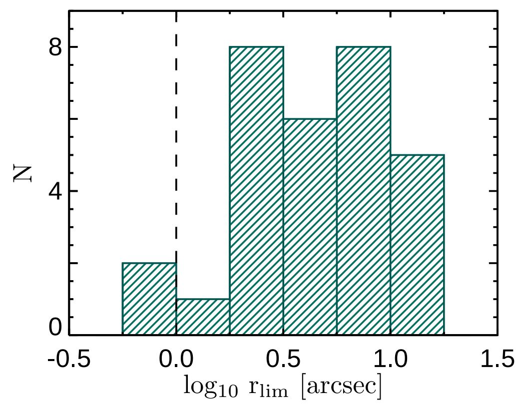

Figure 3.7: Angular size of stellar clusters around Galactic "naked" IMBHs in the "direct collapse" model (see text for details). The angular extent is calculated for an observer at $d_{\rm GC} = 8$ kpc from the center of the VLII halo. *Dashed line:* angular resolution limit of current ground-based surveys.

We have modelled the apparent brightness distribution of stellar cusps around naked IMBHs in the direct collapse scenario, which produces the largest number of massive IMBHs today. We assume an initial stellar mass that is twice the mass of the black hole and a present-day stellar mass-to-light ratio of 4 (as appropriate for an old stellar population with a Salpeter IMF - see Rashkov et al. 2012; for details). The mass density in the star clusters is expected to follow a steep power law with drop-off power $\alpha \sim$ -2.15. Given these physical characteristics, we calculate the peak surface brightness (within a typical SDSS seeing element of angular size $\sim$ 1 arcsec) of the clusters as would be seen by a mock observer located 8 kpc from the center of the VLII main halo. The distribution is shown in Figure 3.6. The angular size out to which the brightness profile will be brighter than 25 mag arcsec^{-2} is shown in Figure 3.7. Most clusters would be resolvable, as their angular extent spans 2 to 10 1-arcsec resolution elements. In these calculations, we have accounted for the fact that the SDSS points away from the Galactic Center by excluding IMBHs within 8 kpc of the VLII halo center. The resulting distribution of peak brightness for the IMBH stellar clusters would have to be further scaled down by a factor of 5, to account for the limited sky coverage of the SDSS. After accounting for these corrections, only a handful of clusters should be detectable with current surveys. This is consistent with a recent search for stellar clusters surrounding recoiled IMBHs in the SDSS source catalog that resulted in an upper limit of 100 candidates in the Milky Way halo (O'Leary & Loeb 2012). We have also estimated the proper motion of IMBHs on the sky. Having tangential velocities ranging from 0 to 250 $\mathrm{km\,s^{-1}}$ as seen from an observer at 8 kpc from the VLII halo center, and distances of up to 100 kpc, their proper motions fall in the range between 0.1 and 10 milliarcsec year^{-1}. This is similar to measured proper motions of distant halo stars and may be currently detectable with the *Hubble Space Telescope* (Sohn et al. 2012), and future missions such as *Gaia*.

Chapter 4

What is the mass of the Milky Way?

4.1 Introduction

The mass of the Milky Way's dark matter halo is a key astrophysical quantity for placing our Galaxy in a cosmological context, modelling the formation of the Local Group, deciphering the structure and dynamics of the luminous Galactic components, and ultimately for understanding the complex processes of baryon dissipation and substructure survival within the cold dark matter (CDM) hierarchy. It is, unfortunately, amongst the most poorly known of all Galactic parameters. A common technique to measure the total mass of the Milky Way is to use kinematic tracers such as globular clusters, distant halo stars and satellite galaxies Wilkinson & Evans (1999), Xue et al. (2008), Gnedin et al. (2010), Deason et al. (2012b), Boylan-Kolchin et al. (2013). In spherical geometry, the Jeans equation provides a link between the host potential of a pressure-supported system and the distribution function of the tracer population in equilibrium with it according to

$$M(<r) = \frac{r\sigma_r^2}{G}\left(-\frac{d\ln\rho_*}{d\ln r} - \frac{d\ln\sigma_r^2}{d\ln r} - 2\beta\right), \qquad (4.1)$$

Table 4.1: Recent mass estimates of the Milky Way

Author	Year	Method used	$M_{\rm MW}$ [$M_\odot$]	Estimate type
Little & Tremaine	1987	Satellites	$1.7 - 3.7 \times 10^{11}$	M(<50kpc)
Zaritsky et al.	1989	Satellites	$11 - 15 \times 10^{11}$	M(<120kpc)
Kulessa & Lynden-Bell	1992	Satellites	13×10^{11}	M(<230kpc)
Kochanek	1996	Satellites, Esc. Speed, Rotation	$3.8 - 6.0 \times 10^{11}$	M(<50kpc)
Wilkinson & Evans	1999	Satellites, GCs	$1.8 - 9 \times 10^{11}$	M(<50kpc)
Wilkinson & Evans	1999	Satellites, GCs	$0.2 - 5.5 \times 10^{12}$	$\rm M_{total}$
Sakamoto et al.	2003	Satellites, GCs, Halo stars	$1.5 - 3.0 \times 10^{12}$	$\rm M_{total}$
Sakamoto et al.	2003	Sat.(excl. Leo I), GCs, Stars	$1.1 - 2.2 \times 10^{12}$	$\rm M_{total}$
Battaglia et al.	2005	Satellites, GCs, Halo stars	$0.6 - 2.0 \times 10^{12}$	$\rm M_{total}$
Dehnen et al.	2006	Satellites, GCs, Halo stars	1.5×10^{12}	$\rm M_{vir}$ (<200kpc)
Smith et al.	2007	High-velocity stars	$0.88 - 2.56 \times 10^{12}$	$\rm M_{vir}$ (<305kpc)
Xue et al.	2008	BHB stars	$3.3 - 4.7 \times 10^{11}$	M(<60kpc)
Watkins et al.	2010	Satellites	$7 - 34 \times 10^{11}$	M(<300kpc)
Deason et al.	2012b	Satellites, GCs, Halo stars	$5 - 10 \times 10^{11}$	M(<150kpc)

Note. — Columns 1 and 2 indicate the authors and year of publication, columns 3, 4, and 5 give the method of mass measurement used, the mass estimate, and the mass type.

where $M(< r)$ is the total gravitating mass, ρ_* is the density profile of the tracer stars, σ_r is their radial velocity dispersion, and β is the velocity anisotropy. The uncertainties in the mass estimates for the Milky Way are due to the fact that, even with high-quality data (accurate distances and radial velocities), the orbit eccentricities and the density profile of the tracer population are poorly constrained. Without firm knowledge of the tracer properties, Galactic mass measures suffer from the well-known mass-anisotropy-density degeneracy.

MW mass estimates typically range between $5 \times 10^{11} M_\odot$ and $2 \times 10^{12} M_\odot$ and are measured in a diverse set of ways, including rotation curve of halo gas, local escape speed, and kinematics of discrete halo tracers, like globular clusters, satellite galaxies and halo stars. We list a compilation of commonly cited MW mass estimates in Table 4.1.

In this chapter, we use state-of-the-art tracer kinematic data from Deason et al. (2012b) and two high-resolution simulations of MW-analog galaxies, *Eris* and *VLII*, to try to weigh the MW halo. The two galaxies have total virial masses at the two ends of the spectrum of quoted mass estimates, $7 \times 10^{11} M_\odot$ and $2 \times 10^{12} M_\odot$ respectively, so that allows us to fully explore the extremes of possible values found in the literature. We first apply a simple tracer mass estimator, derived by Watkins et al. (2010) under the assumptions of spherical symmetry and scale-free halo structure to the two simulations. Thus, we measure its performance in the case of realistic data, in which none of the above assumptions hold. We then compare the stellar halos in the two simulations in detail to the best data available for the MW halo, specifically focusing on their stellar tracer density profiles, tracer kinematic anisotropy profiles and their velocity dispersion profiles. Finally, we interpret our results by direct numerical integration of the Jeans equation, which allows us to disentangle the complex interplay between the different parameters.

This chapter is organized as follows: in § 4.2, we briefly describe the kinematic tracers we use in our study; in § 4.3, we describe the Eris simulation, a novel hydrodynamic cosmological simulation of a late-type MW-like galaxy. In § 4.4, we outline the tracer mass estimator and its performance on the VLII and Eris data, and study the simulated stellar halos in detail. In § 4.5, we compare the direct observable, the velocity dispersion profile, with ones we measure in the simulations and interpret our results with controlled experiments based on integration of the Jeans equation. We conclude in § 4.6.

4.2 Halo Tracer Population

To derive precision constraints on the mass of the Milky Way's dark matter halo, we use the samples of blue horizontal branch (BHB) stars specifically targeted by SDSS and SEGUE for spectroscopy. BHB stars are excellent tracers of Galactic halo dynamics because because they are luminous and have a nearly constant absolute magnitude within a restricted color range.

Xue et al. (2008) select their star sample using photometric and spectroscopic data from SDSS DR6. Their selection combines a photometric color cut based on analysis by Yanny et al. (2000) and two spectroscopic Balmer line cuts meant to remove contaminating blue straggler

(BS) and warm main-sequence stars. The final sample consists of 2,558 stars with galactocentric distance to about 60kpc (Xue et al. 2008).

Instead, Deason et al. (2012b) aim to find more distant stars, with $D > 80kpc$. They first implement a photometric color selected to select objects consistent with faint stars, with $20 < g < 22$. They then follow up their candidates with the VLT-FORS2 spectrograph to obtain low resolution spectra of these objects. Finally, based on their Balmer spectral lines, they identify 7 BHB stars and 31 BS stars. Their sample reaches galactocentric distances of 150kpc and is the largest catalog to date to do so (Deason et al. 2012b).

In their analysis, Deason et al. (2012b) complement their BS and BHB samples with a sample of previously published N-type carbon (CN) stars from Totten & Irwin (1998), Totten et al. (2000), Mauron et al. (2005), Mauron (2008); two additional BHB stars from Clewley et al. (2005) as well as globular clusters and MW satellites excluding Leo I. For the remainder of this chapter, we adopt the binning of all these data exactly as published in Figure 9 of Deason et al. (2012b).

4.3 The Eris Simulation

The cosmological simulation employed in the present study is "Eris", one of the highest resolution "zoom-in" simulations ever run of the formation of a Milky Way-sized disk galaxy from cosmological initial conditions. Details of the simulation are given in Guedes et al. (2011) and are quickly summarized here for completeness. Eris follows the formation of a $M_{\rm vir} = 7.9 \times 10^{11}\,{\rm M}_{\odot}$ galaxy halo from $z = 90$ to the present epoch using the N-body + smoothed particles hydrodynamics (SPH) code `GASOLINE` (Wadsley et al. 2004). The simulation includes Compton cooling, atomic cooling, metallicity-dependent radiative cooling at low temperatures, a prescription for blastwave supernova feedback, and the ionizing effect of a uniform UV background using a modified version of the Haardt & Madau (1996) spectrum. The target halo was selected to have a quiet merger history with no major mergers (defined as mass ratio $\geq 1/10$) at redshift $z < 3$ (four minor mergers occur at $z \simeq 3$, and two more at $z \simeq 1$ and $z \simeq 0.6$). The high resolution region was resampled with 13 million dark matter particles and an equal number of gas particles, for a mass resolution of $m_{\rm DM} = 9.8 \times 10^4$ M$_\odot$ and $m_{\rm SPH} = 2 \times 10^4$ M$_\odot$. The gravitational softening length was fixed to 120 physical pc for all particle species from $z = 9$ to the present time, and evolved as $1/(1 + z)$ at earlier times. Star particles form in cold gas that reaches a density threshold of $n_{\rm SF} = 5$ atoms cm^{-3}, and are created stochastically with an initial mass $m_* = 6 \times 10^3$ M$_\odot$ distributed following a Kroupa et al. (1993) initial mass function. Supernova explosions deposit an energy of 8×10^{50} ergs and metals into a 'blastwave radius', and the heated gas has its cooling shut off following Stinson et al. (2006). The use of a high threshold for star formation has the effect of increasing the efficiency of supernovae feedback through the injection of energy in localized high-density regions.

At $z = 0$, Eris is a late-type spiral galaxy of virial radius $R_{\rm vir} = 239$ kpc and total stellar mass $M_* = 3.9 \times 10^{11}$ M$_\odot$, and is resolved with $N_{\rm DM} = 7 \times 10^6$, $N_{\rm gas} = 3 \times 10^6$, $N_* = 8.6 \times 10^6$ dark matter, gas, and star particles, respectively. Its rotation curve has a value at 8 kpc (the solar circle) of $V_{c,\odot} = 206$ km s^{-1}, in good agreement with the recent determination of the local circular velocity, $V_{c,\odot} = 218 \pm 6$ km s^{-1}, by Bovy et al. (2012). Mock $i-$band images show that Eris has an i-band absolute magnitude of $M_i = -21.7$, an extended stellar disk of exponential scale length $R_d = 2.5$ kpc, a pseudobulge with Sérsic index $n = 1.4$, and a bulge-to-disk ratio B/D=0.35 (Guedes et al. 2011). The present-day $u - r = 1.52$ mag color of Eris is consistent with the colors of galaxies that host pseudobulges (Guedes et al. 2012). Eris's surface brightness profile shows a downbending break at about five disk scale lengths, as observed in many nearby spiral galaxies (Pohlen & Trujillo 2006). Eris falls on the Tully-Fisher relation, on the locus of the $\Sigma_{\rm SFR}$-$\Sigma_{\rm HI}$ plane occupied by nearby spiral galaxies, and on the stellar mass-halo mass relation at $z = 0$. The predicted correlations of stellar age with spatial and kinematic structure are in good qualitative agreement with the correlations observed for mono-abundance stellar populations in the Milky Way (Bird et al. 2013).

Figure 4.1 shows Eris' stellar halo as viewed by an external observer. A region of size 300kpc centered on the galactic disk is shown. Three prominent satellites are visible in the image, together with a variety of other substructure, including streams and shells. For comparison, we show a 400kpc region centered on the accreted stellar halo in VLII in the same plot.

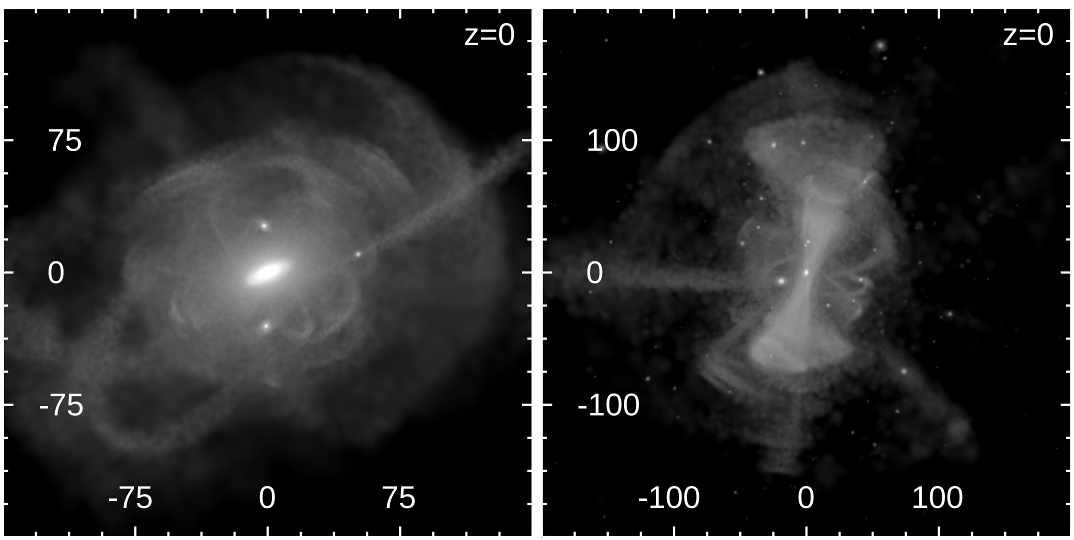

Figure 4.1: Image of Eris' and VLII's stellar halos, as seen from an external observer. A 300kpc (Eris, left panel) and a 400kpc (VLII, right panel) regions centered on the center of each galaxy are shown. The surface density shown ranges from 10^2 to 10^8 $M_{\odot}/kpc^2$. Both halos display rich structure, consisting of streams and shells, remnants of past accretion events. The galactic disk and three prominent satellites are clearly visible in the Eris image. In stark contrast to the Eris halo, VLII displays a prominent "hourglass-shaped" feature.

4.4 Tracer Mass Estimator

4.4.1 The Jeans equation - interface between kinematic tracers and galactic potentials

The Jeans equation is a popular tool for estimating the masses of galaxies. The first moment over velocity of the collisionless Boltzmann equation, it links the overall system potential to the kinematics of discrete tracers moving in equilibrium with it. In radial symmetry, the Jeans equation reads:

$$\frac{1}{\rho}\frac{\rho\sigma_r^2}{dr} + \frac{2\beta\sigma_r^2}{r} = -\frac{GM(r)}{r^2} \tag{4.2}$$

where r is the radial coordinate, ρ is the tracer density, σ_r is the radial velocity dispersion of the tracers, $\beta = 1 - \sigma_t/2\sigma_r$ is the anisotropy between the tangential and radial components of the tracer velocity dispersion, and $M(r)$ is the mass of the system within r.

While this version of the equation in spherical symmetry is able to capture the interplay between the underlying mass potential, kinematic tracer distribution and velocity anisotropy of a galactic halo in their most general form, making certain assumptions about the functional form of the individual components can greatly simplify the solution to the Jeans equation. For example, assuming a constant velocity anisotropy β throughout the tracer sample results in the following solution for the radial velocity dispersion profile:

$$v_r^2(r) = \frac{1}{r^{2\beta}\rho(r)}\int_r^\infty dr' r'^{2\beta}\rho(r')\frac{d\Phi}{dr'} \tag{4.3}$$

This simple way to obtain a solution is very useful, as it can directly be compared to the observable line-of-sight velocity dispersion σ_{los}. While at small galactocentric distances the geometric error incurred from Earth's offset from the galactic center is large, this error falls to

9% at $r = 20kpc$ and only 3% at $r = 30kpc$, so for tracers in the outer halo of the Galaxy, the two can be compared directly without corrections. Since most constraints on the total mass of the MW depend on velocity measurements of the outer halo, where σ_r and σ_{los} agree well, this form of the Jeans equation becomes a useful tool to constrain the mass of our galaxy.

A further simplification results from making some assumptions about the form of the underlying matter potential and the distribution of the tracers within that potential. Watkins et al. (2010) derive a family of mass estimators that provide an estimate of the total mass enclosed within radius r_{out}, the radial distance to the most distance tracer. These estimators assume a scale-free density profile for the tracer population and a scale-free underlying potential. In particular, if the tracer number density is described as:

$$\rho(r) \propto r^{-\gamma} \text{ or } \frac{\mathrm{d} \log \rho}{\mathrm{d} \log r} = -\gamma \tag{4.4}$$

and the mass distribution is described as:

$$\frac{M(r)}{M(a)} = \left(\frac{r}{a}\right)^{1-\alpha} \tag{4.5}$$

for some radial distance $r = a$, then the total mass enclosed within the furthest observed tracer is (Watkins et al. 2010):

$$M = \frac{(\alpha + \gamma - 2\beta) r_{out}^{1-\alpha}}{G} \left\langle v_r^2 r^\alpha \right\rangle \tag{4.6}$$

The above mass estimator has been successfully tested to be unbiased in the regime in which the assumptions under which it was derived hold. Furthermore, it has been been used by Watkins et al. (2010) and Deason et al. (2012b) to estimate the mass of the MW. However, galaxies (including the MW) have complex structures and are generally not well represented by scale-free potentials, which introduces an additional uncertainty in the mass estimates derived by the two groups. That is why it is useful to test the performance of the Watkins et al. (2010) mass estimator with simulations, in which the value of the total halo mass is known at every radius.

4.4.2 Applications of the Jeans equation to simulated galaxies

We now apply the Watkins et al. (2010) mass estimator to the two available simulated galaxies - Eris and VLII. We begin by randomly selecting 500 orientations of the region observed by SDSS in both simulations. This is important to do, as observations of stars in the outer MW halo, which are essential in constraining the Galaxy's mass, typically originate from the region surveyed by the SDSS. Limiting the tracer data to 1/5 of its full range could bias any individual estimate and randomizing the survey pointing within each simulation box will give the full scatter in the measurement. In VLII, the lack of disk allows for the complete freedom in choosing the SDSS footprint. In Eris, there is a disk, so we have a plane in which to place the 500 theoretical observers if we want to stay true to the geometrical uncertainties introduced by the disk plane. However, we could also choose to disregard the disk orientation and, like in the VLII case, explore the full topology of the stellar halo.

In each of these 500 realizations of SDSS within each simulation, we then measure the average anisotropy β, the average tracer profile slope γ and the average underlying mass density profile α in a radial region enclosed between an inner boundary of 20kpc and an outer boundary $r_{\rm out}$ that is allowed to vary between 25kpc and 200kpc. The mass estimate $M_{\rm est}(< r_{\rm out})$ that is calculated via Equation 4.6 can be directly compared to the true mass $M_{\rm true}(< r_{\rm out})$ enclosed within the same radius. We show the performance of the estimator in Figure 4.2, in which we plot the ratio of the estimated to the true mass as a function of radius r_{out} to which the two were measured. The resulting heatmap shows the density of observations in the 500 realizations

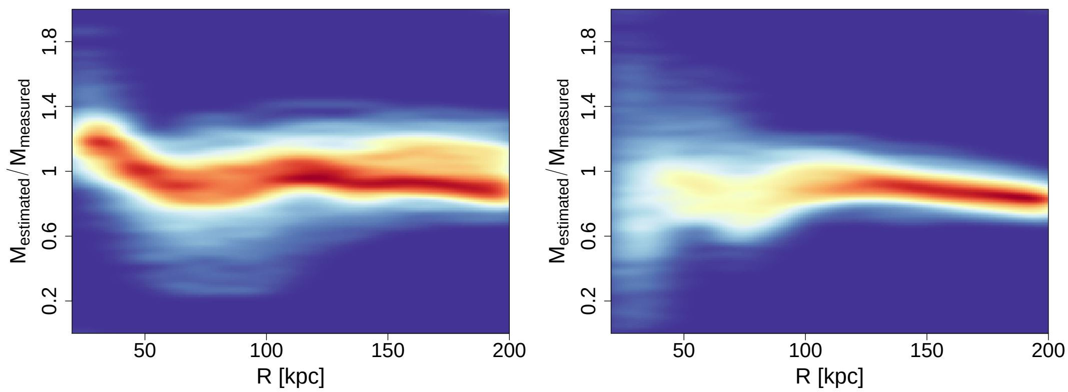

Figure 4.2: Peformance of the Watkins et al. (2010) mass estimator as a function of radius. *Left panel:* Eris. *Right panel:* Via Lactea II. What is shown is the ratio of the mass estimate obtained with Equation 4.6 divided by the true mass of the simulated galaxy within the same radius. The colors correspond to the density of individual points obtained from 500 individual SDSS-like footprint pointings within the simulation box, each of which was probed at 40 radial distances.

of SDSS in the $M_{\rm est}/M_{\rm true}$ - $r_{\rm out}$ plane.

It is clear from the figure that the estimator is not able to provide perfect measurements of the total mass enclosed within the outermost tracer, but in most cases gives solutions within 20 to 40% of the true value. This is encouraging, however, given the stringent simplifying assumptions (spherical symmetry, scale-free radial behavior) that go into its derivation. The masses of the MW derived using Equation 4.6 and quoted by both Watkins et al. (2010) and Deason et al. (2012b) are thus very likely to be within 20 - 40% of the true value of the MW mass, still intriguingly small compared to previous estimates.

4.4.3 Parameter uncertainties - the velocity anisotropy

Some of the main remaining challenges in using observations of stellar kinematics to measure the MW mass revolve around the value of the anisotropy parameter β. Intrinsically hard to measure, β requires knowledge of tangential as well as radial motions of the tracers (for large enough galactocentric distance, line-of-sight velocities suffice, as they are essentially in the

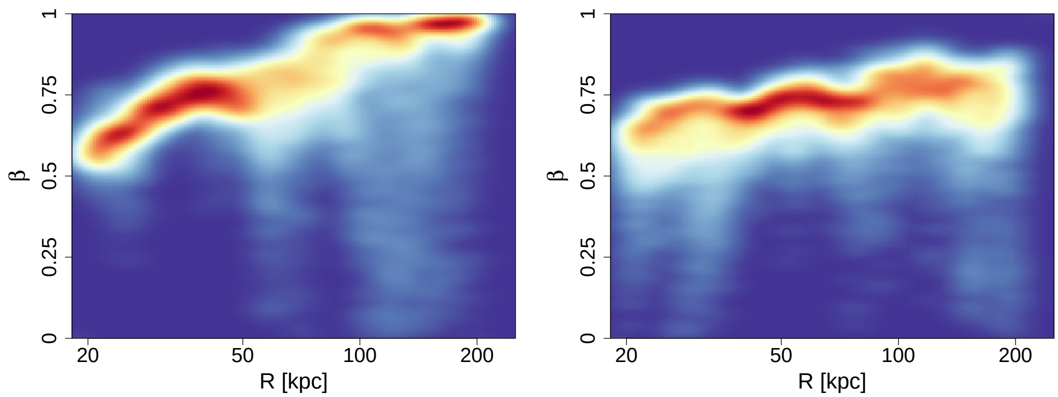

Figure 4.3: Velocity anisotropy as a function of radius. *Left panel:* Eris. *Right panel:* Via Lactea II. Heatmaps are based on 500 realizations of a SDSS-like survey within each simulation box, allowing for for full freedom in orientation - i.e. regardless of disk position in the case of Eris. Both agree with observations very well in the inner halo regions - out to 50kpc. Eris' tracers display purely radial kinematic behavior in the outer halo, i.e. close to its virial edge.

radial direction). In models, the anisotropy parameter is often degenerate with the total mass of the system, and has only recently been measured by Deason et al. (2012a) to approximately equal 0.5 in in the MW, i.e. it is radially biased out to about 50kpc of the Galactic center.

The β anisotropy is easy to measure in simulations and we show it as a function of galactocentric radius in Figure 4.3. Like in Figure 4.2, the heatmap color contours are a result of 500 random SDSS realizations within the simulation box of Eris and VLII. Out to about 50kpc, both simulations agree very well with the MW - with values of β about 0.6 - 0.75, they are clearly radially biased. In the case of Eris, however, the anisotropy then quickly asymptotes to 1, indicative of purely radial kinematics near the virial edge of the galaxy, at $R_{\rm vir} = 238kpc$. VLII has a larger virial radius and the anisotropy does not reach this purely radial regime in the 200kpc window we probed. Observing a similar behavior in the β profile in the future would be indicative of probing all the way out to the MW galactic edge. This would provide a strong constraint of the total mass of the Galaxy.

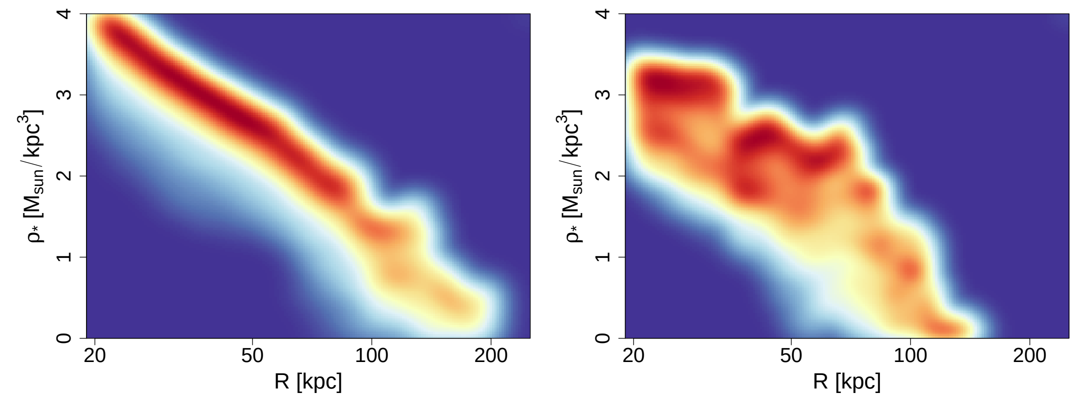

Figure 4.4: Stellar density profiles as a function of galactocentric radius. Heatmaps are based in 500 realizations of a mock SDSS survey within each of the two simulation boxes, allowing full freedom in orientation - i.e. regardless of disk position in the case of Eris. In both cases, we only consider tracers with R > 20kpc to avoid contamination from the disk and bulge in the case of Eris. *Left panel:* Eris. We measure a profile slope of -3.4 within 60kpc and -4.4 outside that region. *Right panel:* Via Lactea II. We measure profile slopes of -2.8 and -4.6 inside and outside 50kpc respectively.

4.4.4 Parameter uncertainties - the stellar density profile

Another source of uncertainty in using the Jeans equation as a mass estimator is the tracer density profile. This would be either the mass density or the number density profile of the stellar halo. Previous attempts to measure it from the data include ones by Bell et al. (2008), who measure a power law slope in the range from -2 to -4, and Deason et al. (2011), who measure a halo slope of -2.3 inner of 27kpc and -4.6 outside that radius. This quantity is very sensitive to the accretion history of a particular galaxy; however, it is important to verify that the simulated halos we use in this analysis have a reasonable tracer distribution when compared to the observed one in the MW.

We plot heatmaps of the corresponding stellar halo density profiles as measured from 500 random SDSS orientations within the Eris and VLII simulation boxes in Figure 4.4. Note that the VLII stellar halo exhibits a large range in the normalization of its density profile. This effect can be attributed to the "hourglass" shape of its most prominent accretion event. Looking down the principal axis of the debris from this particular accreted substructure will result in a higher measured density than looking 90° away from the principal axis.

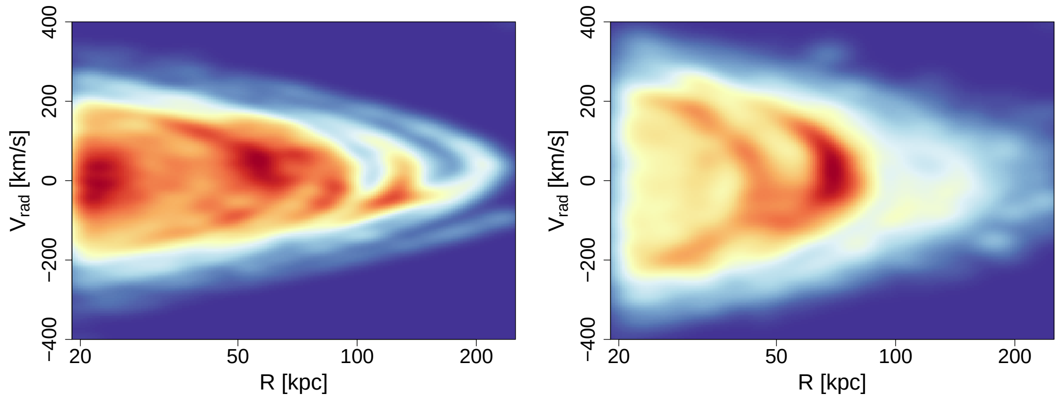

Figure 4.5: Phase space density of stellar tracers in the v_r - R plane. Overdensities in these plots correspond to accretion events whose stellar orbits have apocenters at particular galactocentric distances. They result in knees in the stellar density profiles and dips in the velocity anisotropy profiles. Note the broader range of radial velocities in VLII compared to Eris, which we attribute its larger mass. *Left panel:* Eris. A clear overdensity of stars occurs around 60kpc. *Right panel:* Via Lactea II. There are two apocenter-like arc features - at 40kpc and 70kpc.

In order to quantify the falloff of the tracer density, we break the stellar profiles in the two simulations in two general regions: inner (between 20kpc and 50kpc of the box center), and outer (outside of 50kpc from the center). In Eris, we measure an inner slope of -3.4 and an outer slope of -4.4 if we average over all angular directions. In VLII, we measure an inner slope of -2.8 and an outer slope of -4.6 similarly averaging over the entire sky. These values depend on the detailed structure and accretion history of each individual halo, but it is very encouraging that they fall in the ballpark of measured values in MW, which makes our observational comparison through kinematic tracers easier to interpret.

For further detail in the shapes of these profiles and the features in the velocity anisotropy profiles from Figure 4.3, we look at the distribution of tracer stars in v_r - R phase space. We show the corresponding heatmaps in Figure 4.5. Overdensities of stars in this phase space plane will be indicative of the apocenter distances of orbits associated with particular accretion events. Since stars spend most of their time at apocenter, we expect to see tracers from prominent progenitors cluster in certain regions of the v_r - R plane. These regions are typically linked to features in the smooth density profile, such as knees where the slope changes. A closer look at Figure 4.5 reveals such overdensities at roughly 60kpc in Eris and 40kpc and 70kpc in VLII. Changes in the behavior of the stellar density profiles at the same locations in the two simulations can then be explained as a direct consequence of the stellar halos' structures.

Additionally, one could expect that overdensities at the apocenters of stellar orbits lower the anisotropy parameter β at the same galacocentric radii. The reason for this is as simple as follows - at apocenter, a given star has reached the furthest radial point in its orbit and is turning around to fall back toward the center of the potential. That means that at apocenter exactly, its radial velocity component is negligible, $v_r = 0$. As β quantifies the ratio of the radial and tangential components of the tracer motion, it is expected that it will drop in regions where there is an overdensity of stars at apocenter. We observe these characteristic dips in β at the exact same locations in R (60kpc for Eris, and 40 and 70kpc for VLII) in Figure 4.3.

4.5 The Mass of the Milky Way's Halo

4.5.1 Direct comparison with observable data

In the previous sections, we looked at the structural properties of the stellar halos in the simulations that are subject of this study, including their density profiles as a function of galactocentric radius, their velocity anisotropy and their phase space density in the v_r - R plane. We linked certain features in the anisotropy and density profiles to regions in phase space where stars cluster due to the apocenter locations of orbits associated with particular accretion events. We verified that the properties of the simulated stellar halos are very similar to recent state-of-the-art observations of the MW halo, such as the value of the anisotropy, the existence of a knee in the density profile, and the range of values of the inner and outer slope of the density profile.

Additionally, we verified that a simple mass estimator based on the Jeans equation under assumptions of spherical symmetry and scale-free behavior is able to reproduce the correct value of the enclosed mass to within 20 - 40 % despite the fact that these conditions do not hold true in the case of realistic accreted stellar halos. It was precisely this mass estimator that was used in combination with observations of the line-of-sight velocity dispersion profile to determine that the mass of the MW galaxy is likely smaller than was previously thought (Watkins et al. 2010, Deason et al. 2012b). Given the similarities between the simulated and the observed stellar halos, it is worthwhile to understand if the mass of the MW can be estimated directly from the two simulations without resorting to the assumptions of the Jeans mass estimator.

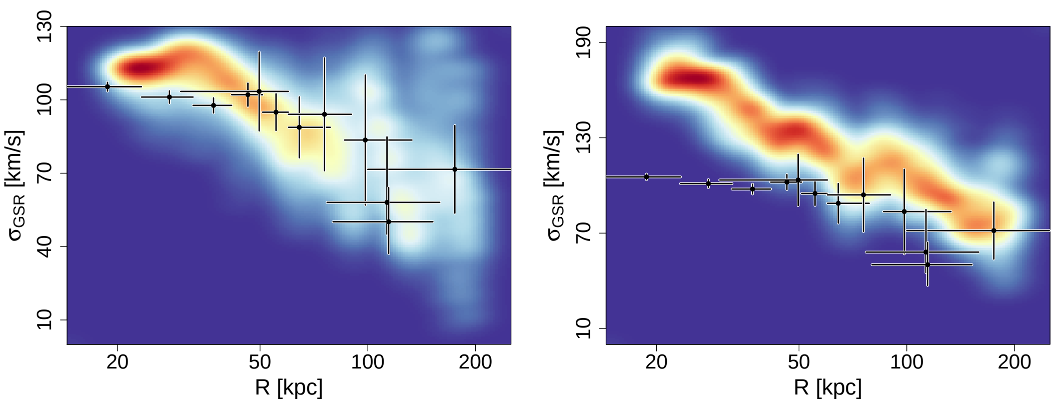

Figure 4.6: Radial velocity dispersion heatmaps from 500 random SDSS realizations per simulation box compared to data from Deason et al. (2012b). Data points technically represent line-of-sight velocity dispersion σ_{los} instead of σ_r. However, the geometric error in using one and not the other is less than 9% beyond 20kpc and less than 4% beyond 30kpc. Eris, a much lighter galaxy than VLII, is able to fit the data much better. Note the difference in y-axis scale between the two panels. *Left panel:* Eris. *Right panel:* Via Lactea II.

In Figure 4.6, we plot the line-of-sight velocity dispersion σ_{los} data from Deason et al. (2012b) and Xue et al. (2008) together with heatmaps of the radial velocity dispersion σ_r as measured in 500 random projections of the SDSS survey within the simulation boxes of Eris and VLII. While the two quantities compared are not exactly the same, the geometric error made in using σ_r instead of σ_{los} is only 9% at 20kpc and drops to less than 4% at 30kpc and beyond, which do not significantly affect the comparison presented here. It is clear from this figure that Eris, with a dark halo of total mass $8 \times 10^{11} M_{\odot}$, fits the data much better than VLII, with its much more massive halo of mass $2 \times 10^{12} M_{\odot}$. The simulations therefore confirm results from Watkins et al. (2010) and Deason et al. (2012b) that the MW could be less massive than $1 \times 10^{12} M_{\odot}$ with measurements coming from realistic stellar halos simulated in the full cosmological accretion setting and without relying on assumptions of spherical geometry and scale-free behavior.

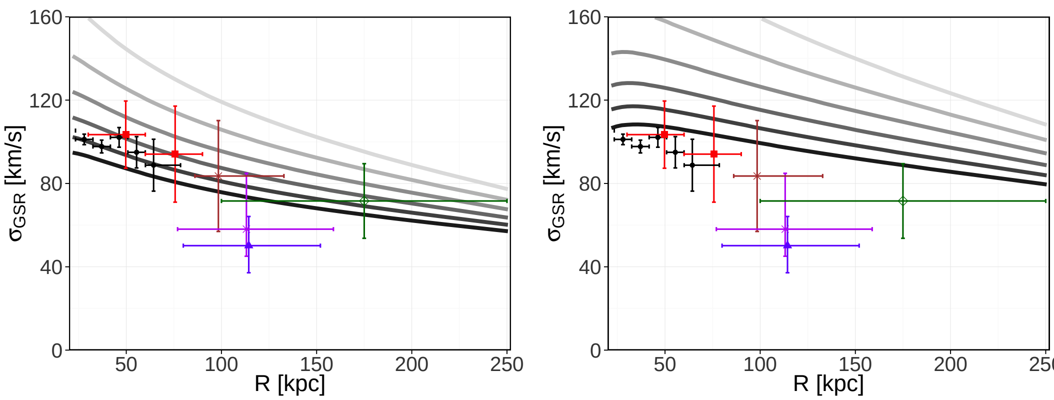

Figure 4.7: Radial velocity dispersion profiles from numerical integration of the Jeans equation compared to data from Deason et al. (2012b). Data points technically represent line-of-sight velocity dispersion σ_{los} instead of σ_r. However, the geometric error in using one and not the other is less than 9% beyond 20kpc and less than 4% beyond 30kpc. Eris, a much lighter galaxy than VLII, is able to fit the data much better. All integrated σ_r profiles have $\beta = 0.55$. The tracer density profiles explored have slopes γ ranging from -2. (lightest gray) to -4.5 (darkest gray) *Left panel:* A DM halo similar to the one of Eris. *Right panel:* A DM halo similar to the one of Via Lactea II.

4.5.2 Understanding the line-of-sight velocity dispersion profile

Attributing the discrepancy between the σ_{los} data points and the VLII σ_r profiles in the bottom panel of Figure 4.6 requires verifying that no additional factors play a role in setting that galaxy's halo structure. While we verified that the kinematic anisotropy and stellar tracer density profiles resemble the ones measured in the MW, VLII is a dark matter-only simulation which does not capture the influence of a galactic disk in the central regions of its halo. Running a fully-hydrodynamic VLII twin simulation that self-consistently forms a late-type disk galaxy is resource-intensive and beyond the scope of this work. However, performing a series of controlled experiments numerically integrating the Jeans equation in full generality of the underlying mass distribution will be sufficient to answer the questions about the disk's role in contracting the DM halo and affecting the σ_r stellar profile.

In Figure 4.7, we plot the σ_{los} data from Deason et al. (2012b) and Xue et al. (2008) as a function of radius together with σ_r profiles calculated by numerical integration of the Jeans equation. In all cases, we use an anisotropy $\beta = 0.55$, similar to the value measured in the MW and values from Eris and VLII. Due to the uncertainty in the tracer density profile, we try 5 different values from $\gamma = 2$ (shown in lightest gray) to $\gamma = 4.5$ (in darkest gray) in steps of 0.5. A DM halo similar to the one in the Eris simulation is able to fit the data for a wide variety of values for the tracer density profile slope, while a DM halo similar to the VLII one can only barely fit the data for an extreme value of $\gamma = 4.5$. However, VLII was a dark-matter only collisionless simulation in which no baryonic disk forms in the halo center. Eris, on the other hand, self-consistently forms a late-type spiral stellar disk which in turn contracts the DM halo. The measured halo concentration in Eris is $c = R_s/R_{vir} = 22$ (Guedes et al. 2011), much higher than a typical value of 10 or 11, like those of DM-only simulated halos. In order to make the comparison with VLII more realistic, we should consider a massive halo which would be as concentrated as the Eris halo in the hypothetical presence of a baryonic disk in its inner regions.

In Figure 4.8, we explore the possible contraction of the inner regions of the VLII DM halo in the presence of a hypothetical baryonic disk. We achieve this effect by modifying the scale radius R_s to the best fitting NFW profile of VLII, so that the halo concentration matches the one observed in Eris, $c = 22$. In doing so, we adjust the profile's normalization to keep the

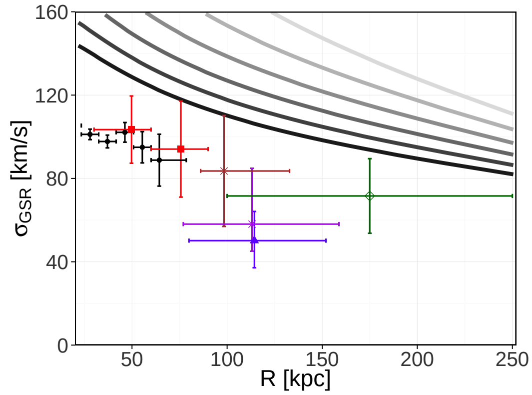

Figure 4.8: Effect of the halo contractin on the radial velocity dispersion profiles. Data points from Deason et al. (2012b) technically represent line-of-sight velocity dispersion σ_{los} instead of σ_r. However, the geometric error in using one and not the other is less than 9% beyond 20kpc and less than 4% beyond 30kpc. All integrated σ_r profiles have $\beta = 0.55$. The tracer density profiles explored have slopes γ ranging from -2. (lightest gray) to -4.5 (darkest gray). The underlying matter potential mimics a DM halo with mass similar to the one of Via Lactea II, but concentration as high as the one of the Eris halo, $c \sim 22$. None of the numerically integrated profiles is a good fit to the data, suggesting VLII's mass is too high to fit the data.

total enclosed mass equal to the one in the un-contracted case. The five different σ_r profiles correspond to five different values of the tracer density slope, just like in Figure 4.7. This time, however, none of the profiles match the observed data. This suggests that, even if VLII had a baryonic disk in its center, the predicted kinematic profiles would be a poorer representation of the observed data. VLII is simply too massive to support radial velocity dispersions as low as 50km/s at a distance of 100kpc.

4.6 Summary

We have used the state-of-the-art high resolution numerical simulations *Eris* and *VLII* to weigh the MW halo using halo stars as kinematic tracers. The advantage of using computer simulations is that the velocity anisotropy, a parameter poorly constrained in reality, can be readily measured in the simulations.

We apply a tracer mass estimator derived by Watkins et al. (2010) in the case of spherical symmetry and scale-free, power-law halo structure to the simulated stellar kinematic data. We determine that the estimator, which has most recently used to estimate a MW mass by Deason et al. (2012b), is able to estimate the true MW halo mass within 20 - 40% despite the fact that none of the assumptions it is based on hold in reality.

In an attempt to make the comparison between simulations and observations more direct, we distance ourselves from the mass estimator, instead directly comparing the observable quantity, the line-of-sight (radial) velocity dispersion profile. We find that Eris has a radial velocity dispersion profile that is a great fit to the observed MW data, while VLII does not. In VLII, the predicted velocity dispersion is too high to accommodate the values measured in the MW by Deason et al. (2012b). This result agrees strikingly well with a recent mass estimate by Bovy et al. (2012), who quote a virial mass of only $8 \times 10^{11} M_{\odot}$ for the MW.

We verify that the Eris and VLII stellar halos look like the Galactic one in every other way, in order to make our result more meaningful. Halos that are as close to the data as possible except for their mass would strengthen our argument that the MW is lighter than previously thought. We compare the halos' velocity anisotropy profiles, both of which agree with the 0.5 recent estimate by Deason et al. (2012a), and their density profiles. The density profile slopes we measure in VLII and Eris are both consistent with estimates from Bell et al. (2008) and Deason et al. (2012a) and vary between -2 and -4. We are able to attribute features in the stellar density profiles and velocity anisotropy profiles to stellar overdensities in the $v_r - R$ phase space diagram. These correspond to the apocenters of orbits from recent accretion events, where stars spend a significant amount of their orbital time, producing a knee in the density profile and lowering the measured velocity anistropy, as they have no radial component velocity component at apocenter.

In order to understand in detail if the line-of-sight velocity dispersion is sufficient indicator that the MW has mass similar to the one of the Eris simulation instead of VLII, we compute the radial velocity dispersion profiles by numerically integrating the Jeans equation. We use two fiducial NFW halos, one resembling Eris and one resembling VLII, with a variety of unknown slopes for the stellar density profile within its observation-permissible range. We note that the lighter halo is able to fit the observed radial velocity dispersion profile for a wider range of the density slope parameter. Additionally, if we introduce a modification to the more massive halo DM structure, such as a higher concentration - possible result of contraction in the presence of a baryonic stellar disk - we observe the more realistic massive galaxy gives an even poorer fit to the data.

We conclude that our results support a growing body of evidence that the MW halo is indeed lighter than previously thought and is consistent with having a virial mass of the order of only $8 \times 10^{11} M_{\odot}$.

Bibliography

Adén, D., Wilkinson, M. I., Read, J. I., Feltzing, S., Koch, A., Gilmore, G. F., Grebel, E. K., & Lundström, I. 2009, *ApJ*, **706**, L150

Baker, J. G., Boggs, W. D., Centrella, J., Kelly, B. J., McWilliams, S. T., Miller, M. C., & van Meter, J. R. 2008, *ApJ*, **682**, L29

Barth, A. J., Greene, J. E., & Ho, L. C. 2005, *ApJ*, **619**, L151

Battaglia, G., Helmi, A., Morrison, H., Harding, P., Olszewski, E. W., Mateo, M., Freeman, K. C., Norris, J., & Shectman, S. A. 2005, *MNRAS*, **364**, 433

Begelman, M. C., Volonteri, M., & Rees, M. J. 2006, *MNRAS*, **370**, 289

Behroozi, P. S., Conroy, C., & Wechsler, R. H. 2010, *ApJ*, **717**, 379

Bell, E. F., Zucker, D. B., Belokurov, V., Sharma, S., Johnston, K. V., Bullock, J. S., Hogg, D. W., Jahnke, K., de Jong, J. T. A., Beers, T. C., Evans, N. W., Grebel, E. K., Ivezić, Ž., Koposov, S. E., Rix, H.-W., Schneider, D. P., Steinmetz, M., & Zolotov, A. 2008, *ApJ*, **680**, 295

Bellovary, J., Volonteri, M., Governato, F., Shen, S., Quinn, T., & Wadsley, J. 2011, *ApJ*, **742**, 13

Belokurov, V., Walker, M. G., Evans, N. W., Gilmore, G., Irwin, M. J., Just, D., Koposov, S., Mateo, M., Olszewski, E., Watkins, L., & Wyrzykowski, L. 2010, *ApJ*, **712**, L103

Belokurov, V., Zucker, D. B., Evans, N. W., Gilmore, G., Vidrih, S., Bramich, D. M., Newberg, H. J., Wyse, R. F. G., Irwin, M. J., Fellhauer, M., Hewett, P. C., Walton, N. A., Wilkinson, M. I., Cole, N., Yanny, B., Rockosi, C. M., Beers, T. C., Bell, E. F., Brinkmann, J., Ivezić, Ž., & Lupton, R. 2006, *ApJ*, **642**, L137

Belokurov, V., Zucker, D. B., Evans, N. W., Kleyna, J. T., Koposov, S., Hodgkin, S. T., Irwin, M. J., Gilmore, G., Wilkinson, M. I., Fellhauer, M., Bramich, D. M., Hewett, P. C., Vidrih, S., De Jong, J. T. A., Smith, J. A., Rix, H.-W., Bell, E. F., Wyse, R. F. G., Newberg, H. J., Mayeur, P. A., Yanny, B., Rockosi, C. M., Gnedin, O. Y., Schneider, D. P., Beers, T. C., Barentine, J. C., Brewington, H., Brinkmann, J., Harvanek, M., Kleinman, S. J., Krzesinski, J., Long, D., Nitta, A., & Snedden, S. A. 2007, *ApJ*, **654**, 897

Benson, A. J., Frenk, C. S., Lacey, C. G., Baugh, C. M., & Cole, S. 2002, *MNRAS*, **333**, 177

Bertschinger, E. 2001, *ApJS*, **137**, 1

Besla, G., Kallivayalil, N., Hernquist, L., Robertson, B., Cox, T. J., van der Marel, R. P., & Alcock, C. 2007, *ApJ*, **668**, 949

Binney, J. & Tremaine, S. 2008, *Galactic Dynamics: Second Edition*, Princeton University Press

Bird, J. C., Kazantzidis, S., Weinberg, D. H., Guedes, J., Callegari, S., Mayer, L., & Madau, P. 2013, *ArXiv e-prints*

Blumenthal, G. R., Faber, S. M., Primack, J. R., & Rees, M. J. 1984, *Nature*, **311**, 517

Bovy, J., Allende Prieto, C., Beers, T. C., Bizyaev, D., da Costa, L. N., Cunha, K., Ebelke, G. L., Eisenstein, D. J., Frinchaboy, P. M., García Pérez, A. E., Girardi, L., Hearty, F. R., Hogg, D. W., Holtzman, J., Maia, M. A. G., Majewski, S. R., Malanushenko, E., Malanushenko, V., Mészáros, S., Nidever, D. L., O'Connell, R. W., O'Donnell, C., Oravetz, A., Pan, K., Rocha-Pinto, H. J., Schiavon, R. P., Schneider, D. P., Schultheis, M., Skrutskie, M., Smith, V. V., Weinberg, D. H., Wilson, J. C., & Zasowski, G. 2012, *ApJ*, **759**, 131

Bower, R. G., Benson, A. J., Malbon, R., Helly, J. C., Frenk, C. S., Baugh, C. M., Cole, S., & Lacey, C. G. 2006, *MNRAS*, **370**, 645

Boylan-Kolchin, M., Bullock, J. S., & Kaplinghat, M. 2011, *MNRAS*, **415**, L40

Boylan-Kolchin, M., Bullock, J. S., Sohn, S. T., Besla, G., & van der Marel, R. P. 2013, *ApJ*, **768**, 140

Boylan-Kolchin, M., Springel, V., White, S. D. M., & Jenkins, A. 2010, *MNRAS*, **406**, 896

Bruzual, G. & Charlot, S. 2003, *MNRAS*, **344**, 1000

Bullock, J. S. & Johnston, K. V. 2005, *ApJ*, **635**, 931

Bullock, J. S., Kravtsov, A. V., & Weinberg, D. H. 2000, *ApJ*, **539**, 517

Bullock, J. S., Stewart, K. R., Kaplinghat, M., Tollerud, E. J., & Wolf, J. 2010, *ApJ*, **717**, 1043

Busha, M. T., Wechsler, R. H., Behroozi, P. S., Gerke, B. F., Klypin, A. A., & Primack, J. R. 2011, *ApJ*, **743**, 117

Chabrier, G. 2003, *PASP*, **115**, 763

Clewley, L., Warren, S. J., Hewett, P. C., Norris, J. E., Wilkinson, M. I., & Evans, N. W. 2005, *MNRAS*, **362**, 349

Coleman, M. G., Jordi, K., Rix, H.-W., Grebel, E. K., & Koch, A. 2007, *AJ*, **134**, 1938

Colín, P., Avila-Reese, V., & Valenzuela, O. 2000, *ApJ*, **542**, 622

Cooper, A. P., Cole, S., Frenk, C. S., White, S. D. M., Helly, J., Benson, A. J., De Lucia, G., Helmi, A., Jenkins, A., Navarro, J. F., Springel, V., & Wang, J. 2010, *MNRAS*, **406**, 744

de Jong, J. T. A., Harris, J., Coleman, M. G., Martin, N. F., Bell, E. F., Rix, H.-W., Hill, J. M., Skillman, E. D., Sand, D. J., Olszewski, E. W., Zaritsky, D., Thompson, D., Giallongo, E., Ragazzoni, R., DiPaola, A., Farinato, J., Testa, V., & Bechtold, J. 2008, *ApJ*, **680**, 1112

Deason, A. J., Belokurov, V., & Evans, N. W. 2011, *MNRAS*, **416**, 2903

Deason, A. J., Belokurov, V., Evans, N. W., & An, J. 2012a, *MNRAS*, **424**, L44

Deason, A. J., Belokurov, V., Evans, N. W., Koposov, S. E., Cooke, R. J., Peñarrubia, J., Laporte, C. F. P., Fellhauer, M., Walker, M. G., & Olszewski, E. W. 2012b, *MNRAS*, **425**, 2840

Dehnen, W., McLaughlin, D. E., & Sachania, J. 2006, *MNRAS*, **369**, 1688

Devecchi, B., Volonteri, M., Rossi, E. M., Colpi, M., & Portegies Zwart, S. 2012, *MNRAS*, **421**, 1465

Di Matteo, T., Colberg, J., Springel, V., Hernquist, L., & Sijacki, D. 2008, *ApJ*, **676**, 33

Diemand, J., Kuhlen, M., & Madau, P. 2006, *ApJ*, **649**, 1

Diemand, J., Kuhlen, M., Madau, P., Zemp, M., Moore, B., Potter, D., & Stadel, J. 2008, *Nature*, **454**, 735

Diemand, J., Madau, P., & Moore, B. 2005, *MNRAS*, **364**, 367

Fan, X. 2006, *NewAR*, **50**, 665

Farrell, S. A., Webb, N. A., Barret, D., Godet, O., & Rodrigues, J. M. 2009, *Nature*, **460**, 73

Ferrarese, L. & Merritt, D. 2000, *ApJ*, **539**, L9

Gebhardt, K., Kormendy, J., Ho, L. C., Bender, R., Bower, G., Dressler, A., Faber, S. M., Filippenko, A. V., Green, R., Grillmair, C., Lauer, T. R., Magorrian, J., Pinkney, J., Richstone, D., & Tremaine, S. 2000, *ApJ*, **543**, L5

Gebhardt, K., Rich, R. M., & Ho, L. C. 2005, *ApJ*, **634**, 1093

Geha, M., Willman, B., Simon, J. D., Strigari, L. E., Kirby, E. N., Law, D. R., & Strader, J. 2009, *ApJ*, **692**, 1464

Ghez, A. M., Salim, S., Weinberg, N. N., Lu, J. R., Do, T., Dunn, J. K., Matthews, K., Morris, M. R., Yelda, S., Becklin, E. E., Kremenek, T., Milosavljevic, M., & Naiman, J. 2008, *ApJ*, **689**, 1044

Gilbert, K. M., Guhathakurta, P., Kalirai, J. S., Rich, R. M., Majewski, S. R., Ostheimer, J. C., Reitzel, D. B., Cenarro, A. J., Cooper, M. C., Luine, C., & Patterson, R. J. 2006, *ApJ*, **652**, 1188

Gnedin, O. Y., Brown, W. R., Geller, M. J., & Kenyon, S. J. 2010, *ApJ*, **720**, L108

Governato, F., Brook, C., Mayer, L., Brooks, A., Rhee, G., Wadsley, J., Jonsson, P., Willman, B., Stinson, G., Quinn, T., & Madau, P. 2010, *Nature*, **463**, 203

Graham, A. W., Onken, C. A., Athanassoula, E., & Combes, F. 2011, *MNRAS*, **412**, 2211

Guedes, J., Madau, P., Mayer, L., & Callegari, S. 2011, *ApJ*, **729**, 125

Guedes, J., Mayer, L., Carollo, M., & Madau, P. 2012, *ArXiv e-prints*

Gunn, J. E., Carr, M., Rockosi, C., Sekiguchi, M., Berry, K., Elms, B., de Haas, E., Ivezić, Ž., Knapp, G., Lupton, R., Pauls, G., Simcoe, R., Hirsch, R., Sanford, D., Wang, S., York, D., Harris, F., Annis, J., Bartozek, L., Boroski, W., Bakken, J., Haldeman, M., Kent, S., Holm, S., Holmgren, D., Petravick, D., Prosapio, A., Rechenmacher, R., Doi, M., Fukugita, M., Shimasaku, K., Okada, N., Hull, C., Siegmund, W., Mannery, E., Blouke, M., Heidtman, D., Schneider, D., Lucinio, R., & Brinkman, J. 1998, *AJ*, **116**, 3040

Haardt, F. & Madau, P. 1996, *ApJ*, **461**, 20

Häring, N. & Rix, H.-W. 2004, *ApJ*, **604**, L89

Ibata, R., Irwin, M., Lewis, G., Ferguson, A. M. N., & Tanvir, N. 2001a, *Nature*, **412**, 49

Ibata, R., Lewis, G. F., Irwin, M., Totten, E., & Quinn, T. 2001b, *ApJ*, **551**, 294

Ibata, R. A., Gilmore, G., & Irwin, M. J. 1994, *Nature*, **370**, 194

Inoue, K. T., Rashkov, V., Silk, J., & Madau, P. 2013, *ArXiv e-prints*

Irwin, M. J., Belokurov, V., Evans, N. W., Ryan-Weber, E. V., de Jong, J. T. A., Koposov, S., Zucker, D. B., Hodgkin, S. T., Gilmore, G., Prema, P., Hebb, L., Begum, A., Fellhauer, M., Hewett, P. C., Kennicutt, Jr., R. C., Wilkinson, M. I., Bramich, D. M., Vidrih, S., Rix, H.-W., Beers, T. C., Barentine, J. C., Brewington, H., Harvanek, M., Krzesinski, J., Long, D., Nitta, A., & Snedden, S. A. 2007, *ApJ*, **656**, L13

Islam, R. R., Taylor, J. E., & Silk, J. 2003, *MNRAS*, **340**, 647

Jurić, M., Ivezić, Ž., Brooks, A., Lupton, R. H., Schlegel, D., Finkbeiner, D., Padmanabhan, N., Bond, N., Sesar, B., Rockosi, C. M., Knapp, G. R., Gunn, J. E., Sumi, T., Schneider, D. P., Barentine, J. C., Brewington, H. J., Brinkmann, J., Fukugita, M., Harvanek, M., Kleinman,

S. J., Krzesinski, J., Long, D., Neilsen, Jr., E. H., Nitta, A., Snedden, S. A., & York, D. G. 2008, *ApJ*, **673**, 864

Kaaret, P., Prestwich, A. H., Zezas, A., Murray, S. S., Kim, D.-W., Kilgard, R. E., Schlegel, E. M., & Ward, M. J. 2001, *MNRAS*, **321**, L29

Kalirai, J. S., Gilbert, K. M., Guhathakurta, P., Majewski, S. R., Ostheimer, J. C., Rich, R. M., Cooper, M. C., Reitzel, D. B., & Patterson, R. J. 2006, *ApJ*, **648**, 389

Kauffmann, G., White, S. D. M., & Guiderdoni, B. 1993, *MNRAS*, **264**, 201

Kazantzidis, S., Mayer, L., Colpi, M., Madau, P., Debattista, V. P., Wadsley, J., Stadel, J., Quinn, T., & Moore, B. 2005, *ApJ*, **623**, L67

King, I. 1962, *AJ*, **67**, 471

Kirby, E. N., Simon, J. D., Geha, M., Guhathakurta, P., & Frebel, A. 2008, *ApJ*, **685**, L43

Klypin, A., Kravtsov, A. V., Valenzuela, O., & Prada, F. 1999, *ApJ*, **522**, 82

Kochanek, C. S. 1996, *ApJ*, **457**, 228

Komossa, S. & Merritt, D. 2008, *ApJ*, **683**, L21

Koposov, S., Belokurov, V., Evans, N. W., Hewett, P. C., Irwin, M. J., Gilmore, G., Zucker, D. B., Rix, H.-W., Fellhauer, M., Bell, E. F., & Glushkova, E. V. 2008, *ApJ*, **686**, 279

Koposov, S. E., Yoo, J., Rix, H.-W., Weinberg, D. H., Macciò, A. V., & Escudé, J. M. 2009, *ApJ*, **696**, 2179

Koushiappas, S. M., Bullock, J. S., & Dekel, A. 2004, *MNRAS*, **354**, 292

Kravtsov, A. 2010, *Advances in Astronomy*, 2010

Kravtsov, A. V., Gnedin, O. Y., & Klypin, A. A. 2004, *ApJ*, **609**, 482

Kroupa, P., Tout, C. A., & Gilmore, G. 1993, *MNRAS*, **262**, 545

Kuhlen, M., Krumholz, M. R., Madau, P., Smith, B. D., & Wise, J. 2012, *ApJ*, **749**, 36

Kulessa, A. S. & Lynden-Bell, D. 1992, *MNRAS*, **255**, 105

Little, B. & Tremaine, S. 1987, *ApJ*, **320**, 493

Liu, L., Gerke, B. F., Wechsler, R. H., Behroozi, P. S., & Busha, M. T. 2011, *ApJ*, **733**, 62

Lodato, G. & Natarajan, P. 2006, *MNRAS*, **371**, 1813

Loeb, A. & Rasio, F. A. 1994, *ApJ*, **432**, 52

Lützgendorf, N., Kissler-Patig, M., Gebhardt, K., Baumgardt, H., Noyola, E., de Zeeuw, P. T., Neumayer, N., Jalali, B., & Feldmeier, A. 2012, *ArXiv e-prints*

Macciò, A. V., Kang, X., Fontanot, F., Somerville, R. S., Koposov, S., & Monaco, P. 2010, *MNRAS*, **402**, 1995

Macciò, A. V., Kang, X., & Moore, B. 2009, *ApJ*, **692**, L109

Madau, P., Diemand, J., & Kuhlen, M. 2008a, *ApJ*, **679**, 1260

Madau, P., Kuhlen, M., Diemand, J., Moore, B., Zemp, M., Potter, D., & Stadel, J. 2008b, *ApJ*, **689**, L41

Madau, P. & Rees, M. J. 2001, *ApJ*, **551**, L27

Majewski, S. R., Skrutskie, M. F., Weinberg, M. D., & Ostheimer, J. C. 2003, *ApJ*, **599**, 1082

Mamon, G. A. & Łokas, E. L. 2005, *MNRAS*, **363**, 705

Martin, N. F., de Jong, J. T. A., & Rix, H.-W. 2008, *ApJ*, **684**, 1075

Martínez-Delgado, D., Gabany, R. J., Crawford, K., Zibetti, S., Majewski, S. R., Rix, H.-W., Fliri, J., Carballo-Bello, J. A., Bardalez-Gagliuffi, D. C., Peñarrubia, J., Chonis, T. S., Madore, B., Trujillo, I., Schirmer, M., & McDavid, D. A. 2010, *AJ*, **140**, 962

Mateo, M. L. 1998, *ARA&A*, **36**, 435

Mauron, N. 2008, *A&A*, **482**, 151

Mauron, N., Kendall, T. R., & Gigoyan, K. 2005, *A&A*, **438**, 867

Mayer, L., Kazantzidis, S., Escala, A., & Callegari, S. 2010, *Nature*, **466**, 1082

Mayer, L., Mastropietro, C., Wadsley, J., Stadel, J., & Moore, B. 2006, *MNRAS*, **369**, 1021

McConnachie, A. W., Irwin, M. J., Ibata, R. A., Dubinski, J., Widrow, L. M., Martin, N. F., Côté, P., Dotter, A. L., Navarro, J. F., Ferguson, A. M. N., Puzia, T. H., Lewis, G. F., Babul, A., Barmby, P., Bienaymé, O., Chapman, S. C., Cockcroft, R., Collins, M. L. M., Fardal, M. A., Harris, W. E., Huxor, A., Mackey, A. D., Peñarrubia, J., Rich, R. M., Richer, H. B., Siebert, A., Tanvir, N., Valls-Gabaud, D., & Venn, K. A. 2009, *Nature*, **461**, 66

McConnell, N. J. & Ma, C.-P. 2013, *ApJ*, **764**, 184

Merritt, D., Schnittman, J. D., & Komossa, S. 2009, *ApJ*, **699**, 1690

Micic, M., Abel, T., & Sigurdsson, S. 2006, *MNRAS*, **372**, 1540

Micic, M., Holley-Bockelmann, K., & Sigurdsson, S. 2011, *MNRAS*, **414**, 1127

Moore, B., Diemand, J., Madau, P., Zemp, M., & Stadel, J. 2006, *MNRAS*, **368**, 563

Moore, B., Ghigna, S., Governato, F., Lake, G., Quinn, T., Stadel, J., & Tozzi, P. 1999, *ApJ*, **524**, L19

Mouhcine, M., Ibata, R., & Rejkuba, M. 2010, *ApJ*, **714**, L12

Muñoz, J. A., Madau, P., Loeb, A., & Diemand, J. 2009, *MNRAS*, **400**, 1593

Navarro, J. F., Frenk, C. S., & White, S. D. M. 1996, *ApJ*, **462**, 563

Noyola, E., Gebhardt, K., Kissler-Patig, M., Lützgendorf, N., Jalali, B., de Zeeuw, P. T., & Baumgardt, H. 2010, *ApJ*, **719**, L60

O'Leary, R. M. & Loeb, A. 2009, *MNRAS*, **395**, 781

O'Leary, R. M. & Loeb, A. 2012, *MNRAS*, **421**, 2737

Orban, C., Gnedin, O. Y., Weisz, D. R., Skillman, E. D., Dolphin, A. E., & Holtzman, J. A. 2008, *ApJ*, **686**, 1030

Orosz, J. A., McClintock, J. E., Narayan, R., Bailyn, C. D., Hartman, J. D., Macri, L., Liu, J., Pietsch, W., Remillard, R. A., Shporer, A., & Mazeh, T. 2007, *Nature*, **449**, 872

Perryman, M. A. C., de Boer, K. S., Gilmore, G., Høg, E., Lattanzi, M. G., Lindegren, L., Luri, X., Mignard, F., Pace, O., & de Zeeuw, P. T. 2001, *A&A*, **369**, 339

Pizagno, J., Prada, F., Weinberg, D. H., Rix, H.-W., Pogge, R. W., Grebel, E. K., Harbeck, D., Blanton, M., Brinkmann, J., & Gunn, J. E. 2007, *AJ*, **134**, 945

Plummer, H. C. 1911, *MNRAS*, **71**, 460

Pohlen, M. & Trujillo, I. 2006, *A&A*, **454**, 759

Pontzen, A. & Governato, F. 2012, *MNRAS*, **421**, 3464

Press, W. H. & Schechter, P. 1974, *ApJ*, **187**, 425

Rashkov, V. & Madau, P. 2013, *ArXiv e-prints*

Rashkov, V., Madau, P., Kuhlen, M., & Diemand, J. 2012, *ApJ*, **745**, 142

Rohlfs, K. & Kreitschmann, J. 1988, *A&A*, **201**, 51

Sakamoto, T., Chiba, M., & Beers, T. C. 2003, *A&A*, **397**, 899

Sand, D. J., Olszewski, E. W., Willman, B., Zaritsky, D., Seth, A., Harris, J., Piatek, S., & Saha, A. 2009, *ApJ*, **704**, 898

Schlaufman, K. C., Rockosi, C. M., Allende Prieto, C., Beers, T. C., Bizyaev, D., Brewington, H., Lee, Y. S., Malanushenko, V., Malanushenko, E., Oravetz, D., Pan, K., Simmons, A., Snedden, S., & Yanny, B. 2009, *ApJ*, **703**, 2177

Schlaufman, K. C., Rockosi, C. M., Lee, Y. S., Beers, T. C., Allende Prieto, C., Rashkov, V., Madau, P., & Bizyaev, D. 2012, *ApJ*, **749**, 77

Simon, J. D. & Geha, M. 2007, *ApJ*, **670**, 313

Simon, J. D., Geha, M., Minor, Q. E., Martinez, G. D., Kirby, E. N., Bullock, J. S., Kaplinghat, M., Strigari, L. E., Willman, B., Choi, P. I., Tollerud, E. J., & Wolf, J. 2011, *ApJ*, **733**, 46

Smith, M. C., Ruchti, G. R., Helmi, A., Wyse, R. F. G., Fulbright, J. P., Freeman, K. C., Navarro, J. F., Seabroke, G. M., Steinmetz, M., Williams, M., Bienaymé, O., Binney, J., Bland-Hawthorn, J., Dehnen, W., Gibson, B. K., Gilmore, G., Grebel, E. K., Munari, U., Parker, Q. A., Scholz, R.-D., Siebert, A., Watson, F. G., & Zwitter, T. 2007, *MNRAS*, **379**, 755

Sohn, S. T., Anderson, J., & van der Marel, R. P. 2012, *ApJ*, **753**, 7

Somerville, R. S. 2002, *ApJ*, **572**, L23

Spergel, D. N., Bean, R., Doré, O., Nolta, M. R., Bennett, C. L., Dunkley, J., Hinshaw, G., Jarosik, N., Komatsu, E., Page, L., Peiris, H. V., Verde, L., Halpern, M., Hill, R. S., Kogut, A., Limon, M., Meyer, S. S., Odegard, N., Tucker, G. S., Weiland, J. L., Wollack, E., & Wright, E. L. 2007, *ApJS*, **170**, 377

Springel, V., Wang, J., Vogelsberger, M., Ludlow, A., Jenkins, A., Helmi, A., Navarro, J. F., Frenk, C. S., & White, S. D. M. 2008, *MNRAS*, **391**, 1685

Stacy, A. & Bromm, V. 2012, *ArXiv e-prints*

Stadel, J. G. 2001, *Ph.D. thesis*, UNIVERSITY OF WASHINGTON

Stinson, G., Seth, A., Katz, N., Wadsley, J., Governato, F., & Quinn, T. 2006, *MNRAS*, **373**, 1074

Strigari, L. E., Bullock, J. S., Kaplinghat, M., Diemand, J., Kuhlen, M., & Madau, P. 2007, *ApJ*, **669**, 676

Strigari, L. E., Bullock, J. S., Kaplinghat, M., Simon, J. D., Geha, M., Willman, B., & Walker, M. G. 2008, *Nature*, **454**, 1096

Strigari, L. E., Frenk, C. S., & White, S. D. M. 2010, *MNRAS*, **408**, 2364

Stringer, M., Cole, S., & Frenk, C. S. 2010, *MNRAS*, **404**, 1129

Tanaka, T. & Haiman, Z. 2009, *ApJ*, **696**, 1798

Tollerud, E. J., Bullock, J. S., Strigari, L. E., & Willman, B. 2008, *ApJ*, **688**, 277

Totten, E. J. & Irwin, M. J. 1998, *MNRAS*, **294**, 1

Totten, E. J., Irwin, M. J., & Whitelock, P. A. 2000, *MNRAS*, **314**, 630

Tremaine, S., Gebhardt, K., Bender, R., Bower, G., Dressler, A., Faber, S. M., Filippenko, A. V., Green, R., Grillmair, C., Ho, L. C., Kormendy, J., Lauer, T. R., Magorrian, J., Pinkney, J., & Richstone, D. 2002, *ApJ*, **574**, 740

Tremonti, C. A., Heckman, T. M., Kauffmann, G., Brinchmann, J., Charlot, S., White, S. D. M., Seibert, M., Peng, E. W., Schlegel, D. J., Uomoto, A., Fukugita, M., & Brinkmann, J. 2004, *ApJ*, **613**, 898

Tumlinson, J. 2010, *ApJ*, **708**, 1398

van Wassenhove, S., Volonteri, M., Walker, M. G., & Gair, J. R. 2010, *MNRAS*, **408**, 1139

Vink, J. S., de Koter, A., & Lamers, H. J. G. L. M. 2001, *A&A*, **369**, 574

Volonteri, M., Haardt, F., & Madau, P. 2003, *ApJ*, **582**, 559

Volonteri, M. & Perna, R. 2005, *MNRAS*, **358**, 913

Wadsley, J. W., Stadel, J., & Quinn, T. 2004, *New Astronomy*, **9**, 137

Walker, M. G., Mateo, M., Olszewski, E. W., Peñarrubia, J., Wyn Evans, N., & Gilmore, G. 2009, *ApJ*, **704**, 1274

Wang, W. & White, S. D. M. 2012, *MNRAS*, **424**, 2574

Watkins, L. L., Evans, N. W., & An, J. H. 2010, *MNRAS*, **406**, 264

White, S. D. M. & Rees, M. J. 1978, *MNRAS*, **183**, 341

White, S. D. M. & Springel, V. 2000, in A. Weiss, T. G. Abel, & V. Hill (eds.), *The First Stars*, p. 327

Wilkinson, M. I. & Evans, N. W. 1999, *MNRAS*, **310**, 645

Willman, B., Dalcanton, J. J., Martinez-Delgado, D., West, A. A., Blanton, M. R., Hogg, D. W., Barentine, J. C., Brewington, H. J., Harvanek, M., Kleinman, S. J., Krzesinski, J., Long, D., Neilsen, Jr., E. H., Nitta, A., & Snedden, S. A. 2005, *ApJ*, **626**, L85

Wolf, J., Martinez, G. D., Bullock, J. S., Kaplinghat, M., Geha, M., Muñoz, R. R., Simon, J. D., & Avedo, F. F. 2010, *MNRAS*, **406**, 1220

Xiao, T., Barth, A. J., Greene, J. E., Ho, L. C., Bentz, M. C., Ludwig, R. R., & Jiang, Y. 2011, *ApJ*, **739**, 28

Xue, X. X., Rix, H. W., Zhao, G., Re Fiorentin, P., Naab, T., Steinmetz, M., van den Bosch, F. C., Beers, T. C., Lee, Y. S., Bell, E. F., Rockosi, C., Yanny, B., Newberg, H., Wilhelm, R., Kang, X., Smith, M. C., & Schneider, D. P. 2008, *ApJ*, **684**, 1143

Yanny, B., Newberg, H. J., Kent, S., Laurent-Muehleisen, S. A., Pier, J. R., Richards, G. T., Stoughton, C., Anderson, Jr., J. E., Annis, J., Brinkmann, J., Chen, B., Csabai, I., Doi, M., Fukugita, M., Hennessy, G. S., Ivezić, Ž., Knapp, G. R., Lupton, R., Munn, J. A., Nash, T., Rockosi, C. M., Schneider, D. P., Smith, J. A., & York, D. G. 2000, *ApJ*, **540**, 825

Yanny, B., Rockosi, C., Newberg, H. J., Knapp, G. R., Adelman-McCarthy, J. K., Alcorn, B., Allam, S., Allende Prieto, C., An, D., Anderson, K. S. J., Anderson, S., Bailer-Jones, C. A. L., Bastian, S., Beers, T. C., Bell, E., Belokurov, V., Bizyaev, D., Blythe, N., Bochanski, J. J., Boroski, W. N., Brinchmann, J., Brinkmann, J., Brewington, H., Carey, L., Cudworth, K. M., Evans, M., Evans, N. W., Gates, E., Gänsicke, B. T., Gillespie, B., Gilmore, G., Nebot Gomez-Moran, A., Grebel, E. K., Greenwell, J., Gunn, J. E., Jordan, C., Jordan, W., Harding, P., Harris, H., Hendry, J. S., Holder, D., Ivans, I. I., Ivezič, Ž., Jester, S., Johnson, J. A., Kent, S. M., Kleinman, S., Kniazev, A., Krzesinski, J., Kron, R., Kuropatkin, N., Lebedeva, S., Lee, Y. S., French Leger, R., Lépine, S., Levine, S., Lin, H., Long, D. C., Loomis, C., Lupton, R., Malanushenko, O., Malanushenko, V., Margon, B., Martinez-Delgado, D., McGehee, P., Monet, D., Morrison, H. L., Munn, J. A., Neilsen, Jr., E. H., Nitta, A., Norris, J. E., Oravetz, D., Owen, R., Padmanabhan, N., Pan, K., Peterson, R. S., Pier, J. R., Platson, J., Re Fiorentin, P., Richards, G. T., Rix, H.-W., Schlegel, D. J., Schneider, D. P., Schreiber, M. R., Schwope, A., Sibley, V., Simmons, A., Snedden, S. A., Allyn Smith, J., Stark, L., Stauffer, F., Steinmetz, M., Stoughton, C., SubbaRao, M., Szalay, A., Szkody, P., Thakar, A. R., Sivarani, T., Tucker, D., Uomoto, A., Vanden Berk, D., Vidrih, S., Wadadekar, Y., Watters, S., Wilhelm, R., Wyse, R. F. G., Yarger, J., & Zucker, D. 2009, *AJ*, **137**, 4377

York, D. G., Adelman, J., Anderson, Jr., J. E., Anderson, S. F., Annis, J., Bahcall, N. A., Bakken, J. A., Barkhouser, R., Bastian, S., Berman, E., Boroski, W. N., Bracker, S., Briegel, C., Briggs, J. W., Brinkmann, J., Brunner, R., Burles, S., Carey, L., Carr, M. A., Castander, F. J., Chen, B., Colestock, P. L., Connolly, A. J., Crocker, J. H., Csabai, I., Czarapata, P. C., Davis, J. E., Doi, M., Dombeck, T., Eisenstein, D., Ellman, N., Elms, B. R., Evans, M. L., Fan, X., Federwitz, G. R., Fiscelli, L., Friedman, S., Frieman, J. A., Fukugita, M., Gillespie, B., Gunn, J. E., Gurbani, V. K., de Haas, E., Haldeman, M., Harris, F. H., Hayes, J., Heckman, T. M., Hennessy, G. S., Hindsley, R. B., Holm, S., Holmgren, D. J., Huang, C.-h., Hull, C., Husby, D., Ichikawa, S.-I., Ichikawa, T., Ivezić, Ž., Kent, S., Kim, R. S. J., Kinney, E., Klaene, M., Kleinman, A. N., Kleinman, S., Knapp, G. R., Korienek, J., Kron, R. G., Kunszt, P. Z., Lamb, D. Q., Lee, B., Leger, R. F., Limmongkol, S., Lindenmeyer, C., Long, D. C., Loomis, C., Loveday, J., Lucinio, R., Lupton, R. H., MacKinnon, B., Mannery, E. J., Mantsch, P. M., Margon, B., McGehee, P., McKay, T. A., Meiksin, A., Merelli, A., Monet, D. G., Munn, J. A., Narayanan, V. K., Nash, T., Neilsen, E., Neswold, R., Newberg, H. J., Nichol, R. C., Nicinski, T., Nonino, M., Okada, N., Okamura, S., Ostriker, J. P., Owen, R., Pauls, A. G., Peoples, J., Peterson, R. L., Petravick, D., Pier, J. R., Pope, A., Pordes, R., Prosapio, A., Rechenmacher, R., Quinn, T. R., Richards, G. T., Richmond, M. W., Rivetta, C. H., Rockosi, C. M., Ruthmansdorfer, K., Sandford, D., Schlegel, D. J., Schneider, D. P., Sekiguchi, M., Sergey, G., Shimasaku, K., Siegmund, W. A., Smee, S., Smith, J. A., Snedden, S., Stone, R., Stoughton, C., Strauss, M. A., Stubbs, C., SubbaRao, M., Szalay, A. S., Szapudi, I., Szokoly,

G. P., Thakar, A. R., Tremonti, C., Tucker, D. L., Uomoto, A., Vanden Berk, D., Vogeley, M. S., Waddell, P., Wang, S.-i., Watanabe, M., Weinberg, D. H., Yanny, B., Yasuda, N., & SDSS Collaboration 2000, *AJ*, **120**, 1579

Zaritsky, D., Olszewski, E. W., Schommer, R. A., Peterson, R. C., & Aaronson, M. 1989, *ApJ*, **345**, 759

Zemp, M., Diemand, J., Kuhlen, M., Madau, P., Moore, B., Potter, D., Stadel, J., & Widrow, L. 2009, *MNRAS*, **394**, 641